33RD INTERNATIONAL COSMIC RAY CONFERENCE, RIO DE JANEIRO 2013
THE ASTROPARTICLE PHYSICS CONFERENCE

# The IceCube Neutrino Observatory Part III: Cosmic Rays

THE ICECUBE COLLABORATION



## Contents

**1 Measurement of the cosmic ray energy spectrum with IceTop 73 (paper 0246) 5**

**2 Ground level enhancement of May 17, 2012 observed at South Pole (paper 0368) 9**

**3 An update on cosmic anisotropy studies with IceCube (paper 0382) 13**

**4 Study of the time-dependence of the cosmic-ray anisotropy with AMANDA and IceCube (paper 0411) 17**

**5 Low energy air showers with IceTop (paper 0674) 21**

**6 Seasonal variation of the muon multiplicity in cosmic rays at South Pole (paper 0763) 25**

**7 Cosmic ray composition and energy spectrum between 2.5 PeV and 1 EeV (paper 0861) 29**

**8 Inclined cosmic ray air showers in IceCube (paper 0973) 33**

**9 The effect of snow accumulation on signals in IceTop (paper 1106) 37**

**Keywords:** IceCube, neutrino astronomy, neutrino telescopes, IceTop, air showers, cosmic rays: spectrum, composition, anisotropy; solar ground level enhancement, muon multiplicity.

## IceCube Collaboration Member List

M. G. Aartsen[2], R. Abbasi[27], Y. Abdou[22], M. Ackermann[41], J. Adams[15], J. A. Aguilar[21], M. Ahlers[27], D. Altmann[9], J. Auffenberg[27], X. Bai[31,a], M. Baker[27], S. W. Barwick[23], V. Baum[28], R. Bay[7], J. J. Beatty[17,18], S. Bechet[12], J. Becker Tjus[10], K.-H. Becker[40], M. Bell[38], M. L. Benabderrahmane[41], S. BenZvi[27], P. Berghaus[41], D. Berley[16], E. Bernardini[41], A. Bernhard[30], D. Bertrand[12], D. Z. Besson[25], G. Binder[8,7], D. Bindig[40], M. Bissok[1], E. Blaufuss[16], J. Blumenthal[1], D. J. Boersma[39], S. Bohaichuk[20], C. Bohm[34], D. Bose[13], S. Böser[11], O. Botner[39], L. Brayeur[13], H.-P. Bretz[41], A. M. Brown[15], R. Bruijn[24], J. Brunner[41], M. Carson[22], J. Casey[5], M. Casier[13], D. Chirkin[27], A. Christov[21], B. Christy[16], K. Clark[38], F. Clevermann[19], S. Coenders[1], S. Cohen[24], D. F. Cowen[38,37], A. H. Cruz Silva[41], M. Danninger[34], J. Daughhetee[5], J. C. Davis[17], C. De Clercq[13], S. De Ridder[22], P. Desiati[27], K. D. de Vries[13], M. de With[9], T. DeYoung[38], J. C. Díaz-Vélez[27], M. Dunkman[38], R. Eagan[38], B. Eberhardt[28], J. Eisch[27], R. W. Ellsworth[16], S. Euler[1], P. A. Evenson[31], O. Fadiran[27], A. R. Fazely[6], A. Fedynitch[10], J. Feintzeig[27], T. Feusels[22], K. Filimonov[7], C. Finley[34], T. Fischer-Wasels[40], S. Flis[34], A. Franckowiak[11], K. Frantzen[19], T. Fuchs[19], T. K. Gaisser[31], J. Gallagher[26], L. Gerhardt[8,7], L. Gladstone[27], T. Glüsenkamp[41], A. Goldschmidt[8], G. Golup[13], J. G. Gonzalez[31], J. A. Goodman[16], D. Góra[41], D. T. Grandmont[20], D. Grant[20], A. Groß[30], C. Ha[8,7], A. Haj Ismail[22], P. Hallen[1], A. Hallgren[39], F. Halzen[27], K. Hanson[12], D. Heereman[12], D. Heinen[1], K. Helbing[40], R. Hellauer[16], S. Hickford[15], G. C. Hill[2], K. D. Hoffman[16], R. Hoffmann[40], A. Homeier[11], K. Hoshina[27], W. Huelsnitz[16,b], P. O. Hulth[34], K. Hultqvist[34], S. Hussain[31], A. Ishihara[14], E. Jacobi[41], J. Jacobsen[27], K. Jagielski[1], G. S. Japaridze[4], K. Jero[27], O. Jlelati[22], B. Kaminsky[41], A. Kappes[9], T. Karg[41], A. Karle[27], J. L. Kelley[27], J. Kiryluk[35], J. Kläs[40], S. R. Klein[8,7], J.-H. Köhne[19], G. Kohnen[29], H. Kolanoski[9], L. Köpke[28], C. Kopper[27], S. Kopper[40], D. J. Koskinen[38], M. Kowalski[11], M. Krasberg[27], K. Krings[1], G. Kroll[28], J. Kunnen[13], N. Kurahashi[27], T. Kuwabara[31], M. Labare[22], H. Landsman[27], M. J. Larson[36], M. Lesiak-Bzdak[35], M. Leuermann[1], J. Leute[30], J. Lünemann[28], J. Madsen[33], G. Maggi[13], R. Maruyama[27], K. Mase[14], H. S. Matis[8], F. McNally[27], K. Meagher[16], M. Merck[27], P. Mészáros[37,38], T. Meures[12], S. Miarecki[8,7], E. Middell[41], N. Milke[19], J. Miller[13], L. Mohrmann[41], T. Montaruli[21,c], R. Morse[27], R. Nahnhauer[41], U. Naumann[40], H. Niederhausen[35], S. C. Nowicki[20], D. R. Nygren[8], A. Obertacke[40], S. Odrowski[20], A. Olivas[16], M. Olivo[10], A. O'Murchadha[12], L. Paul[1], J. A. Pepper[36], C. Pérez de los Heros[39], C. Pfendner[17], D. Pieloth[19], E. Pinat[12], J. Posselt[40], P. B. Price[7], G. T. Przybylski[8], L. Rädel[1], M. Rameez[21], K. Rawlins[3], P. Redl[16], R. Reimann[1], E. Resconi[30], W. Rhode[19], M. Ribordy[24], M. Richman[16], B. Riedel[27], J. P. Rodrigues[27], C. Rott[17,d], T. Ruhe[19], B. Ruzybayev[31], D. Ryckbosch[22], S. M. Saba[10], T. Salameh[38], H.-G. Sander[28], M. Santander[27], S. Sarkar[32], K. Schatto[28], M. Scheel[1], F. Scheriau[19], T. Schmidt[16], M. Schmitz[19], S. Schoenen[1], S. Schöneberg[10], A. Schönwald[41], A. Schukraft[1], L. Schulte[11], O. Schulz[30], D. Seckel[31], Y. Sestayo[30], S. Seunarine[33], R. Shanidze[41], C. Sheremata[20], M. W. E. Smith[38], D. Soldin[40], G. M. Spiczak[33], C. Spiering[41], M. Stamatikos[17,e], T. Stanev[31], A. Stasik[11], T. Stezelberger[8], R. G. Stokstad[8], A. Stößl[41], E. A. Strahler[13], R. Ström[39], G. W. Sullivan[16], H. Taavola[39], I. Taboada[5], A. Tamburro[31], A. Tepe[40], S. Ter-Antonyan[6], G. Tešić[38], S. Tilav[31], P. A. Toale[36], S. Toscano[27], M. Usner[11], D. van der Drift[8,7], N. van Eijndhoven[13], A. Van Overloop[22], J. van Santen[27], M. Vehring[1], M. Voge[11], M. Vraeghe[22], C. Walck[34], T. Waldenmaier[9], M. Wallraff[1], R. Wasserman[38], Ch. Weaver[27], M. Wellons[27], C. Wendt[27], S. Westerhoff[27], N. Whitehorn[27], K. Wiebe[28], C. H. Wiebusch[1], D. R. Williams[36], H. Wissing[16], M. Wolf[34], T. R. Wood[20], K. Woschnagg[7], D. L. Xu[36], X. W. Xu[6], J. P. Yanez[41], G. Yodh[23], S. Yoshida[14], P. Zarzhitsky[36], J. Ziemann[19], S. Zierke[1], M. Zoll[34]

[1]III. Physikalisches Institut, RWTH Aachen University, D-52056 Aachen, Germany
[2]School of Chemistry & Physics, University of Adelaide, Adelaide SA, 5005 Australia
[3]Dept. of Physics and Astronomy, University of Alaska Anchorage, 3211 Providence Dr., Anchorage, AK 99508, USA
[4]CTSPS, Clark-Atlanta University, Atlanta, GA 30314, USA
[5]School of Physics and Center for Relativistic Astrophysics, Georgia Institute of Technology, Atlanta, GA 30332, USA
[6]Dept. of Physics, Southern University, Baton Rouge, LA 70813, USA
[7]Dept. of Physics, University of California, Berkeley, CA 94720, USA
[8]Lawrence Berkeley National Laboratory, Berkeley, CA 94720, USA
[9]Institut für Physik, Humboldt-Universität zu Berlin, D-12489 Berlin, Germany
[10]Fakultät für Physik & Astronomie, Ruhr-Universität Bochum, D-44780 Bochum, Germany
[11]Physikalisches Institut, Universität Bonn, Nussallee 12, D-53115 Bonn, Germany
[12]Université Libre de Bruxelles, Science Faculty CP230, B-1050 Brussels, Belgium
[13]Vrije Universiteit Brussel, Dienst ELEM, B-1050 Brussels, Belgium
[14]Dept. of Physics, Chiba University, Chiba 263-8522, Japan
[15]Dept. of Physics and Astronomy, University of Canterbury, Private Bag 4800, Christchurch, New Zealand
[16]Dept. of Physics, University of Maryland, College Park, MD 20742, USA
[17]Dept. of Physics and Center for Cosmology and Astro-Particle Physics, Ohio State University, Columbus, OH 43210, USA
[18]Dept. of Astronomy, Ohio State University, Columbus, OH 43210, USA
[19]Dept. of Physics, TU Dortmund University, D-44221 Dortmund, Germany
[20]Dept. of Physics, University of Alberta, Edmonton, Alberta, Canada T6G 2E1
[21]Département de physique nucléaire et corpusculaire, Université de Genève, CH-1211 Genève, Switzerland
[22]Dept. of Physics and Astronomy, University of Gent, B-9000 Gent, Belgium
[23]Dept. of Physics and Astronomy, University of California, Irvine, CA 92697, USA
[24]Laboratory for High Energy Physics, École Polytechnique Fédérale, CH-1015 Lausanne, Switzerland
[25]Dept. of Physics and Astronomy, University of Kansas, Lawrence, KS 66045, USA
[26]Dept. of Astronomy, University of Wisconsin, Madison, WI 53706, USA
[27]Dept. of Physics and Wisconsin IceCube Particle Astrophysics Center, University of Wisconsin, Madison, WI 53706, USA
[28]Institute of Physics, University of Mainz, Staudinger Weg 7, D-55099 Mainz, Germany
[29]Université de Mons, 7000 Mons, Belgium
[30]T.U. Munich, D-85748 Garching, Germany
[31]Bartol Research Institute and Department of Physics and Astronomy, University of Delaware, Newark, DE 19716, USA
[32]Dept. of Physics, University of Oxford, 1 Keble Road, Oxford OX1 3NP, UK
[33]Dept. of Physics, University of Wisconsin, River Falls, WI 54022, USA
[34]Oskar Klein Centre and Dept. of Physics, Stockholm University, SE-10691 Stockholm, Sweden
[35]Department of Physics and Astronomy, Stony Brook University, Stony Brook, NY 11794-3800, USA
[36]Dept. of Physics and Astronomy, University of Alabama, Tuscaloosa, AL 35487, USA
[37]Dept. of Astronomy and Astrophysics, Pennsylvania State University, University Park, PA 16802, USA
[38]Dept. of Physics, Pennsylvania State University, University Park, PA 16802, USA
[39]Dept. of Physics and Astronomy, Uppsala University, Box 516, S-75120 Uppsala, Sweden
[40]Dept. of Physics, University of Wuppertal, D-42119 Wuppertal, Germany
[41]DESY, D-15735 Zeuthen, Germany
[a]Physics Department, South Dakota School of Mines and Technology, Rapid City, SD 57701, USA
[b]Los Alamos National Laboratory, Los Alamos, NM 87545, USA
[c]also Sezione INFN, Dipartimento di Fisica, I-70126, Bari, Italy
[d]Department of Physics, Sungkyunkwan University, Suwon 440-746, Korea
[e]NASA Goddard Space Flight Center, Greenbelt, MD 20771, USA

**Acknowledgements**

We acknowledge the support from the following agencies: U.S. National Science Foundation-Office of Polar Programs, U.S. National Science Foundation-Physics Division, University of Wisconsin Alumni Research Foundation, the Grid Laboratory Of Wisconsin (GLOW) grid infrastructure at the University of Wisconsin - Madison, the Open Science Grid (OSG) grid infrastructure; U.S. Department of Energy, and National Energy Research Scientific Computing Center, the Louisiana Optical Network Initiative (LONI) grid computing resources; Natural Sciences and Engineering Research Council of Canada, WestGrid and Compute/Calcul Canada; Swedish Research Council, Swedish Polar Research Secretariat, Swedish National Infrastructure for Computing (SNIC), and Knut and Alice Wallenberg Foundation, Sweden; German Ministry for Education and Research (BMBF), Deutsche Forschungsgemeinschaft (DFG), Helmholtz Alliance for Astroparticle Physics (HAP), Research Department of Plasmas with Complex Interactions (Bochum), Germany; Fund for Scientific Research (FNRS-FWO), FWO Odysseus programme, Flanders Institute to encourage scientific and technological research in industry (IWT), Belgian Federal Science Policy Office (Belspo); University of Oxford, United Kingdom; Marsden Fund, New Zealand; Australian Research Council; Japan Society for Promotion of Science (JSPS); the Swiss National Science Foundation (SNSF), Switzerland.

33RD INTERNATIONAL COSMIC RAY CONFERENCE, RIO DE JANEIRO 2013
THE ASTROPARTICLE PHYSICS CONFERENCE

ICRC 2013

# Measurement of the Cosmic Ray Energy Spectrum with IceTop 73

THE ICECUBE COLLABORATION[1].

[1] *See special section in these proceedings*

*bahtiyar@udel.edu*

**Abstract:** We report on the measurement of the all particle cosmic ray energy spectrum with the IceTop air shower array in the energy range from 1.6 PeV up to 1.3 EeV. The IceTop air shower array is the surface component of the IceCube Neutrino Observatory at the geographical South Pole. The analysis was performed using IceTop in its 73 station configuration when it was 90% complete. The spectrum was derived using an iterative unfolding with shower size as an energy proxy.

**Corresponding authors:** Bakhtiyar Ruzybayev[1], Javier Gonzalez[1]
[1] *University of Delaware*

**Keywords:** IceTop, All-particle energy spectrum.

## 1 Introduction

High resolution measurements of the cosmic ray energy spectrum and the elemental composition will improve our understanding of the acceleration and propagation of high energy cosmic rays. In this paper we investigate the spectrum in the region from 1.6 PeV up to 1.3 EeV. We are reporting on the measurement of the spectrum by the IceTop air shower array in its 73 station configuration using the shower size for the energy estimation. The shower size to energy conversion is performed assuming a mixed primary composition as described in reference [1] and is referred to as H4a model. The zenith dependence of the shower attenuation is used for estimating the uncertainty on the flux due to primary composition.

## 2 The IceTop Detector and Data

IceTop [2] is the surface component of the IceCube Neutrino Observatory. IceTop is designed to detect air showers from primary cosmic rays in the 300 TeV to 1 EeV energy range. IceTop is an air shower array consisting of 81 surface stations in its final configuration and covering an area of one square kilometer. The inter-station separation is about 125 m. Each station consists of two ice Cherenkov tanks separated by 10 m. Two Digital Optical Modules (DOM) [3] are deployed per tank. Each DOM contains a 10 inch photomultiplier tube (PMT) and electronics for signal processing and readout [4]. An Ice-Top station is considered triggered when both tanks in the station record hits within 1 $\mu$s of each other. DOM charges are calibrated using signals from single muons and all charges are converted to the tank and DOM independent unit of 'Vertical Equivalent Muon' (VEM) [2].

This analysis was done on the data taken in the period from June 1, 2010 to May 13, 2011 when IceTop consisted of 73 stations. The effective live-time of the data-set used is 327 days.

## 3 Simulation

Detailed simulations were used to relate measured air shower parameters to the properties of primary cosmic rays. Air showers were simulated in a wide energy range from $10^5$ GeV to $10^{9.5}$ GeV with CORSIKA [6]. Showers above $10^8$ GeV were 'thinned' [7] to reduce computational time and storage volume. Hadronic interaction models used were SIBYLL 2.1 [8] for interactions with energies greater than 80 GeV and FLUKA [9] at lower energies. A smaller set was simulated using QGSJET-II [10] for systematic studies. Simulated atmosphere had an atmospheric overburden of 692.9 g/cm$^2$ (680 hPa), which is also the average overburden for the full year of data. Snow cover on top of tanks in simulation was same as measured in February, 2010. Air showers were simulated with equal number of showers per $\sin\theta\cos\theta$ bin, in a zenith range of 0 to 40 degrees. Four primary types, H, He, O, Fe, were simulated with more than 42000 CORSIKA showers per primary. During the analysis showers are reweighted by different assumed spectra. Each CORSIKA shower was resampled 100 times to increase statistics. Shower cores were uniformly distributed over areas larger than the detector area with an energy dependent resampling radius. The detector response was simulated using IceCube software that simulates the entire chain of data taking and all the hardware [2]. Interactions of charged particles with the IceTop tanks were simulated using the GEANT4 [11] package. The simulations of single primary elements were weighted by a power law spectrum, $\frac{dN}{dE} \propto E^{-2.7}$. For a mixed composition we used the model from reference [1], referred to as H4a. The H4a model consists of 5 elemental groups.

## 4 Analysis

### 4.1 Basic reconstructions

The IceTop reconstruction algorithm [2] uses information from individual tanks, including location, charge and pulse time. Shower direction, core location and shower size are reconstructed by fitting the measured charges with a Lateral Distribution Function (LDF) and the signal times with a

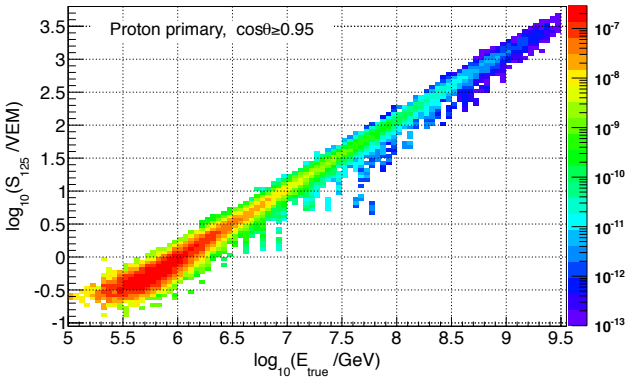


**Fig. 1**: $\log_{10}(S_{125})$ vs. $\log_{10}(E_{true})$. scatter plot for proton primary simulation with $\cos\theta \geq 0.95$, weighted by a flux model $\frac{dN}{dE} \propto E^{-2.7}$

function describing the geometric shape of the shower front. The lateral distribution function is defined as:

$$S(R) = S_{ref}\left(\frac{R}{R_{ref}}\right)^{-\beta-0.303\log_{10}\left(\frac{R}{R_{ref}}\right)}, \qquad (1)$$

where $S_{ref}$ is the shower size or signal at a reference distance $R_{ref}$ to the shower axis, $\beta$ is the slope of the logarithmic LDF at $R_{ref}$. The shower front is described using the signal times as:

$$t(\mathbf{x}) = t_0 + \frac{1}{c}(\mathbf{x}-\mathbf{x}_c)\mathbf{n} + \Delta t(R), \qquad (2)$$

where $t(\mathbf{x})$ is the signal time of the tank at position $\mathbf{x}$, $\mathbf{x}_c$ is the position of shower core on the ground and $\mathbf{n}$ is the unit vector in the direction of movement of the shower. The functional form of $\Delta t(R)$ is a sum of a parabola and a gaussian which describes the curvature as a deviation from the plane perpendicular to the shower axis containing $\mathbf{x}_c$. Equations 1 and 2 describe the expectations for the charge and time of air shower signals. They are fitted to the measured data using a maximum likelihood method [2] with an additional term describing the saturation likelihood. The shower size, $S_{125}$, is defined as the fitted value of the LDF (Eq.1) at a perpendicular distance of 125 m away from the shower axis. From this fit we get the reconstrcuted core location $(x,y)$, zenith $(\theta)$ and azimuthal $(\phi)$ angles.

Snow accumulates on top of IceTop tanks with time, which reduces the measured signal in a tank. To correct for this reduction, the expected signal in the likelihood fitting procedure is reduced according to:

$$S_{expected,corrected} = S_{expected}\exp\left(-\frac{d\sec\theta}{\lambda}\right), \qquad (3)$$

where $d$ is the snow on top of the tank, $\theta$ is the measured zenith angle of the shower and $\lambda = 2.1$ m is the effective attenuation length of the electromagnetic component of the shower in the snow.

The core resolution of the current reconstruction method is better than 15 m around few PeV and improves to less than 8 m at higher energy. The directional resolution is between $0.2^\circ - 0.8^\circ$, depending on energy and zenith angle.

**Table 1**: Fit parameters for Eq.4 for the mixed, H4a, composition assumption in four zenith ranges.

| Composition | Zenith range | $\mathbf{p}_0$ | $\mathbf{p}_1$ |
|---|---|---|---|
| H4a | $\cos\theta \geq 0.95$ | 6.018 | 0.938 |
| | $0.95 > \cos\theta \geq 0.90$ | 6.062 | 0.929 |
| | $0.90 > \cos\theta \geq 0.85$ | 6.117 | 0.921 |
| | $0.85 > \cos\theta \geq 0.80$ | 6.182 | 0.914 |

### 4.2 Event selection

The event selection was done according to the following cuts which were applied both to the simulated and the experimental data.

1. Events must trigger at least 5 stations with reconstructed fits converged (Eqs.1 and 2).
2. Events with $\log_{10}(S_{125}/\text{VEM}) \geq 0.0$.
3. Events with $\cos\theta \geq 0.8$ are selected.
4. Reconstructed cores must be within a geometric boundary that is inside the outermost stations.
5. Events with the largest signal in a station on the edge of the array are rejected.
6. Events in which no station has a signal greater than 6 vertical equivalent muons are rejected.

The last two cuts were introduced to reduce migration of high energy showers that fall outside the geometric containment but still trigger a large number of stations and get reconstructed within the containment area.

### 4.3 Energy estimation method

To estimate the energy of the primary cosmic ray, we use the relationship between shower size $S_{125}$ and the true primary energy, $E_{true}$, from simulations. This relationship depends on the mass of the primary particle and the zenith angle of the air shower. Figure 1 shows a 2-dimensional histogram of the $\log_{10}(S_{125})$ vs $\log_{10}(E_{true})$ for simulated protons weighted by a flux model $\frac{dN}{dE} \propto E^{-2.7}$. For a given zenith bin we slice the distribution shown in Fig.1 in 0.05 bins of $\log_{10}(S_{125})$ and plot the distributions of true energy for each bin. We fit each energy distribution with a gaussian function and use the fitted mean as the energy estimate for the given bin of $\log_{10}(S_{125})$. The relationship between $\log_{10}(S_{125})$ and $\log_{10}(E_{true})$ is:

$$\log_{10}(E) = p_1\log_{10}(S_{125}) + p_0. \qquad (4)$$

Table 1 shows the fit parameters for the mixed compositon assumption. For each composition assumption we get a set of energy estimators as shown in figure 2 for the H4a model assumption. When showing spectra for a given zenith range and assumed composition, the energy was estimated with the appropriate functional relationship.

### 4.4 Flux derivation

The flux was calculated according to the following formula:

$$\mathrm{J}(E) = \frac{\mathrm{d}N}{\mathrm{d}E\,A_{eff}\,\Delta\Omega\,T}, \qquad (5)$$

where $\Delta\Omega = 2\pi(\cos\theta_{min} - \cos\theta_{max})$, solid angle range, T = live-time, and $A_{eff}$ is the effective area

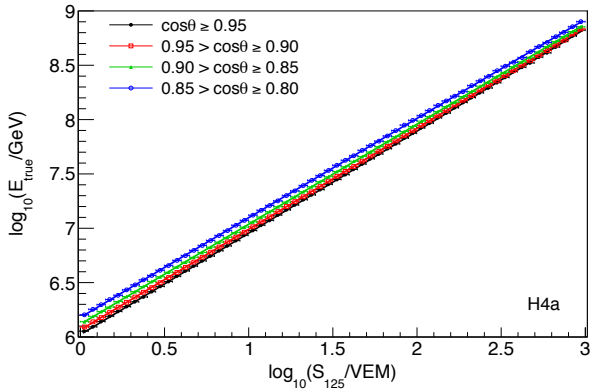


**Fig. 2**: $S_{125}$-to-$E_{true}$ relations in four zenith ranges for the H4a composition assumption.

$$A_{eff} = \mathrm{A_{cut}} \frac{\cos\theta_{max} + \cos\theta_{min}}{2} \varepsilon(E), \qquad (6)$$

where $\mathrm{A_{cut}}$ is the geometric containment and $\varepsilon(E)$ is the detector efficiency

$$\varepsilon(E) = \frac{N_{reco}}{N_{true}}. \qquad (7)$$

where $N_{reco}$ is the number of events with reconstructed energy and zenith angle within the bin, and reconstructed core contained in the IceTop fiducial area, and $N_{true}$ is the number of events with true energy and true zenith angle within the bin, and true core contained in the IceTop fiducial area. Efficiencies were evaluated and applied separately for each composition assumption and each of the four zenith bins. Examples of the derived spectra for different composition assumptions in four zenith ranges can be seen in Fig.3.

The final spectrum was derived assuming the H4a model and averaging over the full zenith range $\cos\theta \geq 0.8$. The spectrum was unfolded by an iterative procedure in which the spectrum derived in the previous step was used to determine the effective area and the $S_{125}$-to-$E_{true}$ relation for the next spectrum evaluation. In case of convergence the effective area effectively accounts for migrations due to finite resolutions. In the first step the spectrum was derived assuming the H4a model. The result was fitted by the sum of three power-law functions each with an exponential cutoff. The fitted spectrum, keeping the fractional contributions of the elemental groups as in the H4a model, was used for the simulation of the next step efficiencies and energy conversions. The spectrum derived in this first iteration step showed no significant difference to the one derived using the original H4a model meaning that the iterative unfolding converged already after one iteration. The same algorithm was applied starting with a featureless power-law spectrum with an H4a composition. In this case the spectrum converged after two iterations.

## 4.5 Systematics

There are four major systematic uncertainties on energy estimation that were accounted for in this analysis. All systematic uncertainties on primary energy were propagated to flux. When calculating different systematics, all conditions except the systematics under investigation, are kept the same.

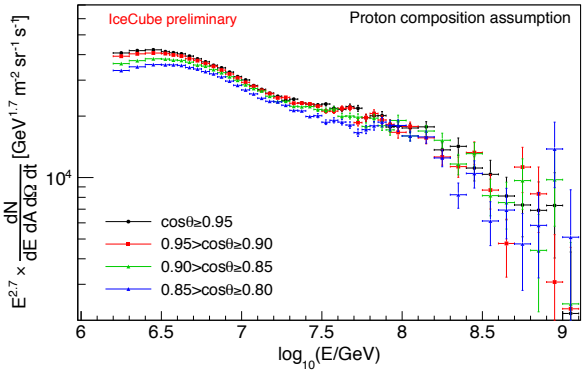


(a) Proton.

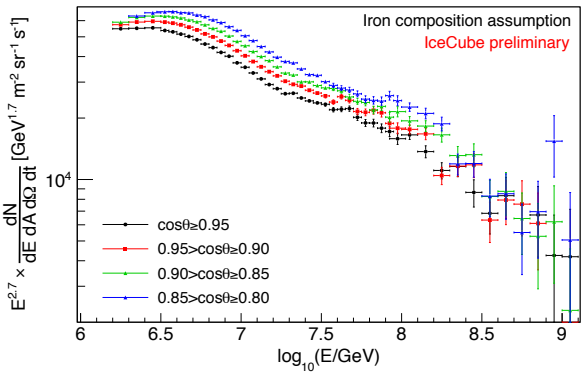


(b) Iron.

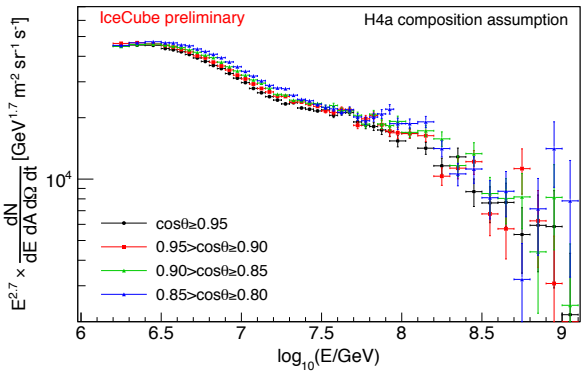


(c) H4a.

**Fig. 3**: Cosmic ray energy spectrum for 3 composition assumptions and 4 zenith ranges.

*Uncertainty in VEM calibration*

The measured charge of each IceTop tank is calibrated using the signal due to atmospheric muons [2]. From simulation studies a 3% uncertainty on the charge callibration and thus on the absoulute energy scale was found [5]. This uncertainty on absolute charge calibration translates into an absolute uncertainty in the signal, $S_{125}$, and consecutively in the energy. We propagate this uncertainty to primary energy and flux.

*Uncertainty in snow correction*
The systematic error due to snow correction arises from the uncertainty in the correction parameter $\lambda$. In the analysis we used $\lambda$ =2.1 m and the uncertainty is $\pm$0.2 m. The error in $S_{125}$ is estimated from the difference between shower size spectra derived using $\lambda = 1.9$ m and $\lambda = 2.3$ m. This error is propagated to an error in energy using the same $S_{125}$-to-$E_{true}$ conversion (Eq.4) for all three $S_{125}$ spectra.
*Difference between SYBILL 2.1 and QGSJET II*
To compare two interaction models, $S_{125}$-to-$E_{true}$ relations were recalculated using the smaller simulated sets with QGSJET II as the interaction model. Comparison of the $S_{125}$-to-$E_{true}$ relations show that for a given $S_{125}$, QGSJET II simulation results in lower energies compared to SYBILL 2.1. The largest difference is $\Delta\log(E/\mathrm{GeV}) = 0.02$, meaning that for the same primary energy QGSJET produces larger $S_{125}$ signal compared to SYBILL 2.1.
*Uncertainty and composition dependence*
The method used in this analysis requires a predefined composition assumption to translate the measured $S_{125}$ spectrum to the primary energy spectrum. In addition to the baseline scenario, the mixed composition H4a, we considered 4 differnet composition assumptions (pure proton, pure helium, pure oxygen and pure iron), to estimate the impact of the composition uncertainties to the all-particle spectrum.

Assuming that the cosmic ray directions are isotropically distributed, the measurement of the spectrum in different zenith ranges should yield the same result for each zenith. For a given energy, protons or light nuclei penetrate deeper into the atmosphere compared to heavy nuclei like iron. Heavy nuclei start to interact higher in the atmosphere and showers will be at a different stage of development at the detector level compared to the light nuclei. When looking at large zenith angle events, one effectively increases the amount of atmosphere that showers need to traverse to get to the detector. This information is sensitive to composition.

Reconstruction of the experimental data assuming pure proton and pure iron compositions in four zenith ranges are shown in Figs. 3(a) and 3(b). It can be seen that for a pure proton assumption the most inclined spectrum ($0.80 \leq \cos\theta < 0.85$) is systematically lower than vertical spectrum ($\cos\theta \geq 0.95$), in the energy range where statistics are not an issue. While for pure iron assumption it is the opposite, the inclined spectrum is systematically higher than vertical.

Four zenith spectra for the mixed, H4a, composition assumption can be seen in Fig. 3(c). Compared to pure proton and pure iron , H4a assumption leads to a smaller difference between vertical and inclined spectra, but still not zero. To estimate the systematic uncertainty in the all-particle energy spectrum due to composition, we use the differences for the H4a assumption between the final (Eq.5 with $\cos\theta_{min} = 1.0$, and $\cos\theta_{max} = 0.8$) and the vertical ($\cos\theta \geq 0.95$) spectra, and the final and the inclined ($0.80 \leq \cos\theta < 0.85$) spectra in the energy range $6.2 < \log_{10}(E/\mathrm{GeV}) < 7.5$ where statistical fluctuations are negligible. The largest difference between spectra is taken as a fixed value for the error due to composition across all energies as a conservative estimate.

## 5 Results and discussion

The final spectrum is shown in Fig.4. The IceTop Shower Size parameter, $S_{125}$, is calibrated against the true primary energy using the H4a composition model as an input to our simulations. We observe that, beyond our systematics, the all-particle cosmic-ray energy spectrum does not follow a single power law above the knee ($4.4 \pm 0.4$ PeV), but shows significant structure. The final spectrum was fitted by a simple power functions of the form

$$\frac{\mathrm{d}N}{\mathrm{d}\ln E\,\mathrm{d}A\,\mathrm{d}\Omega\,\mathrm{d}t} = I_0 \left(\frac{E}{1\,\mathrm{GeV}}\right)^{-\gamma+1}, \qquad (8)$$

in four different energy ranges. The break points in the spectrum are defined as the intersection of the fitted power functions.

The spectral index before the knee is $-2.63 \pm 0.01 \pm 0.06$, and changes smoothly between 4 to 7 PeV to $-3.13 \pm 0.01 \pm 0.03$. Another break is observed at around $18 \pm 2$ PeV, above which the spectrum hardens with a spectral index of $-2.91 \pm 0.01 \pm 0.03$. A sharp fall is observed beyond $130 \pm 30$ PeV with a spectral index of $-3.37 \pm 0.08 \pm 0.08$. The power function fits to the spectrum and their parameters are shown in Fig.4.

In summary, we have obtained a measurement of the cosmic-ray energy spectrum with an energy resolution of 20% below 10 PeV and less than 13% above 10 PeV. Systematic uncertainty is the main error on flux and is no more than $\pm$9%. The hardening of the spectrum around 18 PeV and steepening around 130 PeV is a clear signature of the spectrum and can not be attributed to any of the systematics or detector artefacts.

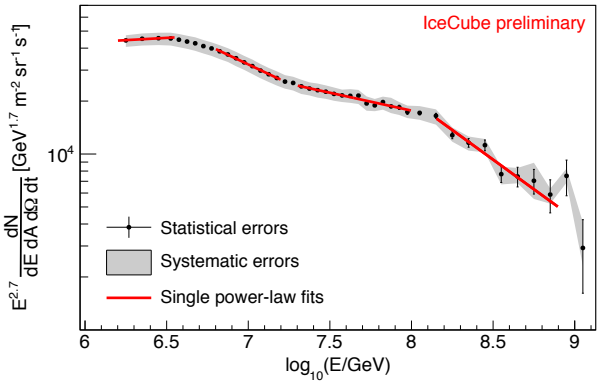


**Fig. 4**: Spectral fits in different energy ranges. Shaded area represents the systematic errors added in quadrature.

**Acknowledgment:**The ICRC 2013 is funded by FAPERJ, CNPq, FAPESP, CAPES and IUPAP.

## References

[1] T.K.Gaisser, Astropart. Phys. 35 (2012) 801-806
[2] R.Abbasi et al, Nucl. Instrum. Meth. A 700 (2013) 188-220
[3] R.Abbasi et al, Nucl. Instrum. Meth. (2009) 294-316
[4] R.Abbasi et al, Nucl. Instrum. Meth. (2010) 139-152
[5] A. Van Overloop, Proc. of the 32$^{nd}$ ICRC, Beijing (2011)
[6] D.Heck et al, report FZKA 6019 (1998)
[7] D.Heck, T.Pierog, `http://www-ik.fzk.de/corsika/usersguide/corsika_tech.html`
[8] E.Ahn et al, Physics Review D 80 (2009) doi:10.1103/PhysRevD.80.094003
[9] G.Battistoni et al, AIP Conf. Proc. 896 (2007) 31-49
[10] S.Ostapchenko, Nucl. Phys. B Proc. Suppl 151 (2006) 143-146
[11] S.Agostinelli et al, Nucl. Instrum. Meth A 506 (2003) 250-303

33RD INTERNATIONAL COSMIC RAY CONFERENCE, RIO DE JANEIRO 2013
THE ASTROPARTICLE PHYSICS CONFERENCE

ICRC 2013

# Ground Level Enhancement of May 17, 2012 Observed at South Pole

THE ICECUBE COLLABORATION[1]

[1]*See special section in these proceedings*

**Abstract:** Amundsen Scott station, located at the geographic South Pole, is arguably the most sensitive surface location on Earth for the detection of solar energetic particles because of the combination of low geomagnetic cutoff and high altitude. Three complementary instruments are now in operation there. IceTop is an array of 162 ice Cherenkov detectors each comprising approximately 2000 kg of clear ice. Each detector is viewed by photomultipliers feeding rate scalers set to different threshold levels, typically counting 1 kilohertz and above. The array of thresholds in principle allows IceTop to determine the energy spectrum of the solar energetic particles. The South Pole neutron monitor, with a long operating history at this location, is a standard 3NM64. Additionally there is an array of bare neutron detectors (without lead shielding) referred to as the Polar Bares. The monitor and bares respond to successively lower energy particles than the Cherenkov detectors, extending the spectral response. In this work we examine the Ground Level Enhancement (GLE) of May 17, 2012, related to an M5.1 solar flare, which was the first GLE in this solar cycle and the first one since December 2006. We estimate the energy spectrum of the solar particles and interpret the result in the context of observations from the global neutron monitor network. **Corresponding authors:** Takao Kuwabara[2], Paul Evenson[2]

[2] *University of Delaware, 217 Sharp lab, Newark DE 19711, USA*

**Keywords:** IceCube, IceTop, Neutron Monitor, Ground Level Enhancement, Solar Flare

## 1 Introduction

The Amundsen Scott station is located at the geographic South Pole. With its unique position of high altitude (2835m) and nearly zero geomagnetic cut-off, cosmic ray detectors located there can resolve solar and galactic cosmic ray disturbances with unprecedented detail. Three complementary instruments are now in operation there. One is a standard 3NM64 neutron monitor [1] and another is an array of 12 bare (without lead) neutron detectors referred to as the Polar Bares.

The third is IceTop, the surface component of the IceCube Neutrino Observatory, which is an air shower array consisting of 162 ice Cherenkov "tank" detectors, each 90 cm deep and each with a surface area of 2.7 $m^2$. In each tank the Cherenkov light is measured by two Digital Optical Modules (DOM), one operated at high gain and the other at low gain to provide sufficient dynamic range to cover both large and small air showers. For the analysis of solar events, we use counting rates from two discriminators in each high gain DOM. For historical reasons the discriminators are termed SPE (Single Photo Electron) and MPE (Multi Photo Electron). The SPE discriminators are in fact set to thresholds ranging from below one photoelectron to over 20 photoelectrons. All of the MPE discriminators are set to a threshold of approximately 20 photoelectrons as needed for air shower detection. Counting rates of the SPE discriminators range from 1 to 15 kHz. Those SPE and MPE discriminator rates are affected by the different amount of snow that has accumulated on each tank [2].

In a ground based cosmic ray detector the fine details of the primary spectrum at the top of the atmosphere for solar physics work are lost but, particularly at South Pole, a surprising amount of information remains. Yield functions, with units area-solid-angle, describe the relation between particle flux at the top of the atmosphere and a particular counting rate. They depend on particle arrival direction, rigidity, mass of the primary nucleus and detector characteristics. At high latitudes such as South Pole, defocusing in the geomagnetic field produces a nearly isotropic flux at the top of the atmosphere even if the flux outside the magnetosphere is highly anisotropic. At low energy (when the probability of a particle or its progeny to reach the surface is small), the yield function is smaller than the physical area-solid-angle of the detector, but at high energy (when a shower can give rise to a signal even if the extrapolated trajectory of the primary passes outside the detector) it can be larger. The yield function of the Polar Bares peaks at lower energy than that of the 3NM64. IceTop yield functions peak at still higher energies, with each discriminator threshold producing a different yield function.

In this paper we examine the Ground Level Enhancement (GLE) of May 17, 2012, related to an M5.1 solar flare, which was the first GLE in this solar cycle and the first one since December 2006. By using calculated and measured yield functions for the various detectors we are able to deconvolute the different discriminator counting rates to produce an estimate of the energy spectrum of the solar particles and interpret the result in the context of observations from the global neutron monitor network.

## 2 GLE Observation from the Neutron Monitor Network

An overview of the GLE as seen in the neutron monitor network is shown in Figure 1. Onset was around 1:50 UT at Apatity and Oulu, both of which had viewing directions close to the inferred sunward direction of the interplanetary magnetic field (IMF). Mawson, which actually views closer

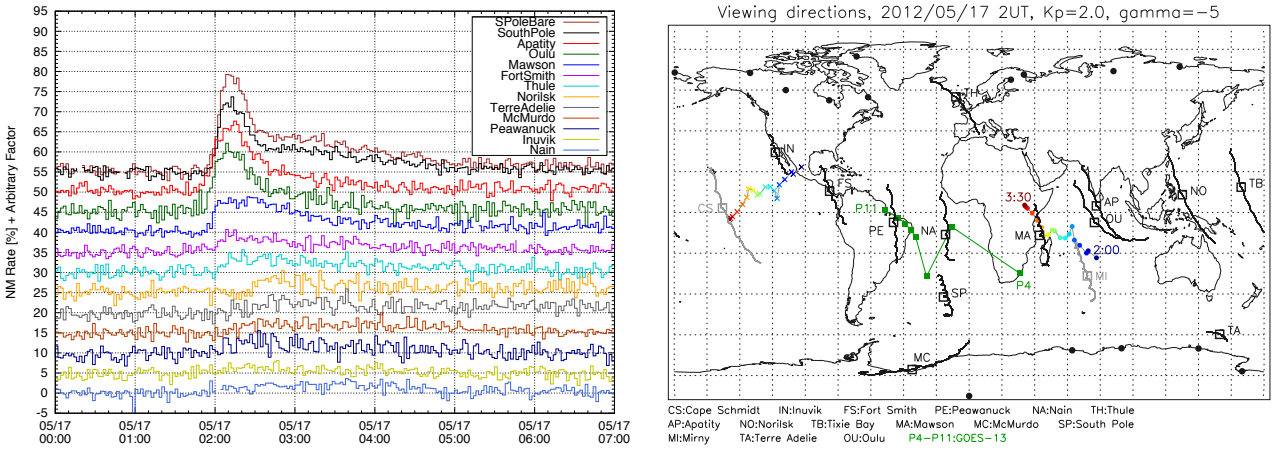


**Figure 1**: Percent increases, relative to the count rate averaged from 01:00 to 01:30 UT of 13 high latitude neutron monitors with arbitrary values added to separate the traces [3, 4] (left) and viewing directions for an assumed $P^{-5}$ particle spectrum calculated for 2:00 UT (right). Solid circles show station locations, squares show asymptotic viewing directions for a median energy particle, and lines show the range of viewing directions for the central 80% of the detector energy response. Viewing directions for the GOES-13 P4-P11 channels are also shown. The IMF direction at Earth [5] from 2:00 to 3:30 UT is shown as a series of colored marks, solid circles for the sunward direction and x marks for the anti-sunward.

to the inferred field direction also saw a fast rise however the peak was not clearly observed and intensity was about half of others (8%). It is not unusual to see an offset of the peak fluxes from the inferred field direction. Other stations with less favorable viewing directions saw smaller enhancements as is typical. The South Pole NM64 and Polar Bare increases started a few minutes after Apatity and Oulu and showed a clear pulse like enhancement ($\geq$15%) with a peak just after 2:00 UT even though their viewing direction is more comparable to that of Peawanuck and Nain, which saw relatively small increases. All of those stations see broader enhancements ($\geq$ 5%) behind the pulse. Other stations see only broad enhancements but with small ($\leq$ 5%) amplitudes.

## 3 GLE Observation at South Pole

Figure 2 compares the GLE observed at South Pole with data from the GOES-13 spacecraft [6] which had a similar asymptotic direction. IceTop rates are average counting rate of several discriminators. SPE1 and SPE2 are the average of the lower 62 and higher 100 SPE discriminator thresholds respectively, while MPE is the average of all 162 MPE discriminators. We can see that lower threshold discriminators have larger percentage increases. The Bare count rates also have a larger percentage increase than the NM64 rates because they respond more to lower energy particles and the solar spectrum is softer than the galactic cosmic ray spectrum. We can see that IceTop and neutron monitors both saw the clear pulse and subsequent broad enhancement. In this preliminary analysis we use the counting rates of the multiple discriminator thresholds in IceTop and the different neutron detectors to derive the energy spectrum of the solar particles during the initial pulse of the event.

### 3.1 Neutron Monitor Polar Bare Analysis

If we assume that the galactic cosmic ray flux is constant during the baseline interval and throughout the enhancement, the neutron monitor counting rate increase at the location of geomagnetic cut-off rigidity $P_c$ is expressed as

$$\Delta N(P_c) = \int_{P_c}^{\infty} S(P) \cdot J_{sep}(P) dP \qquad (1)$$

where $S(P)$ is the neutron monitor yield function and $J_{sep}(P)$ is the primary solar energetic particle (SEP) spectrum. By assuming a simple power law SEP spectrum as $J_{sep}(P) = J_0 P^{-\gamma}$, the ratio of rate increases of Bare to NM64 can be expressed as a function of $\gamma$

$$\frac{\Delta N_{Bare}}{\Delta N_{NM64}} = \frac{\int_{P_c}^{\infty} S_{Bare} \cdot P^{-\gamma} dP}{\int_{P_c}^{\infty} S_{NM64} \cdot P^{-\gamma} dP} \qquad (2)$$

Response functions for Bare $S_{Bare}$ and NM64 $S_{NM64}$ are determined in [7] from Dorman functions $N(P) = N_0(1 - exp(-\alpha P^{-k}))$ which have parameters $N_0$=157.68, $\alpha$=7.846, and $k$=0.940 for Bare, and $N_0$=151.67, $\alpha$=8.415, and $k$=0.894 for NM64.

We then follow [8] to derive the spectrum of the solar particles. Spectral parameters shown in the bottom two panels of Figure 2 are determined every 10 min from 2:00 to 4:30 (points), along with a 15 min average from 02:05 to 02:20 UT for the pulse and a 60 min average from 02:35 to 03:35 UT for the broad enhancement (bars). These averages and time intervals are used in the subsequent comparison with IceTop. We derive a somewhat harder spectrum for the pulse ( $J_{sep}(P) = 1.14 \cdot P^{-4.3}$(cm$^2$ s sr GV)$^{-1}$, P in GV ) than for the broad enhancement ( $J_{sep}(P) = 0.673 \cdot P^{-4.9}$(cm$^2$ s sr GV)$^{-1}$, P in GV ).

### 3.2 IceTop Analysis

Figure 3 shows the increase in counting rate of individual IceTop discriminators averaged over 15 min from 02:05 to 02:20 UT. These increases are plotted as a function of the base count rates defined as an average count rate from 01:00 to 01:30 UT. Discriminators with higher base count rates (lower threshold settings) have larger increases. In

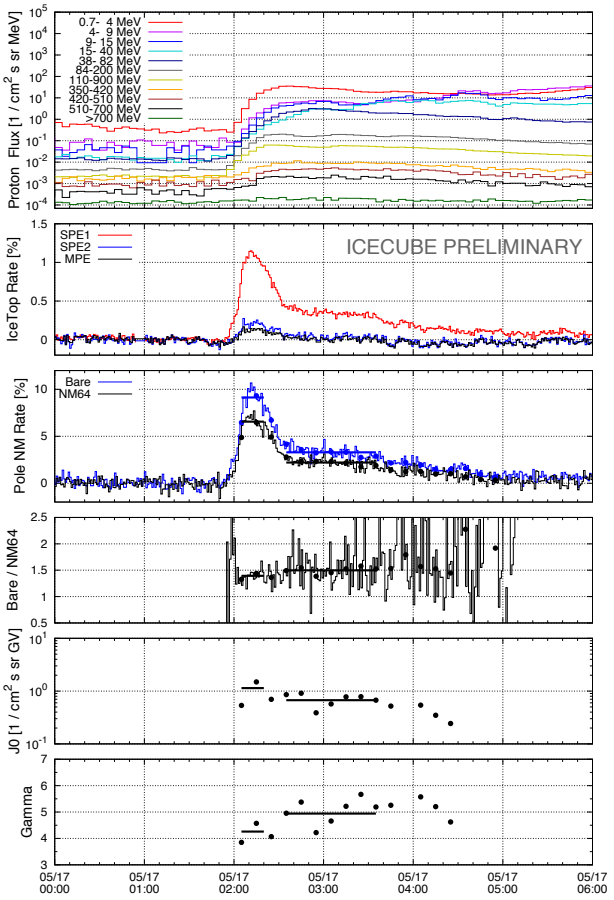


**Figure 2**: GLE observation at South Pole and GOES. From top panel, GOES-13 proton channel, IceTop rates, South-Pole neutron monitor rates, ratio of Bare/NM64 monitor, estimated parameters of primary spectrum from "Polar Bare" analysis as amplitude $J_0$ and exponent $\gamma$ of a power law in momentum.

order to derive a spectrum from the counting rates we must determine a separate yield function for each discriminator. The yield functions must minimally take into account the discriminator setting, characteristics of the tank, barometric pressure and snow cover, all on an individual basis.

Determining a complete set of yield functions is a work in progress. We are presently engaged in adapting the extensive simulation apparatus developed to analyze air showers with IceTop [10]. Significant modification is required because the minimum signal accepted in the air shower analysis corresponds to the MPE threshold, approximately 20 photoelectrons, whereas most of the information on solar events comes from signals with amplitudes below this. Simulation of signals above 20 photoelectrons is well developed on an integrated charge basis, whereas at lower levels the shape of the waveform becomes more irregular and the treatment must be on a voltage amplitude basis. In Figure 3 note the rather regular behavior of the increases for base rates below 4 kHz and the markedly different behavior to the right of this. The threshold producing a base rate of 4 kHz is predicted by the integrated charge calibration to correspond to 3 photoelectrons which defined as the half of the maximum value of the charge distribution [10]. Observationally however, 4 kHz is clearly the true single photoelectron threshold. Lower thresholds produce increasing base rates as they go deeper into the electronic noise but the enhancements during the event do not get larger as one photoelectron is the minimum signal that can be generated physically.

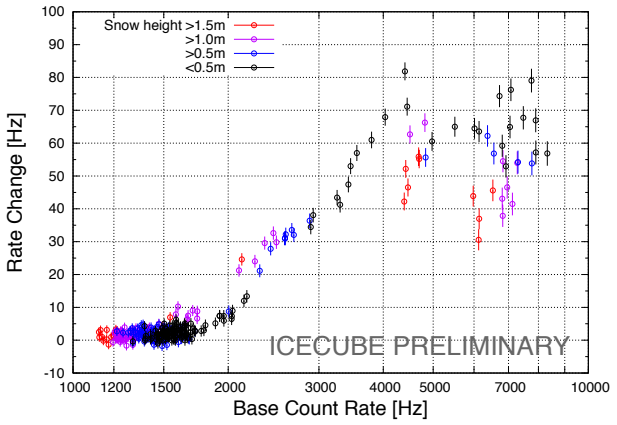


**Figure 3**: Increase of individual IceTop discriminator counting rates during the pulse above the base count rates (defined as the average count from 01:00 to 01:30 UT). Different colors correspond to different snow overburden.

Until the more tailored calculations of yield functions are available we must be content to make phenomenological corrections to the data. One such correction is already implicit in Figure 3 where we have corrected all of the data for barometric pressure using multiplicative factors derived for the base rates. We can also easily derive a phenomenological correction of the snow effect to the base counting rate, this time an additive correction. When applied, as in Figure 4, this results in a much more aesthetic ordering of the data. However clear trends remain in the increases related to snow depth, as one might expect.

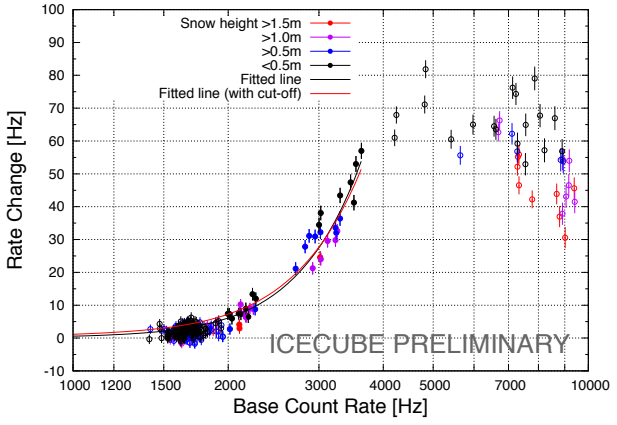


**Figure 4**: Increase of individual IceTop discriminator counting rates during the pulse above snow corrected base count rates. Black and red lines are the best fit to a power law and a power law with exponential cut-off spectrum.

At this point we return to the technique employed in our analysis of the 2006 December 13 event [11] where we used generic yield functions (in the sense that they were

calculated for nominal tank properties, no snow overburden, and a single barometric pressure) for various discriminator settings from FLUKA simulations [12]. We derive the yield function $S_i$ for each discriminator $i$ from its snow corrected base count rate $N_i^{base}$ and an assumed galactic cosmic ray spectrum $J_{gcr}$ as

$$N_i^{base} = \int S_i(P) J_{gcr}(P) dP. \quad (3)$$

We can then determine the simple power law SEP spectrum $J_{sep}$ by using a least squares fitting technique to minimize,

$$\chi^2 = \sum_i \{ \frac{1}{\sigma^2_{\Delta N_i}} [\Delta N_i - \int S_i(P) J_{sep}(P) dP]^2 \}, \quad (4)$$

where $\Delta N_i$ is the rate changes in $i$-th discriminator. We apply the fitting to the discriminator for which the base count rate is higher than 2 kHz where we see large rate increases. From the FLUKA simulation 3.6 kHz is the rate at the single photoelectron setting, so discriminators with higher base rates are excluded from the analysis. The derived power law spectrum of IceTop is $J_{sep}(P) = 16.3 \cdot P^{-8.7}$(cm$^2$ s sr GV)$^{-1}$, P in GV. The black line in Figure 4 shows the fitted enhancements.

## 4 Results

The upper panel of Figure 5 summarizes different determinations of the spectrum. The solid line is the spectrum from the Neutron Monitor Polar Bare analysis with the heavier line denoting the range that contains central 80% of the energy response of the monitors to the solar particles. The points show measurement of the SEPs from the GOES-13 spacecraft. The basic consistency of the two measurements is similar to that obtained in an analysis of multiple events by [13]. The broken line from the power law fit of the IceTop analysis is not consistent with the Polar Bare analysis. The most probable explanation is that the true spectrum exhibits a major steepening and therefore cannot be adequately represented by a power law in rigidity in either detector.

To explore this possibility we assume an exponential cut-off in rigidity of the spectrum from the Polar Bare analysis, with three free parameters. We find $J_{sep} = J_0 P^{-4.3} \exp(-P/0.78)$, P in GV as shown in the lower panel of Figure 5. Normalization factors are separately determined as $J_0^{NM} = 14.9$ and $J_0^{IceTop} = 25.7$ (cm$^2$ s sr GV)$^{-1}$. This difference is not unexpected because their yield functions are not from same framework. This difference indicates the level of systematic uncertainty in the present analysis. The best fit of IceTop data to this spectrum is shown in Figure 4 as a red line. Observed increases of Bare and NM64 during the pulse shown in Figure 2 are 9.13% and 6.56%, whereas the fit gives 9.82% and 6.03% respectively.

**Acknowledgment:** We acknowledge the NMDB database (www.nmdb.eu), founded under the European Union's FP7 programme (contract no. 213007) for providing neutron monitor data of Terre Adelie - French Polar Institute (IPEV), France, Oulu - University of Oulu, Finland, Apatity - Polar Geophysical Institute, Russia, and Norilsk - Institute of Solar-Terrestrial Physics (ISZF), Russia. We also thank Marc Duldig and IPS Radio and Space Services, Bureau of Meteorology, Australia for providing Mawson neutron monitor data. We thank John Bieber, John Clem, David Ruffolo, Roger Pyle and Alejandro Saiz for scientific discussions and for help with preparing the data from the University of Delaware neutron monitors. In addition to US National Science Foundation support for IceCube, the South Pole neutron detectors operated under award ANT-0838839 and the McMurdo neutron monitors under ANT-0739620 .

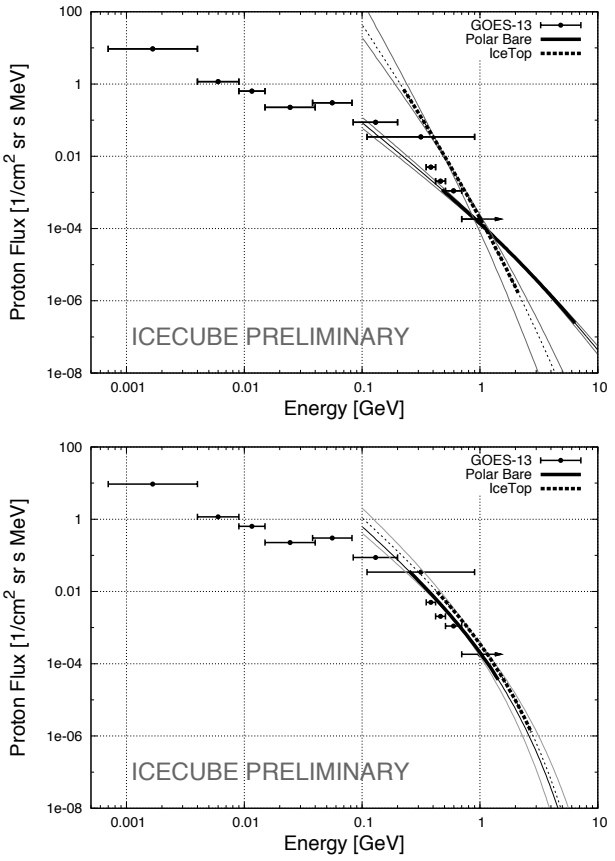


**Figure 5**: Proton spectrum determined from the Neutron Monitor Polar Bare analysis (line) and the IceTop analysis (broken line) during the pulse. Upper panel shows the two power law fits. Bottom panel shows fits for the spectrum with a cut-off. The gray lines represent the statistical uncertainties. The points are the proton fluxes from GOES-13 spacecraft data.

## References

[1] P. H. Stoker, L. I. Dorman, and J. M. Clem, Space Science Reviews 93 (2000) 361-380.
[2] IceCube Collaboration, paper 1106, these Proceedings.
[3] http://www.nmdb.eu/
[4] Duldig, M. (private communication, 2013)
[5] http://omniweb.gsfc.nasa.gov
[6] http://www.swpc.noaa.gov/Data/goes.html
[7] P. H. Stoker, Proc. 19th ICRC, La Jolla, 4 (1985) 114-117.
[8] J. W. Bieber and P. Evenson, Proc. 22nd ICRC, Dublin, 3 (1991) 129-132.
[9] J. W. Bieber and P. Evenson, Proc. 24th ICRC, Roma, 4 (1995) 1316-1319.
[10] R. Abbasi et al., IceCube Collaboration, NIM-A 700 (2013) 188-220.
[11] R. Abbasi et al., IceCube Collaboration, The Astrophysical Journal Letters 689 (2008) L65-L68.
[12] J. M. Clem, P. Niessen, and S. Stoyanov, Proc. 30th ICRC, Merida, 1 (2007) 237-240.
[13] S. Oh, J. W. Bieber, J. M. Clem, P. Evenson, R. Pyle, Y. Yi, and Y.-K. Kim, Space Weather (2012), doi:10.1029/2012SW000795.

33RD INTERNATIONAL COSMIC RAY CONFERENCE, RIO DE JANEIRO 2013
THE ASTROPARTICLE PHYSICS CONFERENCE

ICRC 2013

# An update on cosmic-ray anisotropy studies with IceCube

THE ICECUBE COLLABORATION[1],

[1]*See special section in these proceedings*

*santander@icecube.wisc.edu*

**Abstract:** The IceCube neutrino observatory detects energetic muons from the interaction of TeV cosmic rays with the Earth's atmosphere at a rate of about 2 kHz. The integration of this high rate over the course of several years of operation has provided us with a data set of several billion events with cosmic-ray energies between 20 and 400 TeV. A data set of this size, combined with the degree-scale angular resolution of IceCube for cosmic-ray muons, can be used to search for anisotropy in the arrival direction of cosmic rays at the per-mille level or lower. Previous studies based on data taken with partial configurations of IceCube show significant anisotropy over a wide range of angular scales in two energy bands of about 20 TeV and 400 TeV. We present an update on studies using all currently available cosmic-ray data from IceCube, which consist of 150 billion events collected between 2007 and 2012.

**Corresponding authors:** M. Santander[1], P. Desiati[1], S.Y. BenZvi[1], S. Westerhoff[1]
[1]*Wisconsin IceCube Particle Astrophysics Center, University of Wisconsin, Madison, WI 53706, U.S.A.*

**Keywords:** Cosmic rays, Anisotropy, IceCube.

## 1 Introduction

Several years of observations from tens of GeV to PeV energies have shown that cosmic rays arrive at the Earth with a small anisotropy of order $10^{-4} - 10^{-3}$. The most prominent feature in the anisotropy is a large angular scale structure of per-mille amplitude that is usually described as a dipole. Significant structure is also present with a smaller amplitude and characteristic angular sizes between $15^{\circ}$ and $30^{\circ}$. In addition, the topological structure of the anisotropy changes at energies in excess of approximately 100 TeV, often interpreted as a change in phase of the dipole component of the global anisotropy [1].

IceCube collects a large number of cosmic-ray induced muon bundles (see section 2). The high degree of alignment of the muons with the parent cosmic ray particles enables the study of the distribution of cosmic-ray arrival directions at a level of about $10^{-5}$. The median energy of cosmic rays producing the muons collected by IceCube is about 20 TeV. Higher energies can be reached by selecting for larger events. IceCube provided the first sky map of the cosmic ray arrival direction up to 400 TeV median energy range from the southern hemisphere [2, 3], confirming the topological change in the observed anisotropy. With the IceTop air-shower array it was possible to determine the anisotropy up to about 2 PeV [4]. The sky map obtained by subtracting the large angular scale components (a dipole and a quadrupole in spherical harmonics) from the data [5], shows significant small angular scale structures in the cosmic ray anisotropy, similarly to observations in the northern hemisphere [6, 7].

In this paper we present an update on previous cosmic ray anisotropy studies using data collected by IceCube from June 2007 to May 2012. First, we calculate the angular power spectrum of the cosmic-ray map to search for anisotropy over a wide angular range. We then concentrate on the study of the anisotropy at very small angular scales by fitting and subtracting the large scale structure from the map. Finally, we present the resulting sky maps of cosmic ray arrival distributions.

A separate analysis of the stability of the large scale anisotropy with time is also presented in these proceedings [8].

## 2 The IceCube Observatory

The IceCube neutrino telescope [9] consists of a cubic-kilometer array of 5160 Digital Optical Modules (DOMs) deployed on 86 vertical cables, or *strings*, between depths of 1450 m and 2450 m in the glacial ice sheet at the geographic South Pole. In this work, IceCube is used as a cosmic-ray detector by exploiting its sensitivity to energetic muons produced in the interaction of cosmic rays with the Earth's atmosphere. The Cherenkov light emitted by energetic muons as they propagate through the ice is recorded by DOMs. The amplitude and timing of the light signals can be used to reconstruct the arrival direction of the muons and therefore of their parent cosmic-ray particle.

IceCube was operated in partial configurations from the beginning of detector construction in 2005 until the completion of the detector in 2010. Partial configurations were labeled according to the number of active strings of DOMs that were deployed in the ice at the time. For instance, the final configuration of IceCube (called IC86) consists of 86 detector strings. A list of the detector configurations used in this work is given in Table 1.

## 3 Data selection

Events in IceCube are recorded using a simple multiplicity trigger that requires coincident hits in eight DOMs within a 5 $\mu$s window. All locally-coincident hits within a $\pm 10\,\mu s$ window are recorded for each trigger, and overlapping windows are merged. The trigger rate shows a seasonal modulation of $\pm$ 10% over the year due to changes in

| Detector | Start | End | Live-time (days) | No. of events ($\times 10^9$) |
|---|---|---|---|---|
| IC22 | 06/2007 | 04/2008 | 269.4 | 5.3 |
| IC40 | 05/2008 | 05/2009 | 335.6 | 18.9 |
| IC59 | 06/2009 | 06/2010 | 335.0 | 33.8 |
| IC79 | 06/2010 | 05/2011 | 299.7 | 39.1 |
| IC86 | 05/2011 | 05/2012 | 332.9 | 52.9 |
| *Total* | | | | 150 |

**Table 1**: Detector configurations that were used to collect the data analyzed in this work. The final configuration of IceCube consists of 86 strings of DOMs deployed in the ice (IC86), each partial configuration is indicated as "IC" followed by the number of deployed strings that participated in the data acquisition during each period.

atmospheric conditions that affect muon production in air showers. The average trigger rate for the IC86 configuration is about 2.7 kHz. The integration of this high rate of cosmic-ray muons over a period of about five years results in a combined data set of about 150 billion events that is used in this work to search for cosmic ray anisotropy.

The anisotropy search relies on a precise estimate of the arrival direction of each cosmic-ray event. A first estimate of the event arrival direction is obtained using a $\chi^2$ linear-track fit to the DOM hits pattern. This coarse estimate is used as a seed for a more complex likelihood-based algorithm that implements some aspects of the light generation and propagation in the ice. Simulation studies indicate that the median angular resolution of this algorithm is about $3^\circ$. In this analysis, we only consider muon events with a reconstructed zenith angle of less than $70^\circ$, which limits our sky exposure to the declination range $-90^\circ < \delta < -20^\circ$. The angular resolution degrades very quickly for events with a larger zenith angle.

Due to the high trigger rate, only a very limited amount of data is stored and transmitted for each cosmic-ray event. A compact Data Storage and Transfer (DST) format is used to store the results of the online likelihood reconstruction together with a selected list of event variables. This data is transmitted from the South Pole via the South Pole Archival and Data Exchange (SPADE) satellite communication system. Given its high statistics and reasonable angular resolution, we use the DST data set for cosmic-ray anisotropy studies.

The median energy of the DST set is about 20 TeV and was determined using simulations of air showers generated using the Corsika Monte Carlo code [10].

## 4 Analysis method

The anisotropy results presented in this work are an update on a previous analysis performed with IC59 data and reported in [5]. A brief explanation of the analysis method is given here; the reader is referred to the reference for additional details.

The search for anisotropy is conducted by searching for deviations of the sky map of reconstructed equatorial coordinates of cosmic-ray events from an isotropic reference sky map that accounts for detector exposure effects. The reference map is constructed from the data using the time-scrambling algorithm described in [11] for a scrambling period of 24 hours, which makes the search sensitive to all angular scales. During the time-scrambling procedure, each event is resampled 20 times to reduce the statistical fluctuations in the reference map.

The sky maps are constructed using the HEALPix[1] [12] pixelisation of the celestial sphere, which provides bins of equal solid angle. The selected HEALPix resolution ($N_{\rm side}$ = 64) divides the sphere into 49152 pixels with an average size of about $1^\circ$.

A relative intensity map of deviations of the data counts from the reference level is constructed using the expression $\delta I_i = (N_i - \langle N \rangle_i)/\langle N \rangle_i$, where $N_i$ and $\langle N \rangle_i$ are the number of observed events and the number of reference events in the $i^{\rm th}$ pixel, respectively. A smoothing procedure is applied to the data to increase the sensitivity of the search to structures with angular scales larger than the map pixel size. The smoothing process sums all events in each pixel to the events in all pixels contained within a certain angular distance (or "smoothing radius"). The statistical significance of any observed deviation with respect to the reference level is calculated according to [13].

## 5 Results

Similarly to what was presented in Ref. [5], an angular power spectrum of the relative intensity map was used to estimate the strength of the anisotropy over a wide range of angular scales. The power spectrum was calculated using the `PolSpice` software package[2] [14, 15] that corrects systematic effects introduced by the partial sky coverage of our data.

The spectrum, shown in Fig. 1, exhibits significant power at low-$\ell$ multipoles (i.e large angular scales). This dominant large scale feature has been previously reported by IceCube [2] and is usually described as the combination of the dipole ($\ell = 1$) and quadrupole ($\ell = 2$) modes of the spherical harmonic functions. In agreement with the results of the previous study, a significant departure from the isotropic level is also observed at angular scales roughly between $15^\circ$ and $30^\circ$ (i.e. for multipole between $\ell \sim 5$ and $\ell \sim 12$).

The improvement in statistics from the combination of all available IceCube data reveals a departure from isotropy at higher multipole modes than previously observed. The spectrum indicates that the relative intensity sky map should exhibit anisotropy up to angular scales below $10^\circ$ ($\ell \sim 20$).

The presence of small scale anisotropy is also evident in the one-dimensional projection of relative intensity as a function of right ascension shown in Fig. 2 for the declination range $-75^\circ < \delta < -35^\circ$.

In order to reveal the smaller scale anisotropy, the dipole and quadrupole terms of the spherical harmonic

1. http://healpix.jpl.nasa.gov
2. http://www2.iap.fr/users/hivon/software/PolSpice/

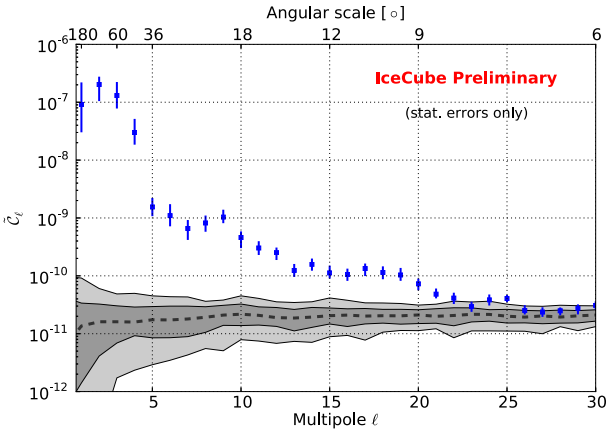


**Figure 1**: Angular power spectrum of the unsmoothed relative intensity map. Blue points show the power spectrum for the IceCube data. Error bars are statistical only. The gray bands indicate the distribution of power spectra for a large sample of isotropic maps, showing the 68% (dark) and 95% containing interval.

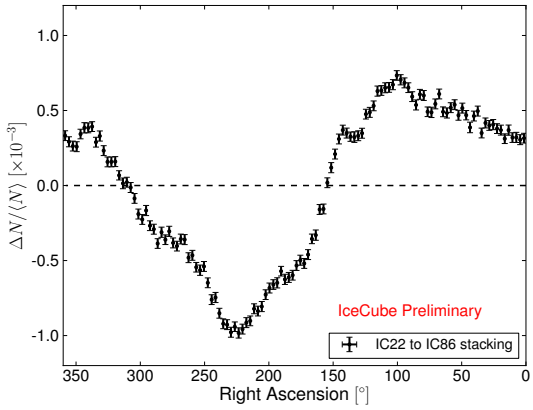


**Figure 2**: One-dimensional projection of relative intensity as a function of right ascension for the combined IceCube data set. A 3° binning was chosen to match the angular resolution of the cosmic ray sample. The uncertainties shown are only statistical.

functions were fit and subtracted from the relative intensity map. The best fit coefficients are given in Table 2 for the spherical harmonic fit functions in Ref. [5]. The residual maps were smoothed to search for small-scale anisotropy. A map of relative intensity after the dipole- and quadrupole-subtraction in shown in Fig. 3 for a smoothing radius of 20°. The map shows excellent agreement with the results of the previous analysis performed on IC59 data [5]. The IC59 set is also included in this analysis and represents 22% of the total data set.

Maps of relative intensity and pre-trial statistical significance are shown in Fig. 4 before (Figs. 4a and 4b) and after (Figs. 4c and 4d) the dipole and quadrupole subtraction procedure for a 5° smoothing radius. The high significance of the small-scale structure shown in the dipole- and quadrupole-subtracted maps indicates for the first time the presence of anisotropy in the flux of TeV cosmic rays at angular scales of about 5°, close to the angular resolution of IceCube for cosmic rays.

| Coefficient | Value ($\times 10^{-4}$) |
|---|---|
| $m_0$ | $-0.05 \pm 0.82$ |
| $p_x$ | $3.01 \pm 0.28$ |
| $p_y$ | $-2.84 \pm 0.28$ |
| $p_z$ | $-0.08 \pm 1.42$ |
| $Q_1$ | $-0.03 \pm 0.64$ |
| $Q_2$ | $-2.69 \pm 0.20$ |
| $Q_3$ | $-8.14 \pm 0.20$ |
| $Q_4$ | $-2.01 \pm 0.09$ |
| $Q_5$ | $-4.77 \pm 0.09$ |

**Table 2**: Dipole and quadrupole coefficients for the best fit to the relative intensity map. The indicated uncertainties are statistical only. A good agreement is found between these values and those reported in [5].

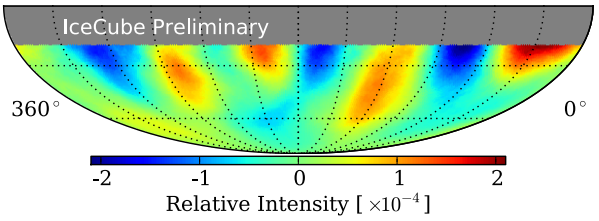


**Figure 3**: Dipole- and quadrupole-subtracted relative intensity map for a smoothing radius of 20°. The structure observed in this map shows good agreement with IC59 results [5].

## 6 Discussion

An update is presented on the study of cosmic ray anisotropy at TeV energies with the IceCube detector. In this work, we use a sample of about 150 billion events collected with IceCube in several detector configurations over a period of five years.

The analysis of this sample reveals the presence of significant anisotropy with amplitudes at per-mille level and lower over a wide range of angular scales. The observed large-scale component of the anisotropy shows good agreement with previous results. Smaller scale structure is revealed in this analysis by fitting and subtracting the dipole and quadrupole terms of the spherical harmonic functions.

In addition to the anisotropy observed in the IC59 analysis with typical sizes between 15° and 30°, new structure with an angular scale of about 5° degrees is revealed in the cosmic ray flux. This observation represents the first detection of TeV anisotropy at such a small angular scale, close to the angular resolution of IceCube for cosmic rays.

The origin of the observed cosmic ray anisotropy is not known, and further full sky observations as a function of energy, primary mass and possible correlations with spectral anomalies are necessary to probe deeper into the origin of the observations. It is possible that the anisotropy is a signature of the discreet random distribution of nearby galactic sources of cosmic rays. The energy dependence of the anisotropy structure could arise from the dominance of one or another source at different energies mainly due to differences in ages of the cosmic ray accelerators [16, 17,

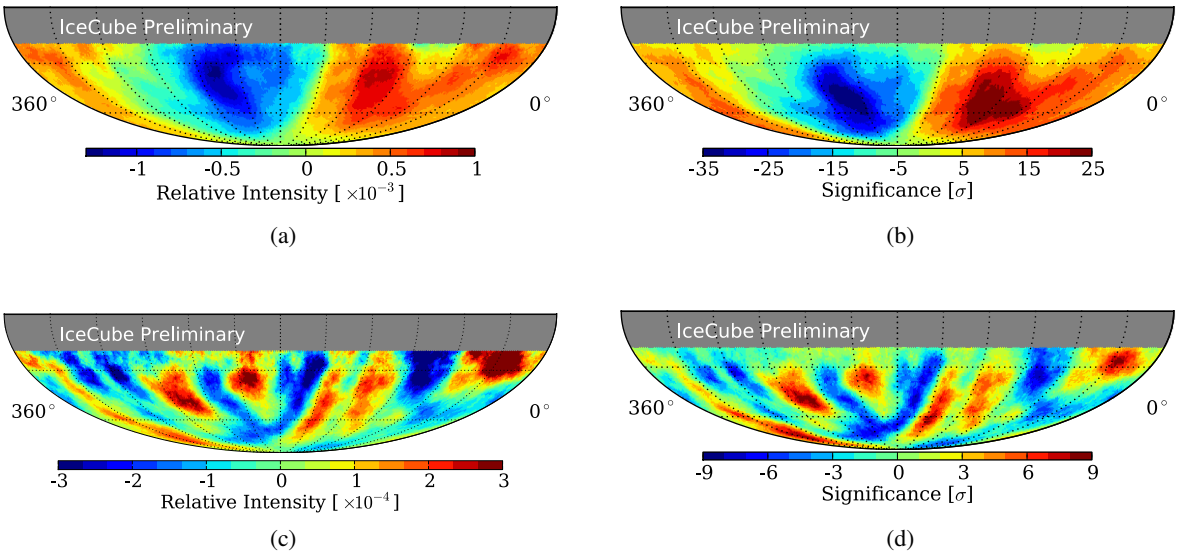


**Figure 4**: Relative intensity and pre-trial statistical significance maps in equatorial coordinates for the combined IceCube data set. The maps are shown before (*top*) and after (*bottom*) the dipole- and quadrupole subtraction procedure. A 5° smoothing radius was used for all maps. The maps show an anisotropic structure that is statistically significant at an angular scale of about 5°.

18]. Although current models of cosmic ray propagation in the interstellar medium predict a dipole anisotropy, some astrophysical interpretations of the small scale anisotropy were provided as well [19, 20]. On the other hand, the small scale structure of the anisotropy might simply be an effect of the turbulent interstellar magnetic field in our vicinity [21]. The local interstellar magnetic field is thought to be associated to the Loop I shell expanding from the Scorpion-Centaurus Association and to be relatively regular up to several tens of parsec [22], i.e. the order of magnitude of the estimated proton mean free path in the interstellar medium [23]. Cosmic-ray protons with energy 1-10 TeV happen to have a gyro-radius of the order of the heliospheric size, therefore it is possible that the interstellar magnetic field perturbed by the heliosphere provides significant pitch angle scattering to influence and re-distribute the arrival directions [24, 25, 26].

## References

[1] M. Aglietta et al., Astrophys. J. Lett. 692 (2009) L130 doi:10.1088/0004-637X/692/2/L130.
[2] R. Abbasi et al., Astrophys. J. 718 (2010) L194 doi:10.1088/2041-8205/718/2/L194.
[3] R. Abbasi et al., Astrophys. J. 746 (2012) 33 doi:10.1088/0004-637X/746/1/33.
[4] M. G. Aartsen et al., Astrophys. J. 765 (2013) 55 doi:10.1088/0004-637X/765/1/55.
[5] R. Abbasi et al., Astrophys. J. 740 (2011) L16 doi:10.1088/0004-637X/740/1/16.
[6] A. A. Abdo et al., Phys. Rev. Lett. 101 (2008) 221101 doi:10.1103/PhysRevLett.101.221101.
[7] R. Iuppa et al., Nucl. Inst. Meth. A692 (2012) 160 doi:10.1016/j.nima.2012.01.012.
[8] IceCube Coll., paper 0411, these proceedings.
[9] A. Achterberg et al., Astropart. Phys. 26 (2006) 155 doi:10.1016/j.astropartphys.2006.06.007.
[10] D. Heck et al., Tech. Report FZKA 6019 (1998) Forschungszentrum Karlsruhe.
[11] D. E. Alexandreas et al., Nucl. Instr. Meth. A328 (1993) 570 doi:10.1016/0168-9002(93)90677-A.
[12] K. M. Gorski et al., Astrophys. J. 622 (2005) 759 doi:10.1086/427976.
[13] T. Li and Y. Ma, Astrophys. J. 272 (1983) 317 doi:10.1086/161295.
[14] I. Szapudi et al., Astrophys. J. 548 (2011) L115 doi:10.1086/319105.
[15] G. Chon et al., Mon. Not. Roy. Astron. Soc. 350 (2004) 914 doi:10.1111/j.1365-2966.2004.07737.x.
[16] A. D. Erlykin and A. W. Wolfendale, Astropart. Phys. 25 (2006) 183 doi:10.1016/j.astropartphys.2006.01.003.
[17] V. S. Ptuskin et al., Adv. Space Res. 37 (2006) 1909 doi:10.1016/j.asr.2005.08.036.
[18] P. Blasi and E. Amato, J. Cosmol. Astropart. Phys. 1/011 (2012) 11 doi:10.1088/1475-7516/2012/01/011.
[19] L. Drury and F. Aharonian, Astropart. Phys. 29 (2008) 420 doi:10.1016/j.astropartphys.2008.04.007.
[20] M. A. Malkov et al., Astrophys. J. 721 (2010) 750 doi:10.1088/0004-637X/721/1/750.
[21] G. Giacinti and G. Sigl, Phys. Rev. Lett. 109 (2012) 071101 doi:10.1103/PhysRevLett.109.071101.
[22] P. C. Frisch et al., Astrophys. J. 760 (2012) 106 doi:10.1088/0004-637X/760/2/106.
[23] H. Yan and A. Lazarian, Astrophys. J. 673 (2008) 942 doi:10.1086/524771.
[24] P. Desiati and A. Lazarian, Astrophys. J. 762 (2013) 44 doi:10.1088/0004-637X/762/1/44.
[25] A. Lazarian and P. Desiati, Astrophys. J. 722 (2010) 188 doi:10.1088/0004-637X/722/1/188.
[26] P. Desiati and A. Lazarian, Nonlinear Proc. Geoph. 19 (2012) 351 doi:10.5194/npg-19-351-2012.

33RD INTERNATIONAL COSMIC RAY CONFERENCE, RIO DE JANEIRO 2013
THE ASTROPARTICLE PHYSICS CONFERENCE

ICRC 2013

# Study of the time-dependence of the cosmic-ray anisotropy with AMANDA and IceCube

THE ICECUBE COLLABORATION[1],

[1] *See special section in these proceedings*

*santander@icecube.wisc.edu*

**Abstract:** The IceCube neutrino observatory and its predecessor, the AMANDA neutrino telescope, search for sources of astrophysical neutrinos against a high background of down-going muons originating from cosmic ray interactions in the atmosphere. The arrival direction of cosmic-ray muons is correlated with the direction of the original primary particle to within a degree for primary energies above several TeV. The large muon sample collected by both detectors provides us with a unique opportunity to study the arrival direction anisotropy of TeV cosmic rays in the southern sky over a time period of more than 12 years. A variation in the observed structure of the TeV anisotropy with time could provide hints about its origin. We present a search for time variability of the anisotropy observed by AMANDA between 2000 and 2006, and by IceCube between 2007 and 2012.

**Corresponding authors:** P. Desiati[1], M. Gurtner[2], K.-H. Kampert[2], T. Karg[2,a], M. Santander[1], S. Westerhoff[1]
[1] Wisconsin IceCube Particle Astrophysics Center, University of Wisconsin, Madison, WI 53706, U.S.A.
[2] Dept. of Physics, University of Wuppertal, D-42119 Wuppertal, Germany
[a] now at DESY, D-15735 Zeuthen, Germany

**Keywords:** Cosmic rays, Anisotropy, AMANDA, IceCube.

## 1 Introduction

Cosmic rays (CRs) in our galaxy are believed to originate in supernova remnants (SNRs) that can potentially accelerate charged particles up to PeV energies. The trajectories of these charged particles are affected by the presence of the magnetic field that permeates the galaxy. Cosmic rays propagating through the interstellar medium would scatter off of turbulences in the galactic magnetic field, which isotropizes their directions of arrival at Earth. This diffusion process creates gradients in the density of cosmic rays in the solar vicinity, which in turn should produce an anisotropy with a characteristic dipolar shape and a small amplitude of per-mille strength or lower (see [1] and references therein).

A number of experiments in the northern hemisphere have observed anisotropy at TeV energies (see [2] and others). The observed anisotropic structure in the sky shows two major features: an almost dipolar large angular scale component with a relative amplitude of $\sim 10^{-3}$ and several localized excess regions with typical sizes between $10^{\circ}$ and $30^{\circ}$ and relative amplitudes of $\sim 10^{-4}$. A similar structure has been observed in the southern sky using data from the IceCube detector [3, 4] at energies of about 20 TeV.

While it is possible that the large scale anisotropy is due to cosmic ray diffusion from nearby sources, its shape could be affected by the interaction of these cosmic rays with the heliosphere. It is known that cosmic rays with energies below 10 GeV are modulated by solar activity, but this influence should be less significant at higher energies. At primary energies of several TeV, the gyroradius of a proton in the $\mu$G-strength field of our galaxy is about $10^{-3}$ pc, which corresponds to scales of $\mathcal{O}(10^2)$ AU, similar to the size of the heliosphere. It has been argued [5] that given the similarity in these scales, it is possible that some of the observed structure in the anisotropy is due to scattering of cosmic rays in the heliosphere. Possible evidence for such a heliospheric influence on the anisotropy would be the observation of a variation in the anisotropy shape with the 11-year solar cycle. On much longer times scales (over thousands of years or more) a variation in the orientation and amplitude of the anisotropy is also expected due to changes in the cosmic-ray flux due to nearby sources [6].

Studies of the stability of the TeV anisotropy as a function of time have been performed by the Tibet [7], and Milagro [8] collaborations. While Tibet observes no significant variation in the anisotropy for the time period 11/1999 to 12/2008, Milagro reports a steady increase in the amplitude of the deficit region over a similar period of seven years (from 07/2000 to 07/2007). These stability studies can be extended to the southern hemisphere by analyzing the combined cosmic ray data set collected by the AMANDA and IceCube neutrino telescopes over the course of 12 years (from 2000 through 2011). Both detectors observe muons that originate in cosmic ray showers at very high rates, which has allowed us to collect multi-billion event data sets of cosmic ray muons with an angular resolution of a few degrees. The stable data taking conditions and the good angular resolution of both detectors make this study possible. The results of this search are presented in this work.

## 2 Detectors

### 2.1 AMANDA

AMANDA (Antarctic Muon And Neutrino Detector Array) [9] is the predecessor to the IceCube neutrino telescope. It consists of a three-dimensional array of 655 optical modules deployed over a volume of $3 \times 10^{-3}$ km$^3$ at depths between 1500 m and 2000 m in the Antarctic ice sheet at the geographic South Pole. Optical modules are connected to 19 vertical cables, or "strings", that provide mechanical support, electrical power, and a data connection to the

surface. The final configuration of the detector, AMANDA-II, operated from 2000 to 2006. AMANDA is located at a similar depth below the ice surface as IceCube, making it sensitive to TeV muons from cosmic-ray air showers.

The median energy of the cosmic-ray primary particles that produce muons detected in AMANDA is about 10 TeV [11]. Cosmic-ray muons are considered background for most neutrino searches, so only minimal information is stored for these events. In this work, we use this minimal data to search for large-scale anisotropies in the arrival directions of cosmic rays.

### 2.2 IceCube

The IceCube neutrino telescope [10] is based on the same design principle as AMANDA. In IceCube, a total of 5160 Digital Optical Modules (DOMs), attached to 86 strings, are deployed over a volume of about 1 km$^3$ at depths between 1450 m and 2450 m below the ice surface.

Similarly to the AMANDA case, only limited information is stored for cosmic-ray muons events. The median energy of this limited cosmic ray sample is determined from simulations to correspond to about 20 TeV.

## 3 Data selection

### 3.1 AMANDA

For this analysis, we use AMANDA events that satisfy the M24 trigger condition. This trigger requires a light signal in $\geq 24$ optical modules during a time window of 2.1 $\mu$s. For downward going muons from cosmic ray air showers, this corresponds to an energy threshold of a few hundred GeV, depending on the zenith angle. The data rate of the M24 trigger is approximately 100 Hz and follows seasonal variations in the atmospheric profile. The `DirectWalk` reconstruction algorithm [12], which has an angular resolution of about 4.8° [13], is applied online to all triggered events,. After reconstruction quality cuts, the data rate is reduced to approximately 60 Hz.

Maintenance, calibration procedures, and interferences from other experiments at South Pole can induce instabilities in the AMANDA data rate. To ensure that only data acquired under stable conditions are analyzed we exclude periods of unusually high or low rates. The data are divided in 5 minute long time slices and the event rate in each time slice is compared to the average event rate of the past 12 hours. Time slices in which the event rate deviates by more than 50% from the average rate are discarded.

### 3.2 IceCube

The main event trigger in IceCube is a simple multiplicity trigger called SMT8 that requires coincident hits in eight DOMs within 5 $\mu$s. For each trigger, all hits detected in coincidence by nearby DOMs within a $\pm 10\mu$s window are recorded and overlapping windows are merged. The SMT8 trigger rate shows a seasonal variation of $\pm 10\%$ over the course of a year, due to the change of atmospheric conditions that affect the muon production in air showers. The average trigger rate has increased over the years with the deployment of more strings in the ice, and is about 2700 Hz for the final 86-string configuration.

A first guess of the event direction is obtained by performing a linear-track fit to the DOM hits using an analytical $\chi^2$ minimization procedure. The result of the linear fit is used as a seed to a more complex likelihood-based reconstruction that takes into account some aspects of the light generation and propagation in the ice. A single-iteration of this likelihood fit (with an angular resolution of about 3°) is run online at the South Pole and the corresponding information is later transmitted over satellite.

Similarly to AMANDA, only periods where the detector data rate was stable are taken into account.

## 4 Analysis method and results

The search for anisotropy is conducted by searching for deviations of the sky map of reconstructed cosmic ray arrival directions in equatorial coordinates from a reference isotropic sky map obtained from data using the time-scrambling method described in [14]. The time scrambling period used in the analysis is 24 hours, which makes it sensitive to all angular scales in the celestial sphere. During the time scrambling procedure, events were resampled 20 times to reduce statistical fluctuations in the reference sky map.

The sky maps were constructed using the HEALPix[1] library [15] that provides an equal area pixelization of the sphere. The chosen HEALPix resolution divides the sphere into 49152 pixels, with an average distance between pixel centers of approximately 1°.

Using the reference and data maps, a relative intensity map can be calculated using the expression $\delta I_i = (N_i - \langle N \rangle_i)/\langle N \rangle_i$, where $N_i$ and $\langle N \rangle_i$ are, respectively, the number of observed events and the number of reference events for the isotropic expectation in the $i^{\text{th}}$ pixel obtained with the time scrambling technique.

Maps are subjected to a smoothing procedure to increase the sensitivity of the anisotropy search to structures larger than the map pixel size. The smoothing process creates a map of correlated pixels where the number of events in each pixel corresponds to the integrated number of events in a circular region around that pixel. The radius of the circular region (i.e. the smoothing radius) defines the angular scale of the structure for which the sensitivity of the smoothing procedure is optimized. For the maps shown in Fig. 1, a smoothing radius of 20° was chosen.

As can be seen in Fig. 1, the anisotropy maps show significant large-scale structure of per-mille amplitude in the southern sky as already reported by IceCube [3]. At first glance, the anisotropy shape appears to be stable across the twelve periods of approximately one year each considered in this work.

In order to obtain a quantitative result, we compared the observed anisotropy profile from each period defined according to Table 1 to the global twelve-year average. For this exercise, one-dimensional projections of the anisotropy maps were obtained by binning the right ascension coordinate $\alpha$ in 15 statistically-independent intervals. The relative intensity $\delta I(\alpha)$ in the $j^{\text{th}}$ right-ascension bin is calculated from the number of events in the data and reference maps contained in the declination range $-85° < \delta < -35°$.

The agreement between each yearly profile $\delta I_y$ and the global average $\langle \delta I \rangle$ is estimated by a $\chi^2$-test using the following expression:

$$\chi^2_y = \sum_{j=1}^{j=15} \frac{(\delta I_y(\alpha_j) - \langle \delta I(\alpha_j) \rangle)^2}{\sigma^2_{\delta I} + \sigma^2_{\langle \delta I \rangle}} , \qquad (1)$$

1. http://healpix.jpl.nasa.gov

| Period | Detector | Start | End | Live-time (days) | No. of events ($\times 10^9$) | $\chi^2$/dof | p-value |
|---|---|---|---|---|---|---|---|
| 1 | AM-II | 02/13/2000 | 11/02/2000 | 213.4 | 1.4 | 11.3/15 | 0.73 |
| 2 | AM-II | 02/11/2001 | 10/19/2001 | 235.3 | 2.3 | 16.6/15 | 0.34 |
| 3 | AM-II | 01/01/2002 | 08/02/2002 | 169.2 | 2.4 | 26.0/15 | 0.04 |
| 4 | AM-II | 02/09/2003 | 12/17/2003 | 236.0 | 2.2 | 19.3/15 | 0.20 |
| 5 | AM-II | 01/05/2004 | 11/02/2004 | 225.8 | 2.5 | 14.3/15 | 0.50 |
| 6 | AM-II | 12/30/2004 | 12/23/2005 | 242.9 | 2.6 | 21.0/15 | 0.14 |
| 7 | AM-II | 01/01/2006 | 09/13/2006 | 213.1 | 2.4 | 24.4/15 | 0.06 |
| 8 | IC22 | 06/01/2007 | 03/30/2008 | 269.4 | 5.3 | 45.2/15 | $7 \times 10^{-5}$ |
| 9 | IC40 | 04/18/2008 | 04/30/2009 | 335.6 | 18.9 | 12.8/15 | 0.62 |
| 10 | IC59 | 05/20/2009 | 05/30/2010 | 335.0 | 33.8 | 11.1/15 | 0.75 |
| 11 | IC79 | 05/31/2010 | 05/12/2011 | 299.7 | 39.1 | 6.5/15 | 0.97 |
| 12 | IC86 | 05/13/2011 | 05/14/2012 | 332.9 | 52.9 | 8.9/15 | 0.88 |

**Table 1**: Definition of each time period used in this analysis. AMANDA data sets are indicated as "AM-II", while IceCube data sets are marked as "IC" followed by the number of active detector strings during that time period. The number of live-days and recorded events is shown. Each time period is compared to the global twelve-year average using a $\chi^2$-test. The $\chi^2$ and the associated p-value for each period is also listed.

where the statistical uncertainties in each bin are calculated according to the expression:

$$\sigma_{\delta I} = \frac{N_j}{\langle N \rangle_j} \sqrt{\frac{1}{N_j} + \frac{1}{s\langle N \rangle_j}} \,. \quad (2)$$

Here, $s = 20$ is the number of resamples that was used in the calculation of the reference map. The combined uncertainty in the difference is obtained by adding the individual uncertainties in $\delta I_y$ and $\langle \delta I \rangle$ in quadrature. The global uncertainty in each bin is dominated by the uncertainty in each yearly period due to the relatively lower level of statistics. Only statistical uncertainties have been considered so far. A future analysis will account for systematic effects that may be caused by the incomplete time coverage of each period which could lead to distortions in the right ascension profile (for instance, due to interference of the solar dipole anisotropy with the anisotropy in equatorial coordinates [4]).

A p-value was calculated for each reduced $\chi^2$ value. A list of p-values is given in Table 1. With the exception of Period 8, all p-values show a good agreement between individual periods and the global average, given the statistical uncertainties of each set. The large p-values for periods 11 and 12 are expected since the large relative size of both data sets makes them dominate the global average profile. Period 8 corresponds to the start of regular operation of IceCube, where the detector operated with 22 active strings (about one quarter of the final size of the detector). Due to gaps in the data taking process and fluctuations in the muon rate, it is possible that the discrepancy is related to detector effects. The impact of these effects is currently under investigation.

A preliminary study of the amplitudes and phases of a first and second harmonic fit to the relative intensity profiles shows no significant modulation over time.

## 5 Conclusions

A study of the stability of the TeV cosmic ray anisotropy over a period of twelve years is presented using data recorded with the AMANDA and IceCube detectors. No significant time variation in the observed anisotropy is found with the exception of the period corresponding to the 22-string configuration of IceCube.

Since IC22 was the first year of regular operation of IceCube, instabilities in the detector configuration were common, which may have led to distortions in the observed anisotropy. Further stability studies are required to estimate the impact of these detector effects.

## References

[1] P. Blasi and E. Amato, J. Cosmol. Astropart. Phys. 1/011 (2012) 11 doi:10.1088/1475-7516/2012/01/011.
[2] M. Amenomori et al., Science 314 (2006) 439 doi:10.1126/science.1131702.
[3] R. Abbasi et al., Astrophys. J. 718 (2010) L194 doi:10.1088/2041-8205/718/2/L194.
[4] R. Abbasi et al., Astrophys. J. 740 (2011) L16 doi:10.1088/0004-637X/740/1/16.
[5] P. Desiati and A. Lazarian, Astrophys. J. 762 (2013) 44 doi:10.1088/0004-637X/762/1/44.
[6] M. Pohl and D. Eichler, Astrophys. J. 766 (2013) 4 doi:10.1088/0004-637X/766/1/4.
[7] M. Amenomori et al., Astrophys. J. 711 (2010) 119 doi:10.1088/0004-637X/711/1/119.
[8] A. A. Abdo et al., Astrophys. J. 698 (2009) 2121 doi:10.1088/0004-637X/698/2/2121.
[9] E. Andres et al., Astropart. Phys. 13 (2000) 1 doi:10.1016/S0927-6505(99)00092-4.
[10] A. Achterberg et al., Astropart. Phys. 26 (2006) 155 doi:10.1016/j.astropartphys.2006.06.007.
[11] D. A. Chirkin, PhD thesis (2003) University of California, Berkeley.
[12] J. Ahrens et al., Nucl. Instrum. Meth. A524 (2004) 169 doi:10.1016/j.nima.2004.01.065.
[13] P. Steffen, Tech. Report AMANDA-IR/20010801, DESY, 2001.
[14] D. E. Alexandreas et al., Nucl. Instr. Meth. A328 (1993) 570 doi:10.1016/0168-9002(93)90677-A.
[15] K. M. Gorski et al., Astrophys. J. 622 (2005) 759 doi:10.1086/427976.

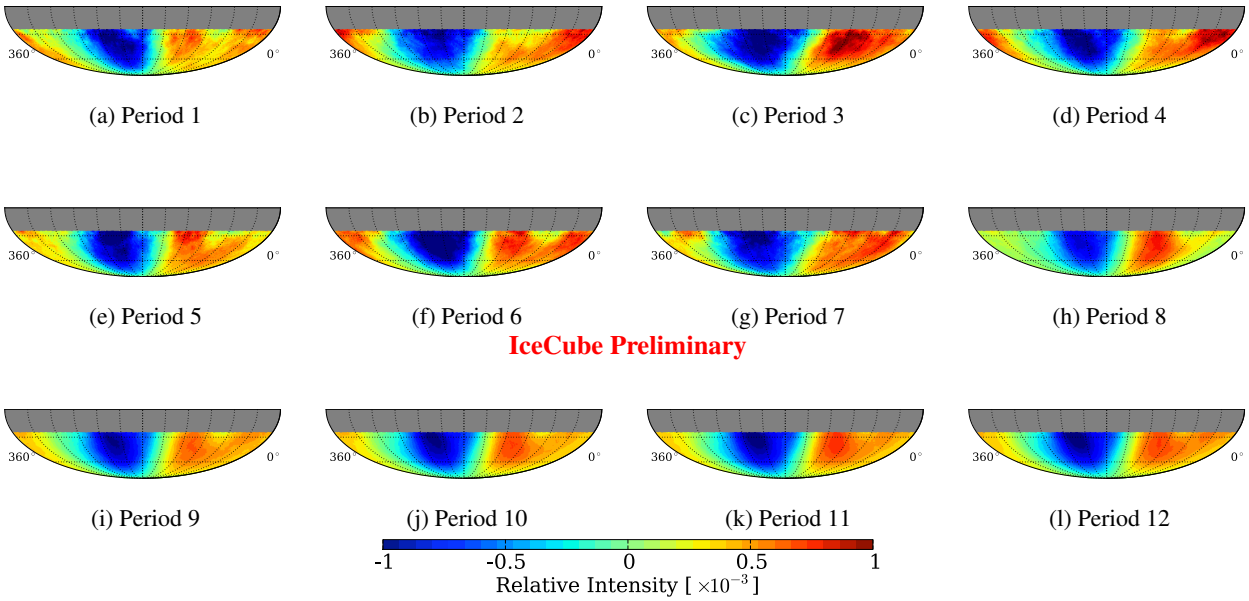


**Figure 1**: Two-dimensional relative intensity maps in equatorial coordinates of the cosmic ray anisotropy for the 12 time periods covering the years from 2000 to 2012 (see Table 1). All maps have been smoothed using a circular window with a 20° angular radius.

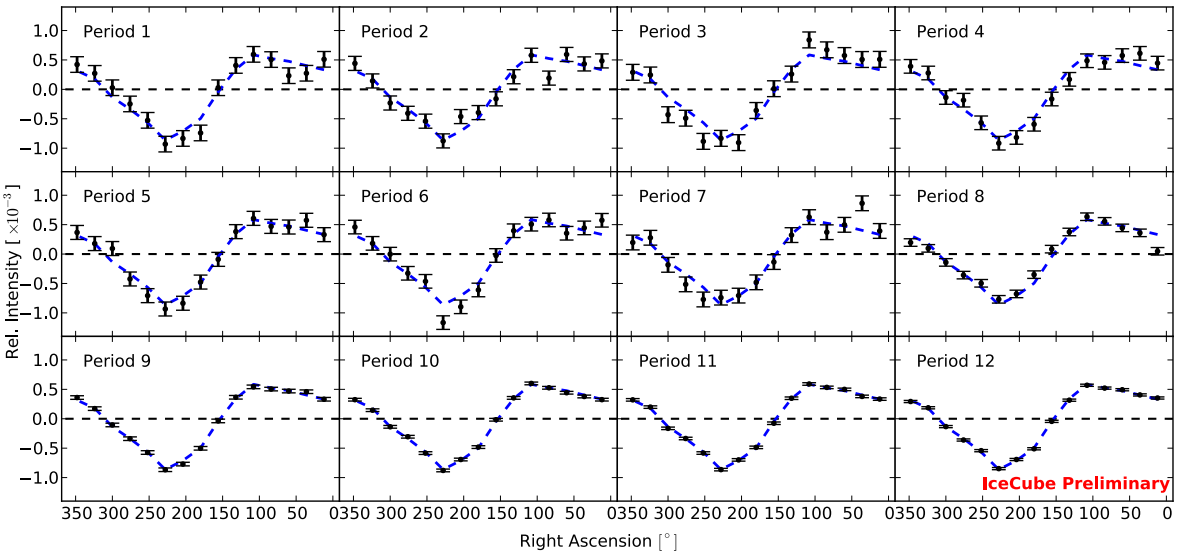


**Figure 2**: One-dimensional projections of relative intensity as a function of right ascension for the 12 time periods considered in this work. As a reference, the average profile for the entire data set is shown as a dashed blue line. The uncertainties shown are only statistical.

33RD INTERNATIONAL COSMIC RAY CONFERENCE, RIO DE JANEIRO 2013
THE ASTROPARTICLE PHYSICS CONFERENCE

# Low Energy Air Showers With IceTop

THE ICECUBE COLLABORATION[1]
[1]*See special section in these proceedings*
*abd.hajismail@ugent.be*

**Abstract:** IceTop, the surface component of the IceCube detector, was completed in 2011 with 81 stations covering an area of 1 km$^2$. Most IceTop stations are placed with a spacing of 125 m. Three of them, located in the center of the array, were deployed with smaller separations forming with five other neighboring stations a sub-array called the InFill array. Standard IceTop analyses use events which trigger at least five stations leading to an energy threshold of about a few PeVs. The goal of this analysis is to study the properties of small showers that hit the InFill array and do not have more than five stations, This should allow us to measure the energy spectrum in the overlap region with direct cosmic ray primary particle measurements.

**Corresponding authors:** Abd al karim Haj Ismail[1]
[1]*Department of Physics and Astronomy, University of Gent, B-9000 Gent, Belgium*

**Keywords:** IceTop, InFill Array, Low Energy Showers

## 1 Introduction

The IceTop cosmic ray air shower array is currently operating with a complete configuration as a part of the IceCube Neutrino Observatory at the geographic South Pole. IceTop consists of 81 stations covering an area of about 1 km$^2$ at a height of 2832 m above sea level, which is equivalent to an atmospheric depth of about 680 g/cm$^2$. Each station consists of two ice-filled tanks separated by 10 m, each equipped with two Digital Optical Modules (DOMs) as optical sensors [1].

IceTop measures the Cherenkov light emitted by charged particles inside the ice tanks. When a signal is recorded in a DOM, a local coincidence signal is required from one DOM in the neighboring tank in the same station within 1 $\mu$s to start the data recording.

IceTop measured the cosmic ray energy spectrum at energies between 1 PeV and 100 PeV [2, 3] and between 2 PeV and 1 EeV [4, 5]. These measurements were restricted to air showers that trigger at least 5 stations, which is the minimum number of stations required to achieve a stable shower reconstruction in IceTop. This restriction results in an energy threshold of a few PeVs. To decrease the energy threshold of the detector to around 100 TeV, three extra stations were deployed at the center of the detector forming, with five other stations in the center, a denser sub-array called the InFill array (Fig. 1).

This analysis investigates the basic reconstructed shower observables of events that trigger three stations in the InFill array and have a maximun of five stations in IceTop, and explores the possibility to measure the energy spectrum between 100 TeV and a few PeVs. In this energy range, the measurement would overlap with direct cosmic ray primary particle measurements (e.g., ATIC [6]).

## 2 Data, Simulations and Event Selection

Monte Carlo simulations for proton and iron primaries were produced using CORSIKA v73500 [7], according to an E$^{-1}$ spectrum. SIBYLL 2.1 [8] was used as a hadronic interaction model for energies greater than 80 GeV and FLUKA [9] for lower energies. Showers were generated over all azimuths and with zenith angles between 0° and 65°. Since the simulation is computationally intensive, each generated shower was re-sampled 100 times over a circular area around the center of IceTop, with a radius of 600 m, 800 m, 1100 m and 1700 m and a primary energy range of $\log_{10}(E/\mathrm{GeV})$: 4-5, 5-6, 6-7 and 7-8, respectively.

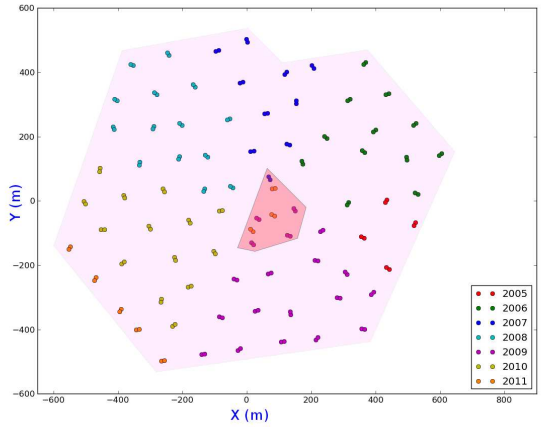


**Figure 1**: The completed IceTop array. The center area represents the eight stations of the InFill array.

Three InFill stations are required to fulfill the InFill trigger. Events are selected if the InFill trigger is passed and we have a maximum of five IceTop stations per event. Three of the InFill stations are required to be adjacent to remove showers that pass the InFill trigger and have a large distance between stations. Extra cuts based on the quality of shower reconstruction are applied to ensure the selection of well reconstructed events. We studied events in two zenith angle bands of equal solid angle [1.0>cos($\theta$)>0.9]

and [0.9>cos($\theta$)>0.8] to include the zenith dependence in the analysis.

Data from June 2011 is used for this analysis. In total, 539,884 events were left for [1.0>cos($\theta$)>0.9] and 322,964 events for [0.9>cos($\theta$)>0.8] in the data sample after all cuts.

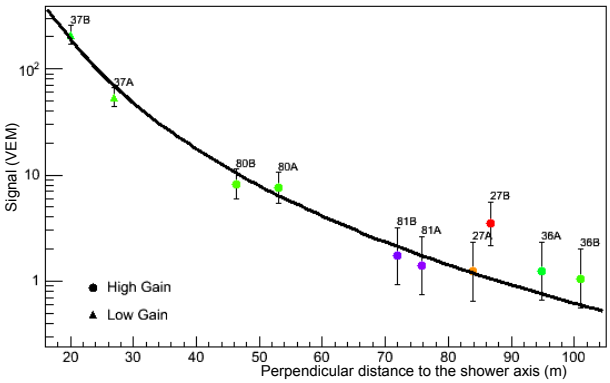


**Figure 2**: An example of a lateral fit distribution. The distance to the reconstructed shower axis is shown on the horizontal axis. Different colors represent the arrival time of the signal with red corresponding to early pulses. Error bars are charge fluctuations.

## 3 Shower Reconstruction

The shower size, which is defined as the strength of the signal $S_{\rm ref}$ (in a unit of vertical equivalent muon VEM [1]) at a given distance $R_{\rm ref}$ to the shower axis, is one of the main parameters that characterize the air shower. The shower direction is determined from the arrival times of the signals recorded by the DOMs, and the particle density and core position are determined from the lateral distribution of measured charges [2].

A first guess for the shower core is obtained by calculating the average of tank positions weighted by the square root of the charges, while an initial estimate for the shower direction is obtained by fitting a plane perpendicular to the shower axis to the measured arrival time of signal. These two first guesses are used as an input for a maximum likelihood fitting procedure [1] to fit a lateral distribution function (LDF) to the recorded signals,

$$S(\mathrm{r}) = S_{\rm ref}\left(\frac{\mathrm{r}}{R_{\rm ref}}\right)^{-\beta-0.303\log_{10}(\frac{\mathrm{r}}{R_{\rm ref}})}, \qquad (1)$$

where $S_{\rm ref}$ is the expectation value of the signal at a reference distance $R_{\rm ref}$ from the shower axis. $\beta$ is the slope of the lateral distribution function at $R_{\rm ref}$ . The free parameters of this functions are $S_{\rm ref}$ and $\beta$. Figure 2 shows the lateral distribution function, with data from one event.

The maximum likelihood accounts also for stations that did not trigger and saturated signals close to the shower core. The likelihood, therefore, has four terms,

$$L = L_{\rm t} + L_{\rm s} + L_0 + L_{\rm sat}, \qquad (2)$$

where $L_{\rm t}$ describes the timing likelihood for the signal arrival time, $L_{\rm s}$ is the signal size likelihood, $L_0$ accounts for stations that do not trigger, $L_{\rm sat}$ is a saturation likelihood.

The standard IceTop reconstruction fails for all events that trigger less than five stations. In this analysis, we use small showers with three, four and five stations, where we fix the shower direction to the value from the first guess, to decrease the number of free parameters, and perform the fitting procedure in one step.

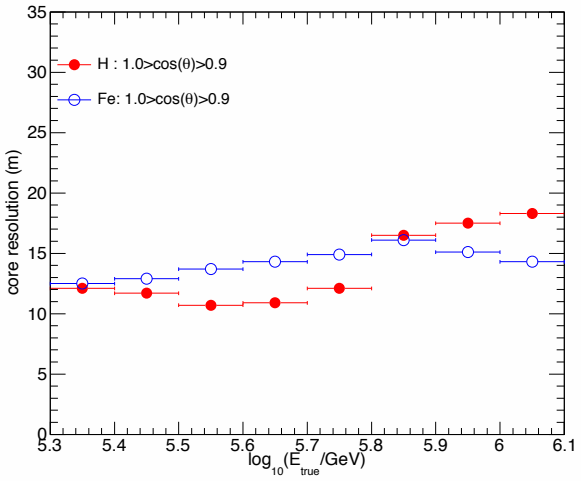


(a)

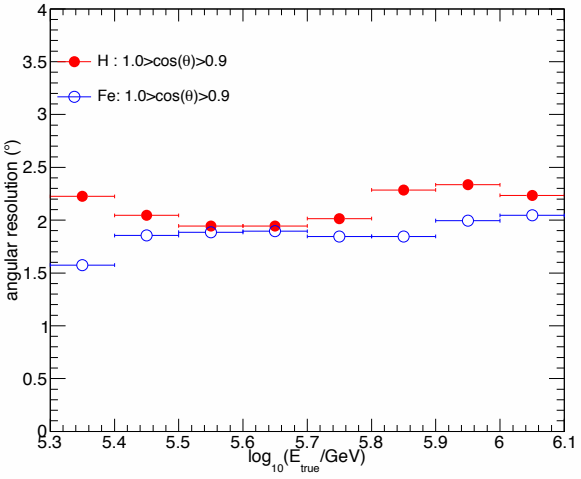


(b)

**Figure 3**: The core and angular resolution for showers with a zenith angle band 1.0>cos($\theta$)>0.9. Upper plot: the core resolution. Lower plot: the angular resolution

To check the quality of the reconstruction, the core and angular resolution are plotted in Figure 3, for proton and iron showers, in an energy range between 200 TeV and 1 PeV, and in the vertical zenith angle band [1.0>cos($\theta$)>0.9]. The core resolution is defined as 68% of the integral distribution of the distance between the reconstructed track and the true track on the surface. The core resolution for reconstructed showers is between 10 m and 18 m (Fig. 3a). The angular resolution is defined as 68% of the integral of the angle between the reconstructed track direction and the true track direction. The angular

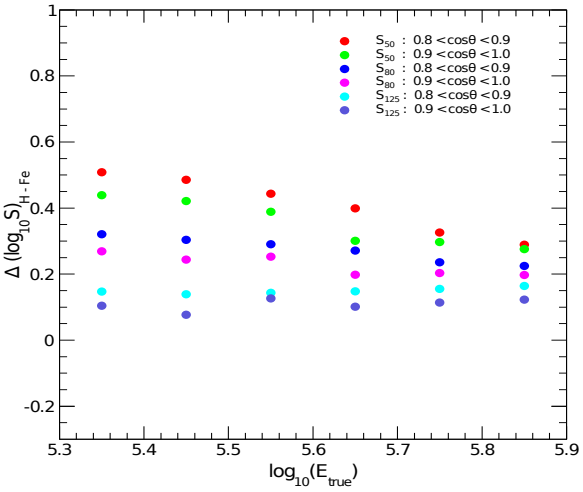


**Figure 4**: Difference between the shower size ($S_{50}$, $S_{80}$ and $S_{125}$) of proton and iron induced showers for reference distances ($R_{50}$, $R_{80}$ and $R_{125}$ m) as a function of the primary energy.

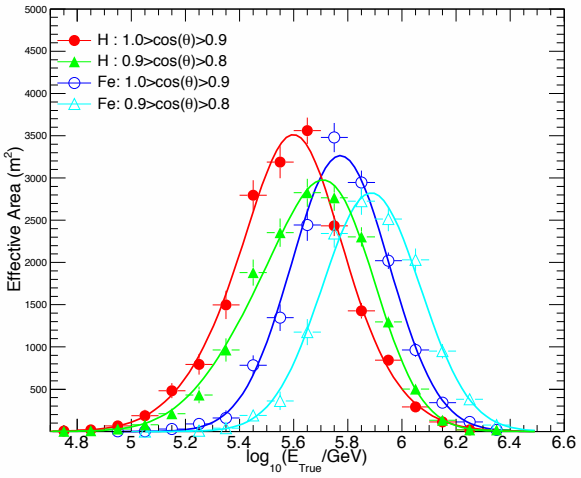


**Figure 5**: The effective area for proton and iron induced showers triggering five stations in two zenith bands. Gaussian fits were added to guide the eye.

resolution for proton and iron is around 2° (Fig. 3b).

In Figure 4, we study the shower size dependence on primary mass and zenith angle at different distances from the shower axis as a function of true energy. There is no indication for a composition independent shower size at any of the studied distances from the shower axis over this energy range. This is due to the higher particle density for proton showers than for iron showers. This difference decreases at higher energies and for more vertical zenith angles.

The distance of 80 m was chosen as a reference distance $R_{\text{ref}}$ for this analysis because most of our signals are around 80 m from the shower axis.

## 4 Effective Area and Reconstructed Energy

The effective area describes the efficiency of the detector to detect air showers. It is calculated from Monte Carlo simulations and is defined as,

$$A_{\text{eff}} = A_{\text{gen}} \frac{N_{\text{cut}}}{N_{\text{gen}}}. \qquad (3)$$

$A_{\text{gen}}$ is the re-sampling geometric area used in simulations, $N_{\text{cut}}$ is the total number of events we keep in the final sample after all cuts and $N_{\text{gen}}$ is the total number of generated events in simulations.

The effective area for proton and iron showers in the two zenith bands is shown in Figure 5. It reaches a maximum at energy of 400 TeV for proton and 630 TeV for iron in the vertical zenith angle band. Due to the restriction to showers that do not trigger more than five stations, $A_{\text{eff}}$ decreases rapidly towards higher energies. Iron starts interacting higher in the atmosphere and showers will be at different stage of development at the detector level. The probability for showers to reach the detector level and trigger at low energy is smaller for iron than for proton showers. Inclined showers travel for a larger distance than vertical showers in the atmosphere. Therefore, a clear composition and zenith dependence can be seen in the effective area.

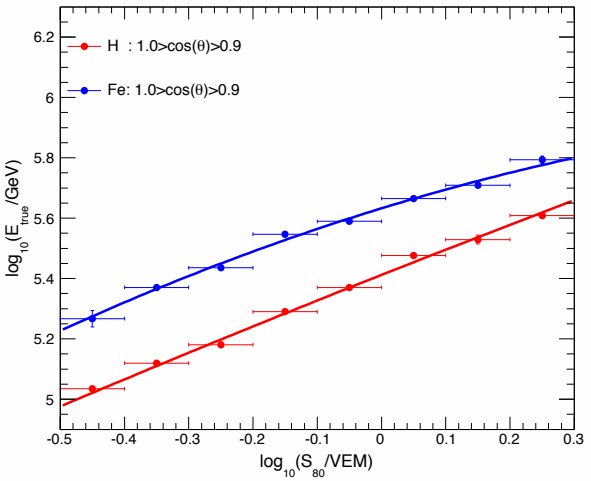


**Figure 6**: $\log_{10}(E_{\text{true}}/\text{GeV})$ vs $\log_{10}(S_{80}/\text{VEM})$ for proton and iron induced showers in the vertical zenith angle band.

The shower size is closely related to the primary energy and can be used as an energy estimator. Simulated proton and iron showers were divided into intervals of width 0.1 in $\log_{10}(S_{80})$. For each interval, the distribution of the logarithm of the simulated primary energies $\log_{10}(E_{\text{true}})$ was fitted with a Gaussian. The mean of the Gaussian is taken as an energy estimate for showers in the respective $\log_{10}(S_{80})$ interval. Figure 6 shows the energy estimate as a function of $\log_{10}(S_{80})$ for simulated proton and iron showers in the vertical zenith angle band. The relationship between $\log_{10}(S_{80})$ and $\log_{10}(E_{\text{true}})$ is fitted with a parabola:

$$\log_{10} E = p_0 + p_1 \log_{10} S_{80} + p_2 (\log_{10} S_{80})^2. \qquad (4)$$

The parameters $p_0$, $p_1$, $p_2$ are composition and zenith dependent.

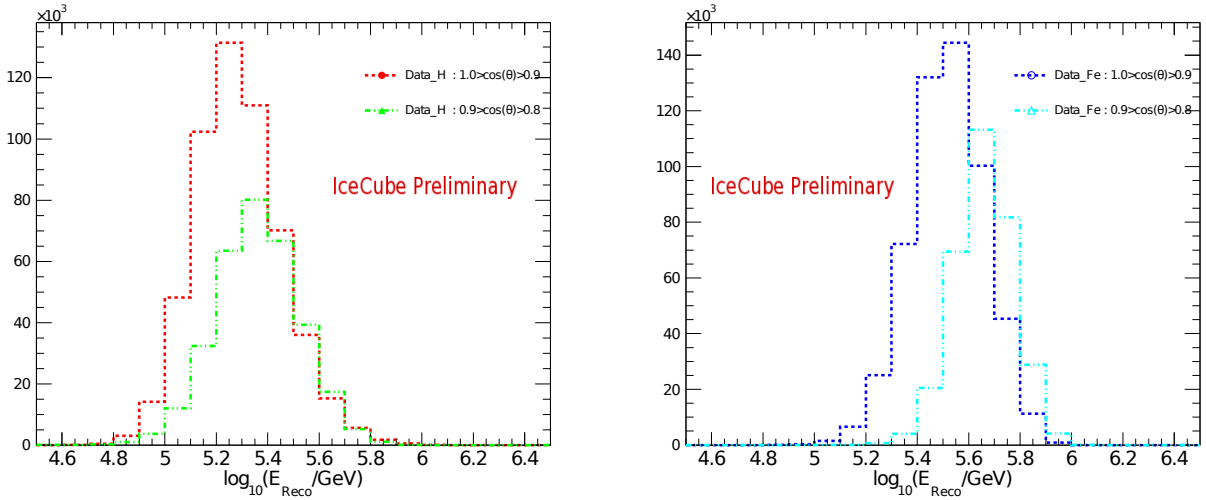


**Figure 7**: The reconstructed energy distributions for showers triggering a maximum of 5 stations obtained from experimental data with proton assumption (a) and with iron assumption (b). Different colors represent different zenith angle bands.

An energy distribution is obtained when applying the proton and iron energy conversion to experimental data (Fig. 7). The data is reconstructed with proton assumption (Fig. 7a), and with iron assumption (Fig. 7b). The reconstructed energy depends, as expected, on primary mass and zenith angle.

## 5 Conclusion and Outlook

In this paper, the performance of reconstruction for low energy showers is investigated using simulations. The core and the angular resolution have been calculated for proton and iron induced showers and in two zenith angle bands.

Including the small shower events to the standard IceTop analysis would lead to the possibility to extend the IceTop energy threshold to around 100 TeV where it overlaps with direct measurements. A clear composition and zenith dependence on primary energy and primary mass has to be taken into account for further analysis.

In order to measure the energy spectrum, some other issues have to be included in this analysis. Most importantly, the effect of snow on the shower signal is expected to be large at this energy range [10].

We are planning to use more IceTop data to provide enough statistics for a more accurate study of the energy spectrum at low energy. Including events with larger number of stations is needed to have an overlap with the energy spectrum measured with current IceTop analysis.

## References

[1] R. Abbasi et al., NIM. A, 700 (2013) 188 doi:10.1016/j.nima.2012.10.067.
[2] R. Abbasi et al., Astropart. Phys. 44 (2013) 40 doi:10.1016/j.astropartphys.2013.01.016.
[3] R. Abbasi et al., Astropart. Phys. 42 (2013) 15 doi:10.1016/j.astropartphys.2012.11.003.
[4] IceCube Collaboration., paper 0246, these Proceedings.
[5] IceCube Collaboration., paper 0861, these Proceedings.
[6] A.D. Panov et al., Bulletin of the Russian Academy of Sciences, 73 (2009) 564 doi:10.3103/S1062873809050098.
[7] D. Heck et al., report FZKA 6019 (1998).
[8] E. Ahn, R. Engel, T. Gaisser, P. Lipari, and T. Stanev, Phys. Rev. D80 (2009) 094003 doi:10.1103/PhysRevD.80.094003.
[9] G. Battistoni et al., AIP Conference proceedings 896 (2007) 31.
[10] IceCube Collaboration., paper 1106, these Proceedings.

33RD INTERNATIONAL COSMIC RAY CONFERENCE, RIO DE JANEIRO 2013
THE ASTROPARTICLE PHYSICS CONFERENCE

ICRC 2013

# Seasonal variation of the muon multiplicity in cosmic rays at South Pole

THE ICECUBE COLLABORATION[1]

[1] *See special section in these proceedings*

*sam.deridder@ugent.be*

**Abstract:** The semi-annual alternation between polar day and polar night causes the South Pole atmosphere to undergo a large annual change. Seasonal changes of the atmosphere highly affect the properties of cosmic ray air showers. IceCube detects the high-energy muonic component of air showers with the 1 km$^3$ underground detector, whereas IceTop, the surface array, mainly measures the electromagnetic component. The influence due to the seasonal changes on the high-energy muon multiplicity, important for composition studies, is studied in simulation and data. To reduce this variation, a correction procedure based on the measured atmospheric temperature profile and the muon production longitudinal profile is proposed.

**Corresponding authors:** Sam De Ridder[1], Tom Feusels[1]
[1] *Dept. of Physics and Astronomy, University of Gent, B-9000 Gent, Belgium*

**Keywords:** IceCube, cosmic rays, seasonal modulation

## 1 Introduction

At South Pole, extreme seasonal variations of the atmosphere can be found, due to the tilt of the Earth's rotation axis relative to the ecliptic. During austral spring, the sun heats the atmosphere above the Antarctic ice sheet, while it cools down in fall. In the ozone layer, on average at altitudes between 15 and 35 km above sea level, an increase in the UV absorption causes even larger seasonal changes of the atmospheric temperature [1].

At these altitudes, the first interactions of cosmic rays happen and highly energetic mesons, mainly pions and kaons, are produced. The charged mesons decay to high-energy (HE) muons or interact in the atmosphere. The competition between interaction and decay depends on the density $\rho$ (interaction length $\lambda_{\text{int}} \sim \frac{1}{\rho}$) at the local pressure levels, thus on temperature [2]. Hence, as the cosmic ray air shower develops through the atmosphere, the production of the HE muons is highly affected by these atmospheric variations.

The underground detector of the IceCube Neutrino Observatory, which was completed in December 2010, consists of 86 strings spread over 1 km$^2$, with Digital Optical Modules (DOMs) located between 1450 and 2450 m below the surface [3]. On the surface above the underground detector, 81 detector stations constitute the surface detector, called IceTop [4]. Each station consists of two ice Cherenkov tanks, equipped with two DOMs each. IceTop mainly measures the electromagnetic component of the shower, while muons with an energy of at least 300 GeV penetrate the Antarctic ice down to IceCube. Using the information obtained from the muon bundles in combination with the data from IceTop, a coincident IceTop-IceCube analysis is able to measure both the cosmic ray composition and energy spectrum.

All relations between primary energy, mass and reconstructed observables are based on simulations with a single reference atmosphere, for both the coincident analysis that used the 40-string/40-station configuration (IT40-IC40) [5] and the IT73-IC79 coincident analysis [6]. The seasonal variations of the light yield that affect the IceCube measurements should be corrected with respect to this reference atmosphere. The variations of the upper atmosphere are small within each month, so one year of data taking is divided in 12 months. Therefore, only one month of data has been used in the IT40-IC40 analysis. When we want to use an entire year of data, it is crucial to account for these effects.

As the main observable for measuring the composition, the IT73-IC79 analysis uses the energy loss of the HE muon bundle $\left(\mathrm{d}E_\mu/\mathrm{d}x\right)_{\text{bundle}}$ (GeV/m) at a slant depth of 1500 m. Figure 1 shows the influence of the seasonal variations on $\log_{10}\left(\mathrm{d}E_\mu/\mathrm{d}x\right)_{\text{bundle}}$. A maximum variation of 10-15% relative to the proton-iron separation is present (Figure 7), which will affect the determination of the cosmic ray composition.

## 2 Method

In [1], it is shown that the variation in the IceCube muon trigger rate is proportional to the variation in effective temperature ($T_{\text{eff}}$). The effective temperature is defined such that the temperature profile ($T(X)$, where $X$ is the atmospheric depth) is weighted by the muon production height spectrum, created by a nucleon flux convoluted with the effective area for the IceCube trigger rate [2, 7].

The variation of the multiplicity of muons with energies above 300 GeV is highly dependent on the primary energy and composition. Therefore we define a new effective temperature $\tilde{T}_{\text{eff}}$ by weighting the temperature profile $T(X)$ by the muon longitudinal profile $\mathrm{d}N_\mu/(\mathrm{d}X\,\mathrm{d}E_\mu)$ which is a function of primary energy $E_0$ and composition $A$ :

$$\tilde{T}_{\text{eff}}(E_0,A) = \frac{\iint \frac{\mathrm{d}N_\mu}{\mathrm{d}X\,\mathrm{d}E_\mu}(E_0,A)T(X)\,\mathrm{d}X\,\mathrm{d}E_\mu}{\iint \frac{\mathrm{d}N_\mu}{\mathrm{d}X\,\mathrm{d}E_\mu}\,\mathrm{d}X\,\mathrm{d}E_\mu}\,. \quad (1)$$

To obtain the mean $T(X)$ for each month of the 2010-2011 data taking period (from June 1, 2010 until May 12, 2011), we averaged the daily temperature profiles of each

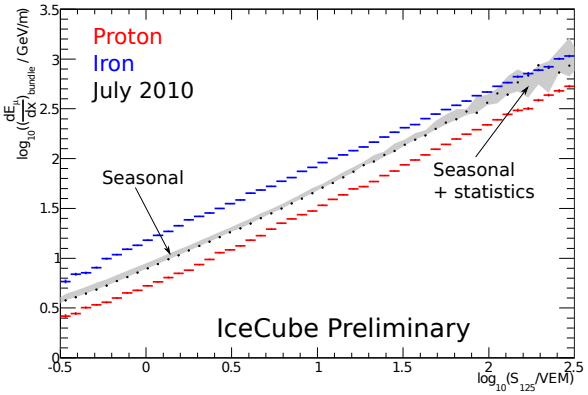


**Figure 1**: The mean $\log_{10}\left(\mathrm{d}E_\mu/\mathrm{d}x\right)_{\mathrm{bundle}}$ at a slant depth of 1500 m below the Antarctic surface, as a function of $\log_{10}(S_{125})$. $S_{125}$ is the IceTop parameter related to the cosmic ray air shower size, which is used to measure the primary energy of the shower [4]. The proton and iron data points are obtained from simulations, described in [6]. The black points show the mean $\log_{10}\left(\mathrm{d}E_\mu/\mathrm{d}x\right)_{\mathrm{bundle}}$ as a function of $\log_{10}(S_{125})$ obtained in July 2010, while the grey band shows the maximal variation during the year with respect to July 2010.

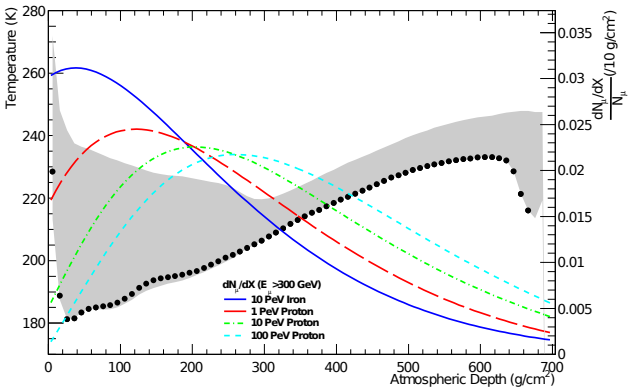


**Figure 2**: The grey band shows the maximal variation of the temperature profile (T(X)) for the average atmospheres of June 2010 until May 12, 2011. The reference month (July 2010) is shown as the black points. The 4 curves are fits to the normalized muon longitudinal profiles $\left(\frac{1}{N_\mu}\frac{\mathrm{d}N_\mu}{\mathrm{d}X}\right)$ for proton showers of 1, 10 and 100 PeV and 10 PeV iron showers, with a muon threshold of 300 GeV. From these curves the $\tilde{T}_{\mathrm{eff}}(A, E_0)$ for each month can be calculated.

month. Figure 2 shows the average temperature profile of July (black points) 2010 and its maximal variation (grey band). The atmosphere data used in this study are provided by balloon measurements from the Antarctic Meteorological Research Center (AMRC [9]) and are extended to larger altitudes with data obtained from the Atmospheric Infrared Sounder (AIRS), one of the six instruments on board of the NASA Aqua Research satellite [10].

Combining the average temperature profile and the muon production profile, $\tilde{T}_{\mathrm{eff}}(E_0, A)$ will be determined for each month in Section 3. In simulation, we investigate whether a linear relation between the variation in $\tilde{T}_{\mathrm{eff}}$ and the variation in muon multiplicity can be found. In Section 4, the relation between the variation in reconstructed muon bundle energy loss with the variation in $\tilde{T}_{\mathrm{eff}}$ will be examined in IT73-IC79 data. Based on that relation we will derive a scheme to correct our data with respect to simulation in Sections 5 and 6.

## 3 Simulation

The muon longitudinal profile $\mathrm{d}N_\mu/(\mathrm{d}X\,\mathrm{d}E_\mu)$ of a shower with energy $E_0$ and mass $A$ depends on the pion and kaon energy spectrum, created in the first interactions at high altitudes, and their decay and interaction probabilities while propagating through the atmosphere. Here we will extract the muon profiles from simulation with a muon energy threshold of 300 GeV, for eight different primary energies $(1, 2.5, 5, 10, 25, 50, 100, 300$ PeV), for proton and iron primaries. Using CORSIKA v6990 [11] with Sybill 2.1 [12] as hadronic interaction model above 80 GeV and Fluka [13] below, 500 vertical showers were generated for each energy, primary mass and each of the 12 months.

The muon longitudinal profiles for proton showers of different primary energies are shown in Figure 2. Due to the superposition model, where a shower induced by a primary particle with mass $A$ and energy $E_0$ can be seen as $A$ proton showers with average primary energy $E_0/A$, iron muon longitudinal profiles will peak at much smaller atmospheric depths than proton. Therefore the relation between $\tilde{T}_{\mathrm{eff}}$ and $\log_{10}(E_0/A)$ is linear in each month (Figure 3). Because in data there is a continuous range of primary energies, this linear relation was fitted and used later on.

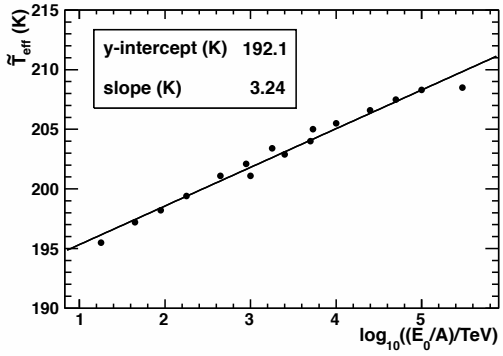


**Figure 3**: $\tilde{T}_{\mathrm{eff}}$ as a function of $\log_{10}(E_0/A)$ for July 2010.

$\tilde{T}_{\mathrm{eff}}$ for each month, primary energy and primary mass is obtained by multiplying the average temperature profile of this month with the muon longitudinal profile for that energy and mass, normalized (by the total multiplicity) per atmospheric depth bin and then summed over the whole atmospheric depth profile.

The simulations for the analysis done in [6, 8] are performed based on the July 1, 1997 South Pole atmosphere, so a correction of the data should be done with respect to this atmosphere. Simulation studies showed that $\Delta N_\mu(E_0, A) \approx 0$ between this atmosphere and the July 2010 atmosphere. Therefore, we will study the variation of the muon multiplicity and $\tilde{T}_{\mathrm{eff}}$, both with respect to July 2010

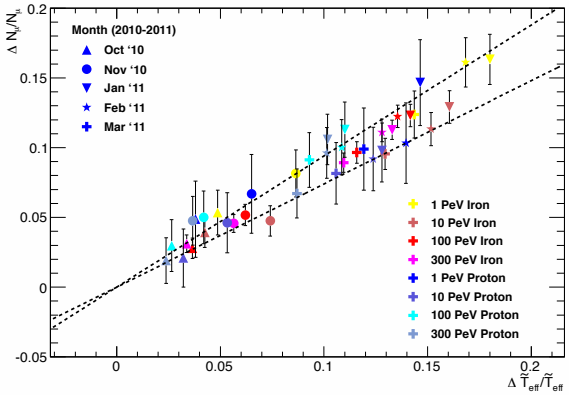


**Figure 4**: The variation in muon multiplicity with respect to the muon multiplicity in July 2010 as a function of the variation in effective temperature for 5 different real atmospheres, 4 primary energies and proton and iron primaries. The dashed lines are the $\tilde{\alpha}_{MC} = 0.74$ and 0.94 lines to show the variation in obtained temperature coefficients.

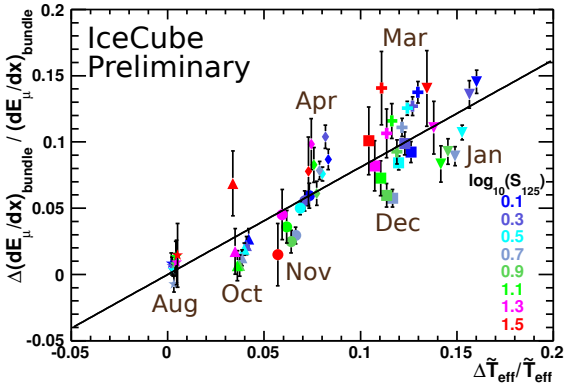


**Figure 5**: The (relative) difference in energy loss of the muon bundle at a slant depth of 1500 m, as a function of the difference in $\tilde{T}_{\text{eff}}$. This is shown for all months compared to the reference month July 2010. The different colors show the different $\log_{10}(S_{125}/\text{VEM})$ bins.

in simulation and determine the temperature coefficient $\tilde{\alpha}_{MC}$ :

$$\frac{\Delta N_\mu}{N_\mu} = \tilde{\alpha}_{\text{MC}} \frac{\Delta \tilde{T}_{\text{eff}}}{\tilde{T}_{\text{eff}}} \qquad (2)$$

$$\frac{N_{\mu,i} - N_{\mu,\text{July}}}{N_{\mu,\text{July}}} = \tilde{\alpha}_{\text{MC}} \frac{\tilde{T}_{\text{eff},i} - \tilde{T}_{\text{eff,July}}}{\tilde{T}_{\text{eff,July}}} .$$

In Figure 4, the expected linear correlation between the variation in muon multiplicity and effective temperature is shown. A linear fit through all points yields an average temperature coefficient $\tilde{\alpha}_{MC}$ of $0.84 \pm 0.10$. The error shows the spread of the points. In Section 5 a possible energy dependence of the temperature coefficient will be discussed.

## 4 Data

In IceCube data, we do not directly measure the number of muons in the shower, neither the primary energy or mass. Therefore IceTop and IceCube observables are used to perform a similar study. We use the energy loss of the muon bundle at a slant depth of 1500 m ($\log_{10}\left(\mathrm{d}E_\mu/\mathrm{d}x\right)_{\text{bundle}}$), which is linearly correlated to the number of muons in a shower, together with $S_{125}$, the main IceTop energy sensitive observable. In order to obtain $\tilde{T}_{\text{eff}}$, which is energy and mass dependent, we need to convert $S_{125}$ to $\tilde{T}_{\text{eff}}$. The conversion from $S_{125}$ to primary energy is done by using:

$$\log_{10}(E_0/\text{GeV}) = 6.018 + 0.938 \log_{10}(S_{125}/\text{VEM}) , \quad (3)$$

obtained in [8]. The mean $< \log A >$ obtained in the IT73-IC79 analysis [6] for July 2010 is about 1.9 in the energy region from 1 to 40 PeV. From simulation, the relation between $\tilde{T}_{\text{eff}}$ and $\log_{10}(E_0/A)$ was found (Figure 3). Hence, using a mean atomic mass assumption of $A = 7$ ($< \log A > \approx 1.9$) and the energy from Eqn. 3, one obtains $\tilde{T}_{\text{eff}}$.

Similar to the simulation study, one can now relate the difference in energy loss to the difference in $\tilde{T}_{\text{eff}}$:

$$\frac{\Delta \left(\frac{\mathrm{d}E_\mu}{\mathrm{d}x}\right)_{\text{bundle}}}{\left(\frac{\mathrm{d}E_\mu}{\mathrm{d}x}\right)_{\text{bundle}}} = \tilde{\alpha}_{\text{data}} \frac{\Delta \tilde{T}_{\text{eff}}}{\tilde{T}_{\text{eff}}} , \qquad (4)$$

for each month and $S_{125}$ bin. Compared to simulation, where primary energies up to 300 PeV are used, the data points only go up to $\log_{10}(S_{125})$=1.5 (~40 PeV), due to a lack of statistics. The result is shown in Figure 5 for seven months with July 2010 as the reference atmosphere.

When all months are used to determine the correlation coefficient, $\tilde{\alpha}_{\text{data}}$ is $0.81 \pm 0.28$ is found, where the error is obtained from a separate fit to each $S_{125}$ bin in order to show the maximal spread. This is described in Section 5. When looking in detail to Figure 5, two residual effects have been observed.

The evolution of the data points for a single month, for example January, shows an unexpected energy dependence, while the energy dependence should already be included in $\tilde{T}_{\text{eff}}$. The same shape of this energy dependence can be seen in the other months.

Furthermore, the months during austral spring (October, November, December) show a smaller correlation compared to the months during austral fall (March, April). This hysteresis effect, which is not seen in the simulation study, will cause a spread when applying the correction: the months during austral spring or austral fall will be over- or undercorrected, respectively.

Several possible explanations for these features have been investigated, including the seasonal variation of $S_{125}$, the influence of the hadronic interaction model, the energy threshold of the muons to generate light in the IceCube detector, the evolution of the $< \log A >$ of cosmic ray air showers with energy, etc. However, none of them could explain the energy dependence or the hysteresis.

## 5 Energy dependence of $\tilde{\alpha}$

When a correction with a constant $\tilde{\alpha}$ is applied, a discrepancy between the mean energy loss and the true energy loss may remain at certain energies. This might induce a wrongly reconstructed composition at the affected ener-

gies. Hence, we propose to absorb the energy dependence in the correlation factor $\tilde{\alpha}$.

By fitting the data points in Figure 5 separately for the various $S_{125}$ bins, one obtains the energy dependence of $\tilde{\alpha}$. This is shown in Figure 6 for both data and simulation. The data points are fitted with a fourth-order polynomial function for $\log_{10}(E_0/\mathrm{GeV})$ <7.8 , while the points obtained from simulation are not included in the fit. A constant fit to the simulation is used above these energies, since data cannot be used due to limited statistics. This energy dependent $\tilde{\alpha}$ will be used for correcting the energy loss of the muon bundle.

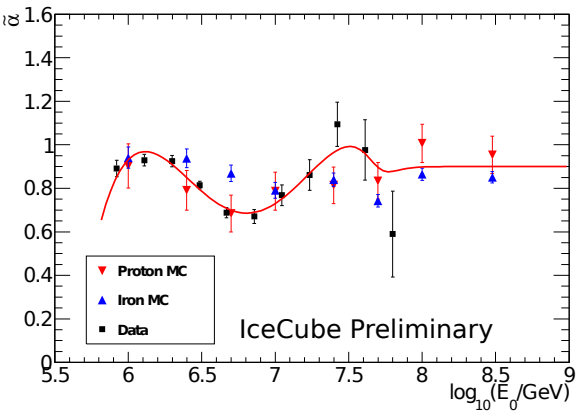


**Figure 6**: $\tilde{\alpha}$ as a function of energy, for data and both proton and iron simulation. For data, the conversion from $S_{125}$ to energy is done, as in Eqn. 3.

## 6 Results

Figure 7 shows the uncorrected and corrected difference of $\log_{10}\left(\mathrm{d}E_\mu/\mathrm{d}x\right)_{\mathrm{bundle}}$ for the various months with respect to July 2010, as a function of $S_{125}$. The difference is normalized to $\Delta\log_{10}\left(\mathrm{d}E_\mu/\mathrm{d}x\right)_{\mathrm{bundle}}$ between proton and iron. The upper figure shows that the maximal seasonal variations of the mean $\log_{10}\left(\mathrm{d}E_\mu/\mathrm{d}x\right)_{\mathrm{bundle}}$ are between 10 and 15 % of the mean proton-iron separation. The lower figure shows the $\Delta\log_{10}\left(\mathrm{d}E_\mu/\mathrm{d}x\right)_{\mathrm{bundle}}$ between July 2010 and the other months, again compared to the proton-iron difference, after the correction applied with the energy dependence of $\tilde{\alpha}$ described in the previous section.

Hence, the seasonal variation of the energy loss can be reduced from 10-15 % in the proton-iron phase space to about ±3 %, except at the highest energies, where we do not have enough statistics. The remaining ±3 % of variation is due to the hysteresis. For each energy, the mean energy loss from the entire year will be close to the one obtained from simulation.

## 7 Conclusions

For the first time, the seasonal variation of the muon multiplicity in cosmic ray air showers has been investigated. The difference in energy loss of the muon bundle has been related to the variation in $\tilde{T}_{\mathrm{eff}}(E_0, A)$, which weights the temperature profile of the atmosphere with the muon production profile (the latter depends on the energy and mass of the primary particle). A correlation factor has been deduced, both in data and simulation. In data, an unexpected energy dependence and hysteresis has been seen. In order to account for this energy dependence, we proposed an empirical correction, based on an energy dependence of the correction factor.

When a correction is applied to the energy loss, we are able to reduce the seasonal variation from 10-15 % to ±3 % of the proton-iron difference, except at the highest energies. The remaining ±3 % is due to the hysteresis effect. Adding more years of data will provide extra information at the high energies, where we lack statistics. We will investigate the energy dependence and hysteresis in data further.

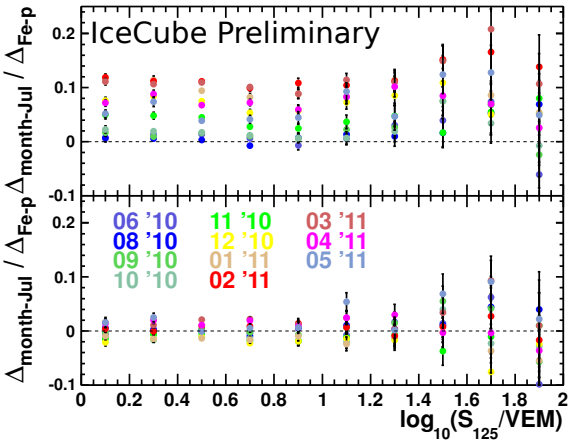


**Figure 7**: The uncorrected (up) and corrected (down) $\Delta\log_{10}\left(\mathrm{d}E_\mu/\mathrm{d}x\right)_{\mathrm{bundle}}$ for all months with July 2010 as a reference ($\Delta_{\mathrm{month-Jul}}$), as a function of $\log_{10}(S_{125})$. The difference is normalized to the difference in $\Delta\log_{10}\left(\mathrm{d}E_\mu/\mathrm{d}x\right)_{\mathrm{bundle}}$ between proton and iron ($\Delta_{\mathrm{Fe-p}}$), obtained by fitting the proton and iron curves in Figure 1.

## References

[1] S. Tilav et al., Proc. 31st ICRC, 2009, Lodz, Poland, arXiv:1001.0776.
[2] P. H. Barrett et al., Rev. Mod. Phys. 24(3) (1952) 133-178.
[3] A.Achterberg et al., Astropart. Phys. 26 (2006) 155-173 doi:10.1016/j.astropartphys.2006.06.007.
[4] R.Abbasi et al., Nucl. Instrum. Meth. A700 (2013) 188-220 doi:10.1016/j.nima.2012.10.067.
[5] R. Abbasi et al., Astropart. Phys. 42 (2013) 15-32 doi:10.1016/j.astropartphys.2012.11.003.
[6] IceCube Collaboration, paper 861, these Proceedings.
[7] T.K. Gaisser, 1990, Cosmic Rays and Particle Physics, ed. 284 CUP.
[8] IceCube Collaboration, paper 246, these Proceedings.
[9] http://amrc.ssec.wisc.edu/
[10] http://aqua.nasa.gov/
[11] D.Heck et al., CORSIKA FZKA 6019 (1998).
[12] E.Ahn, R.Engel, T.Gaisser, P.Lipari, and T.Stanev, Phys. Rev. D80 (2009) 094003 doi:10.1103/PhysRevD.80.094003.
[13] G.Battistoni et al, AIP Conference proceedings 896 (2007) 31-49.

33RD INTERNATIONAL COSMIC RAY CONFERENCE, RIO DE JANEIRO 2013
THE ASTROPARTICLE PHYSICS CONFERENCE

ICRC 2013

# Cosmic Ray Composition and Energy Spectrum between 2.5 PeV and 1 EeV with IceTop and IceCube

THE ICECUBE COLLABORATION[1]

[1]*See special section in these proceedings*

*tom.feusels@ugent.be*

**Abstract:** The mass composition and all-particle energy spectrum of cosmic rays are determined by analysis of coincident events between the IceTop air shower array on the surface and the deep IceCube strings. IceTop mainly detects the electromagnetic component of high energy cosmic ray air showers, while the TeV muon bundle penetrates deep into the Antarctic ice and generates Cherenkov light, which is seen by IceCube.
This analysis uses data taken from June 2010 to May 2011 when the detector was nearly complete with IceCube in its 79 string conguration and IceTop running 73 stations. Variables sensitive to composition and primary energy are based on the lateral signal distribution reconstructed at the surface by IceTop and the energy loss of the muon bundles reconstructed by IceCube. Using a neural network we determine the average mass A and all-particle flux in the energy range from a few PeV up to 1 EeV. We find that $< \log A >$ increases up to at least 100 PeV.

**Corresponding authors:** Tom Feusels[1], Katherine Rawlins[2]
[1] *Dept. of Physics and Astronomy, University of Gent, B-9000 Gent, Belgium*
[2] *Dept. of Physics and Astronomy, University of Alaska Anchorage, Anchorage AK, USA*

**Keywords:** IceCube, IceTop, all-particle energy spectrum, cosmic ray composition.

## 1 Introduction

The measurement of the cosmic ray composition in the PeV to EeV energy range will provide an insight into the acceleration and propagation mechanisms of galactic and extra-galactic cosmic rays. The IceCube Neutrino Observatory [1], located at the geographic South Pole (2835 m altitude), is ideally suited to measure the cosmic ray composition and energy spectrum as it detects both the electromagnetic and high energy muonic component of cosmic ray air showers. IceCube is a cubic-kilometer neutrino detector installed in the ice between depths of 1450 m and 2450 m. The surface air shower array, IceTop [2], consists of 81 stations with two ice-Cherenkov tanks per station. Detector construction started in 2005 and finished in 2010.

In [3] the 73-station analysis of the energy spectrum is described using IceTop alone. Here we will describe the first results of the same detector configuration for coincident events which also passed through the 79 strings of IceCube using a full year of data. Although the statistics will be smaller, the main advantage is that we can obtain a composition independent energy spectrum while the composition itself is measured at the same time.

## 2 Data and Simulation

We use data from the 79-string and 73-station detector from June 1, 2010 until May 12, 2011, comprising a total livetime of 310 days, calculated based on a fit to the distribution of time differences between consecutive events. The fit uncertainty of 0.4 days is negligible. Only good runs longer than 10 minutes and taken during stable operations of both IceCube and IceTop are used.

To extract the relation between the reconstructed observables in data and the primary mass and energy we rely on Monte Carlo (MC) simulations because there is no absolute calibration source. 30,000 CORSIKA [4] air showers between 100 TeV and 100 PeV are simulated for each of four primary masses (H, He, O and Fe) with Sybill 2.1 [5] as the hadronic interaction model above 80 GeV and Fluka [6] below. Between 10 PeV and 3.16 EeV, 12,000 thinned CORSIKA showers of each type are generated. Events are simulated according to an $E^{-1}$ spectrum, in energy bins of 0.1 in $\log_{10}(E_0)$, with zenith angles between 0° and 40° and over the entire azimuth range. The atmospheric model based on South Pole atmosphere of July 1, 1997 is used as baseline because its ground pressure of 692.9 g/cm$^2$ well represents the average measured pressure at South Pole during the data period in 2010-2011. Each shower is resampled 100 times and thrown in an energy dependent resample radius. The interactions of secondary particles in IceTop tanks, including snow on top of the tanks, are simulated with GEANT4 [7]. The high energy muons are further propagated through the ice, while the emitted Cherenkov light is propagated taking into account the specific South Pole ice properties [8]. The electronics for both IceTop and IceCube optical modules and the trigger are simulated using IceCube software.

## 3 Reconstruction

Initially the first guess shower core position and direction are calculated. These are seeded in a maximum likelihood fitting procedure that uses the times and amplitudes of the tank signals to fit a curved shower front and a lateral distribution function (LDF) at the same time. This procedure is described in detail in [2] with some improvement for better fit stability and a saturation likelihood term to better account for signals close to the core. The main IceTop observable, sensitive to primary energy, used in this analysis is the shower size $S_{125}$, the fitted signal strength at 125 m

from the shower axis. Similarly as the IceTop-alone analysis [3], we corrected for the monthly, uneven snow accumulation due to snow drift. After all the containment and quality cuts described in Section 4, a core resolution better than 10 m and angular resolution of about 0.5° is obtained.

When cosmic ray air showers penetrate the ice, only collimated bundles of up to thousands of high energy muons reach the IceCube detection volume while the electromagnetic component is absorbed. IceCube detects the Cherenkov light emitted by these high energy (TeV) muon bundles as they lose energy through ionization and radiative processes. From the amplitude and timing of the detected light signals in the optical sensors when the bundle propagates through the ice, the energy loss profile $(\mathrm{d}E_\mu/\mathrm{d}X)_{\mathrm{bundle}}(X)$ is reconstructed.

An unfolding procedure is used to reconstruct the energy losses along track segments on the muon bundle. The response matrix incorporates the expected Cherenkov light emission, propagation and absorption and scattering properties of the South Pole ice. The example of the reconstructed energy loss profile on Figure 1 shows the stochastic behavior of a large event in the 2010-2011 data sample.

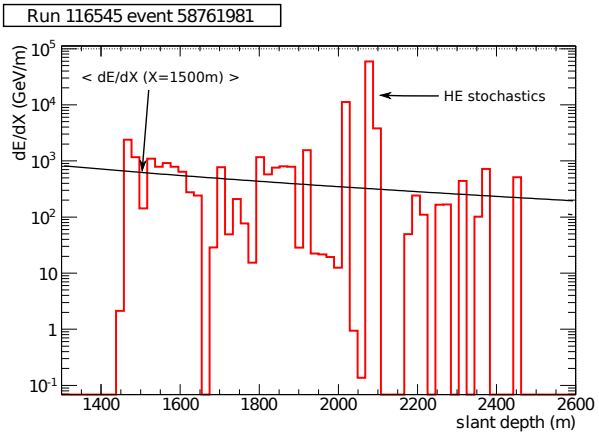


**Figure 1**: Example of the muon bundle energy loss reconstruction for one event of about 200 PeV.

The average energy loss profile is then fitted to the reconstructed profile based on the muon bundle energy loss function derived in [9]:

$$\left(\frac{\mathrm{d}E_\mu}{\mathrm{d}X}\right)_{\mathrm{bundle}}(X) = \int_{E_{\mathrm{min}}}^{E_{\mathrm{max}}} \frac{\mathrm{d}N_\mu}{\mathrm{d}E_\mu}(A, E_0, \theta, E_\mu, X)\frac{\mathrm{d}E_\mu}{\mathrm{d}X}\,\mathrm{d}E_\mu.$$

The muon bundle energy loss at a fixed slant depth depends highly on the muon multiplicity and is therefore a strong composition sensitive observable. In addition, the stochastic behavior also provides information on the composition. The probability that several muons give radiative energy losses on the same track segment is higher for iron, which has higher multiplicities. Therefore the number of reconstructed high energy stochastic energy losses (Figure 1) is a composition sensitive property of the bundle. Two selection criteria are used. The first one selects energy losses which are five times higher than the fitted average loss, while the stronger criteria, which performs better above 100 PeV, selects energy losses which are at least seven times higher.

As already seen in the previous IceCube composition analysis [10], seasonal variations at South Pole highly influence composition sensitive observables based on the muon multiplicity. In [11] a procedure is developed to correct the seasonal variations on the reconstructed variables which are used as input in the neural network, described in Section 5.1.

## 4 Event Selection

A good determination of the shower axis, characterized by its core position on the surface and its direction, is important to limit the smearing in detector response and will therefore minimize the energy resolution. To acquire the excellent angular and core resolution mentioned in Section 3, only events which are contained by the IceTop array are selected. In addition basic quality cuts on the reconstruction of the lateral distribution and reconstructed energy loss are applied.

The only background in a coincident IceTop-IceCube analysis are multiple coincidences and random coincidences. These coincident events could create artifacts due to bad reconstructions and are not simulated, but these events are cleaned in data such that only hits related to the event that passes through both IceTop and IceCube remain. The first class of multiple coincidences are coincident IceTop showers where one of the multiple showers, that hits IceTop, triggers IceCube. The second class are events where a muon track passes through the IceCube detector before the coincident IceTop-IceCube air shower passes through. Random, unrelated IceTop-IceCube coincident events form the last class of background. These are caused by an event that hit the IceTop array while around the same time a muon track passes through the IceCube volume. The bulk of these random coincidences are cut away based on the time difference between IceTop and IceCube triggers.

The effective area as a function of energy after all cuts (Figure 2) shows that the detector is fully efficient for this analysis from 2.5 PeV onwards where it is $1.36 \cdot 10^5$ m$^2$ and that this effective area is composition and energy independent.

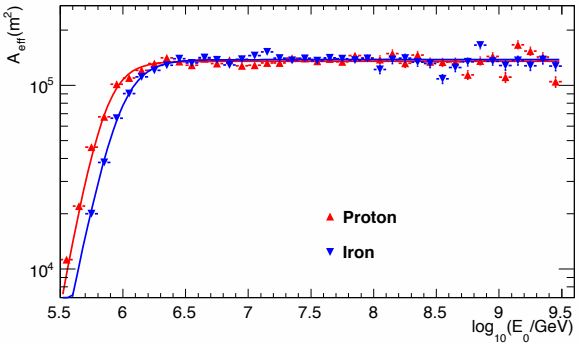


**Figure 2**: The effective area after all cuts for proton and iron showers. Both are fitted with a sigmoid function.

## 5 Analysis

### 5.1 Neural Network

The relation between the primary energy, primary mass and reconstructed variables is highly non-linear and is a complex mapping of n to 2 dimensions. A multilayer perceptron neural network (NN) is the ideal regression tool

to find and solve this non-linear mapping. A similar procedure as the previous IceCube composition analysis [10] is done to train, test and verify the NN. The total MC dataset is also divided in three subsets to avoid any bias, one quarter for training the network, one quarter for testing and choosing the best performing network, and one half to make the template histograms (see Section 5.2). A large range of different network architectures and two activation functions (sigmoid and tanh) are explored. The network shown in Figure 3 is selected based on the following criteria : (i) overall performance in the energy and mass reconstruction (ie. minimizing resolution, spread and bias), (ii) maximal separation of the template histograms, and (iii) energy dependence of the resolution and bias in energy reconstruction. The five primary mass and energy sensitive observables used as NN inputs are the shower size $S_{125}$, the average energy loss at a fixed slant depth of 1500 m ($\mathrm{d}E/\mathrm{d}X$), the zenith angle $\theta$, the number of HE stochastics using a standard selection and the number of HE stochastics using a strong selection (as described in Section 3).

The final performance of the chosen NN for energy reconstruction is shown in Fig. 4, where the energy bias is defined as the mean of a gaussian fit to the $\log_{10}(E_{\mathrm{reco}}/E_{\mathrm{true}})$ distribution and its sigma is the resolution. The NN gives a very good energy resolution, much smaller than 0.1 in $\log_{10}(E)$ and a bias much smaller than the energy binning.

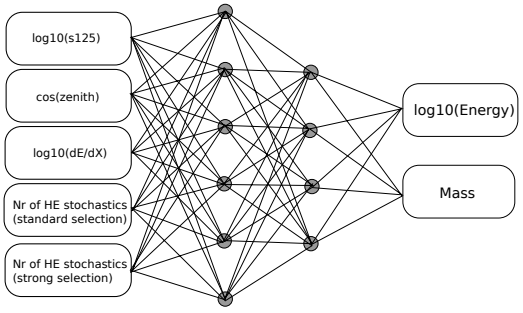


**Figure 3**: The 5-6-4-2 network used in this analysis. Five input variables from both IceTop and IceCube are mapped to 2 output variables, primary mass and primary energy. Two hidden layers are used, with 6 nodes in the first layer and 4 nodes in the layer. The activation function is a tanh.

## 5.2 Template Fitting

Although the neural network is trained to find the mass for individual events based on their reconstructed input variables, the spread of the reconstructed NN mass output for a certain reconstructed energy bin is still quite large as can be seen on Figure 5. This is due to the intrinsic shower fluctuations and the fact that the overlap between different mass groups in the input variables is relatively large. The NN allows the different nuclear types to be separated into more distinct distributions and we can use the shapes of these distributions as characteric template shapes to fit the data NN mass distribution.

For each reconstructed energy bin, template histograms are created for each of the four simulated mass groups based on the half of the total MC dataset not used for NN training and testing. Using an unbinned likelihood fit [12] that takes into account both Poisson fluctuations on the individual bins in the data distribution as well as Poisson

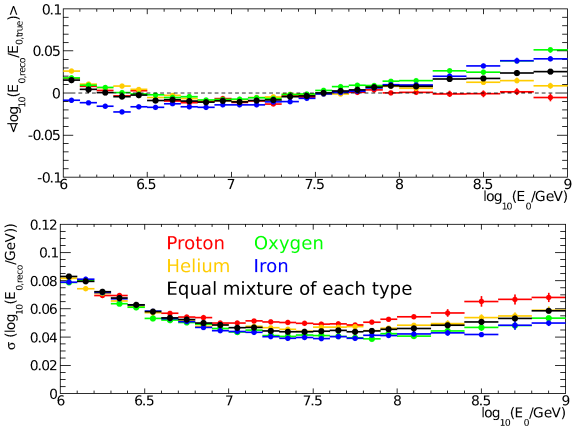


**Figure 4**: The energy bias (top) and resolution (bottom) of the reconstructed energy by the NN for proton, helium, oxygen, iron and an equal mixture of all types.

fluctuations on the MC templates, the fractions of each mass group are fitted. The mean log mass is then calculated based on the reconstructed fractions. The full procedure is tested first on hand-mixed (blind) samples of MC, where for each of the samples the reconstructed $< \log A >$ agreed well with the truth.

The energy binning for the method is chosen to ensure that the number of total MC events for a template histogram is sufficiently large to keep the Poisson fluctuations on the total number of events in the histogram small (below 20% in the highest energy bin). The binning of the template histograms and the number of mass groups fitted is optimized based on the hand-mixed MC test sets. Finer binning in the templates gives more distinct histograms, but also larger Poisson fluctuations per bin.

In Figure 5 the four individual templates for each of the mass groups are shown for the reconstructed energy bin between 7.6 and 7.7 in $\log_{10}(E_0/\mathrm{GeV})$. The result of the unbinned likelihood fit (magenta histogram) describes the fake data distribution (in black) very well.

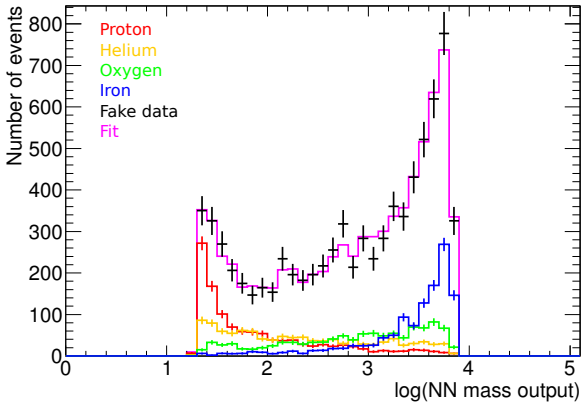


**Figure 5**: Template histograms for four mass groups in the reconstructed energy bin $\log_{10}(E_0) \in [7.6, 7.7]$ for a fake dataset scrambled from MC.

# 6 Results

## 6.1 Energy Spectrum

Data can be directly run through the trained neural network and for each event we get its composition independent reconstructed energy. To convert a distribution of event counts as function of the logarithm of the reconstructed energy $\frac{dN}{d\log_{10}(E)}$ to a differential flux $\frac{d\Phi}{dE}$, we need to account for the effective area $A_{\rm eff}$ as shown in Figure 2, solid angle $\Omega$ and livetime $t$ :

$$E\frac{d\Phi}{dE} = \frac{1}{t\Omega A_{\rm eff}\log(10)}\frac{dN}{d\log_{10}(E)}.$$

To minimize threshold effects the energy ranges from 6.4 to 9.0 in $\log_{10}(E/\mathrm{GeV})$. Above 1 EeV the energy resolution and bias becomes much worse, as does the reconstruction quality. The energy binning (on log scale) is 0.1 below 6.5, 0.05 between 6.5 and 8.0, and 0.1 above 8.0. No unfolding is performed, but the effect of bin-to-bin migration has been taken into account. In Figure 6 the energy spectrum for coincident IceTop-IceCube events and IceTop-alone for 2010-2011 data are plotted. Both spectra agree very well within the composition uncertainty of the IceTop 73 analysis and the same spectral features are visible in both spectra.

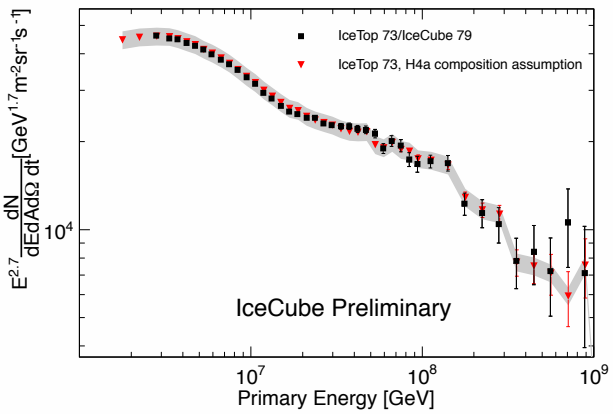


**Figure 6**: The differential energy spectrum multiplied by $E^{2.7}$ for 2010-2011 data, compared with the IceTop 73 measurement from [3], which has a $\pm 7\%$ gray systematic error band due to the composition uncertainty. The other systematic uncertainties, common between both analyses, are not included.

## 6.2 Composition

For each reconstructed energy bin, the template fitting algorithm gives the fractions of each individual mass group ($p_H, p_{He}, p_O, p_{Fe}$) and its uncertainties. The mean log mass is then calculated as :

$$\begin{aligned} <\log A> = {} & p_H\log(A_H) + p_{He}\log(A_{He}) \\ & + p_O\log(A_O) + p_{Fe}\log(A_{Fe}), \end{aligned}$$

and the covariance matrix from the fit are propagated to the error on $<\log A>$.

In Figure 7 the mass composition for 2010-2011 data is shown with conservative systematics included. Above 630 PeV statistics is currently too low to perform the template fitting. The composition is clearly getting heavier up to 630 PeV.

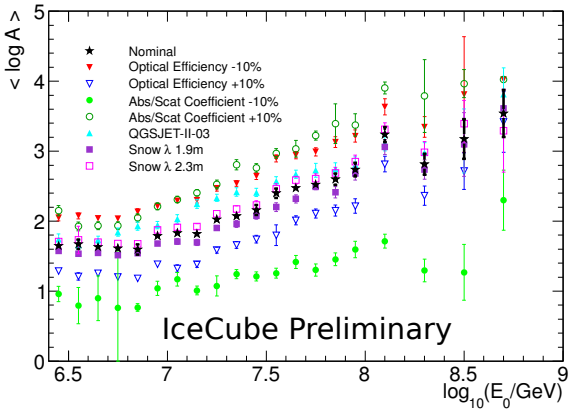


**Figure 7**: The $<\log A>$ composition spectrum as function of primary energy for 2010-2011 data.

# 7 Conclusions and Outlook

Due to the larger detector, improved simulation, reconstruction, and analysis tools we were able to reconstruct a composition independent energy spectrum and a composition spectrum up to 630 PeV using data from 2010-2011 from events which triggered both the IceTop and IceCube detector. Both the energy spectrum obtained here and the IceTop 73 measurement agree very well and show the same spectral features. In addition, an increasing heavier composition up to 630 PeV is seen.

The main systematic uncertainties in the energy spectrum measurement are the same as the IceTop alone analysis [3] (ie. hadronic interaction model, snow, absolute calibration) because the energy conversion is still largely dominated by the shower size $S_{125}$. NN variables most sensitive to composition are related to the absolute energy scale and hence the absolute light yield measured by IceCube. Therefore the uncertainty on absorption and scattering coefficient of the ice model[8] and on the efficiency of the optical modules are the largest systematics in the composition measurement. Detailed studies to improve the systematic uncertainties are ongoing.

# References

[1] A.Achterberg et al., Astropart. Phys. 26 (2006) 155-173 doi:10.1016/j.astropartphys.2006.06.007.
[2] R.Abbasi et al., Nucl. Instrum. Meth. A700 (2013) 188-220 doi:10.1016/j.nima.2012.10.067.
[3] IceCube Collaboration, paper 0246, these Proceedings.
[4] D.Heck et al., CORSIKA FZKA 6019 (1998).
[5] E.Ahn, R.Engel, T.Gaisser, P.Lipari, and T.Stanev, Phys. Rev. D80 (2009) 094003 doi:10.1103/PhysRevD.80.094003.
[6] G.Battistoni et al, AIP Conference proceedings 896 (2007) 31-49.
[7] S.Agostinelli et al., Nucl. Instrum. Meth. A506 (2003) 250-303 doi:10.1016/S0168-9002(03)01368-8.
[8] M. Aartsen et al., Nucl. Instrum. Meth. A711 (2013) 73-89 doi:10.1016/j.nima.2013.01.054.
[9] T. Feusels et al., Proc. 31st ICRC, Lodz, Poland, 2009, arXiv:0912.4668.
[10] R. Abbasi et al., Astropart. Phys. 42 (2013) 15-32 doi:10.1016/j.astropartphys.2012.11.003.
[11] IceCube Collaboration, paper 0763, these Proceedings.
[12] R. Barlow and C. Beeston, Comp. Phys. Comm. 77 (1993) 219-228 doi:10.1016/0010-4655(93)90005-W.

33RD INTERNATIONAL COSMIC RAY CONFERENCE, RIO DE JANEIRO 2013
THE ASTROPARTICLE PHYSICS CONFERENCE

ICRC 2013

# Inclined Cosmic Ray Air Showers in IceCube

THE ICECUBE COLLABORATION[1]

[1]*See special section in these proceedings*

*javierg@udel.edu*

**Abstract:**
In this contribution we will consider the sensitivity of IceCube to inclined air showers produced by cosmic rays. Cosmic ray air shower analyses done with IceCube up to now only considered air showers arriving within a limited zenith angle range. IceTop analyses have included events up to about 40 degrees while coincident IceCube/IceTop analyses are limited to zenith angles smaller than 30 degrees. We study the possibility of extending the angular range to 60 degrees for both IceTop and coincident IceCube/IceTop. In the case of coincident IceCube/IceTop inclined events, the detector aperture is larger than that of IceTop at energies larger than 100 PeV due to the sensitivity to single muons at large distances from the shower axis. As part of this study, we have measured the average lateral distribution of muons at large distances to the shower axis.

**Corresponding author:** Javier G. Gonzalez[1]
[1] *University of Delaware and Bartol Research Institute*

**Keywords:** Air showers, muons, inclined air showers, IceCube, IceTop.

## 1 Motivation

It is well known that the muon content of an air shower, together with a measure of its electromagnetic component, can be used to estimate the energy and mass of its primary [1]. The IceCube collaboration has taken advantage of this in order to study the spectrum and mass-composition of cosmic rays between 1 PeV and 1000 PeV [2]. The main issue with the use of the muon content as an estimate of primary mass is the possible systematic differences between simulated and real air showers, arising from the lack of knowledge of high energy hadronic interactions, as shown by the Pierre Auger Observatory [3]. The angular dependence of the cosmic ray spectrum can be used as cross-check of any such systematic difference [4]. For this reason, we want to extend as much as possible the angular range of the cosmic ray air showers studied in IceCube.

Another reason to extend the detector field of view is to search for hints of a possible galactic/extra-galactic transition above 100 PeV. According to Giacinti et al. [5], the flux of *heavy* cosmic rays with galactic origin, with energies around $1 \times 10^{17}$ eV, should show a large-scale anisotropy of a few percent. One can argue that the *light* cosmic rays that dominate the flux are predominantly of extra-galactic origin and for this reason no anisotropy has been measured between $1 \times 10^{17}$ and $1 \times 10^{18}$ eV. This leaves open the question of whether the heavy component displays some degree of anisotropy. The very first step in order to study the large-scale anisotropy of the heavy component is to increase the detector field of view.

Finally, the study of inclined air showers can lead to a direct determination of the muon content of air showers on an event-by-event basis. Of particular interest are the events where IceTop can be used to directly measure the muons far from the shower axis, enabling the study of new observables sensitive to primary composition, such as the Muon Production Depth distribution (MPD), as is done by the Auger collaboration [6]. In order to study this class of events, we require a detailed knowledge of the sensitivity of the detector and of the lateral distribution of muons in real air showers. The study of the lateral trigger probability as well as the muon lateral distribution function, using the IceTop detector, is presented in section 3. Using this knowledge, we can estimate the efficiency for detecting inclined air showers under various conditions. This will be shown in section 4.

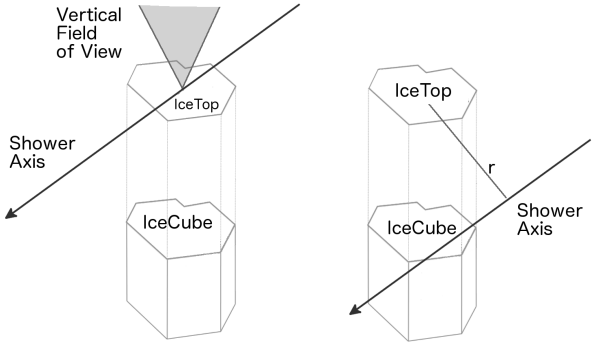


(a) IceTop-contained (b) IceCube-contained

**Figure 1**: The two kinds of inclined air showers detected by IceCube. Compare with the field of view studied so far in IceCube represented by the inverted cone.

We can distinguish two types of *inclined* air showers reaching IceCube, as shown in Fig. 1: the *IceTop-contained* showers, whose symmetry axis passes through the IceTop array, thereby completely missing the in-ice detector, and the *IceCube-contained* showers, whose symmetry axis passes through the in-ice component of IceCube. In this contribution we will be especially interested in *IceCube-contained* events.

## 2 IceCube as a Cosmic Ray Detector

The IceCube detector is composed of two major components. It can measure air showers on the surface with IceTop, high energy muon bundles with the in-ice detector, and both components in coincidence provided that its axis goes through the in-ice detector.

In its final configuration, the in-ice detector consists of 86 strings of 60 Digital Optical Modules (DOMs) each, extending from 1.5 km to 2.5 km under the ice. Each DOM contains a 10 inch photomultiplier tube (PMT) and electronics for signal processing and readout. The strings are separated by about 125 m. IceTop is an air shower array consisting of 81 stations, located above the in-ice detector, covering an area of one square kilometer. Each station consists of two ice Cherenkov tanks separated by ten meters.

Each IceTop tank contains two DOMs operating with different PMT gains for increased dynamic range, registering signals ranging from 0.2 to 1000 Vertical Equivalent Muons (VEM). A discriminator trigger occurs when the voltage in one of the DOMs in a tank has passed the discriminator threshold. A *Hard Local Coincidence* (HLC) occurs when there are discriminator triggers in two neighboring tanks within a time window of $\pm 1$ µs. If there is a discriminator trigger but not an HLC, the result is a *Soft Local Coincidence* hit (SLC). The SLC hits have a significant contribution from single muons while the HLC hits are a measure of the electromagnetic component of the air shower. The total charge collected at the PMT's anode constitutes the tank's signal. The primary cosmic ray properties are reconstructed by fitting the measured charges with a Lateral Distribution Function (LDF) and the signal times with a function describing the shape of the shower front. The primary energy is given by the shower size, defined as the signal at 125 m from the shower axis $S_{125}$. For a more detailed description of IceTop, refer to [7].

The cosmic ray energy spectrum has been measured with IceTop in the energy range between 1.58 PeV and 1.26 EeV by studying air showers arriving within 46°[8] and 37°[9] from the vertical, which we called IceTop-contained events. The zenith angle restriction is especially important when requiring that the air showers are contained within IceTop and in-ice detectors [2], in which case the zenith angle is always less than 30°. The muon bundle multiplicity spectrum in IceCube-contained events has been studied as well and it is sensitive to the primary mass composition [10]. However, in this later case, no attention was paid to whether the air shower was detected by IceTop or not and therefore no combined reconstruction was attempted.

For this contribution, we have analized data taken by the IceTop array from June 1, 2010 to May 13, 2011 when IceTop consisted of 73 stations. The effective livetime of the detector during this time interval is 327 days.

## 3 The Lateral Distribution Function

An example of the average LDF for air showers, with fixed $S_{125}$ and zenith angle, can be seen in Fig. 2. At large distances, there are two distinct populations. One population is the continuation of the main distribution at smaller distances, where the electromagnetic component of the shower dominates. The other population, with signals around 1 VEM, is made up mostly of tanks hit by one or more muons. These two populations are clearly seen in Fig. 3, where we show the histograms of collected charge for all tanks at selected fixed distances to the shower axis.

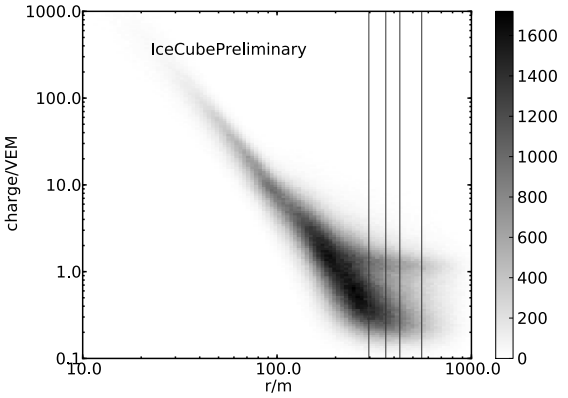


**Figure 2**: 2-d histogram of the tanks' total charge (in VEM), including SLC and HLC hits, and its distance to the shower axis (in meters) for events with $S_{125}$ between 4 and 5 VEM, which corresponds to energies around 4 to 5 PeV, and zenith angle between 30° and 33°. The vertical lines mark the distances at which the 1-d histograms in Fig. 3 were made.

The first population corresponds to the tanks detecting no muons. We approximate this distribution by a power-law multiplied by a function that describes the trigger probability. The trigger probability can be described by a sigmoidal function of the logarithm of the charge, centered at 0.25 VEM and with a width of 0.14. This approximation works well at large distances from the shower axis.

The second population, with a peak around 1 VEM, can be described by the contributions of tanks detecting an integer number of muons, determined by detailed simulations of the detector response. These contributions are weighted according to a Poisson distribution with a given mean number of muons $\langle N_\mu \rangle$. The resulting distribution is smeared and shifted to account for a very small contribution from electrons, positrons, and $\gamma$-rays. These parameters are left free in the fitting procedure.

We can fit the charge distribution at a sufficiently large distance from the shower axis using the distributions just described. The result is the number of tanks hit by at least one muon. This, together with the total number of tanks located at that distance provide an estimate of the probability to be hit by one or more muons, which leads to the mean number of muons $\langle N_\mu \rangle$:

$$p_{\mu\,hit} = 1 - e^{-\langle N_\mu \rangle}. \quad (1)$$

In order to ensure that the distance from the shower axis is sufficiently large, this procedure is applied only to the charge distributions of tanks located at distances larger than a value that can depend on $S_{125}$ and zenith angle. This minimum distance is defined such that, given any tank with signal at this distance, there is less than 10% chance probability that it is an HLC. This can easily be determined at all $S_{125}$ and zenith angle values by looking at the corresponding distribution of tanks, such as the one displayed in Fig. 4. From these distributions, we can also estimate the probability that any tank at a given distance to the shower axis will record a hit, also called the Lateral Trigger Probability (LTP).

The resulting muon lateral distributions, corresponding to air showers arriving within 31° from the vertical, and

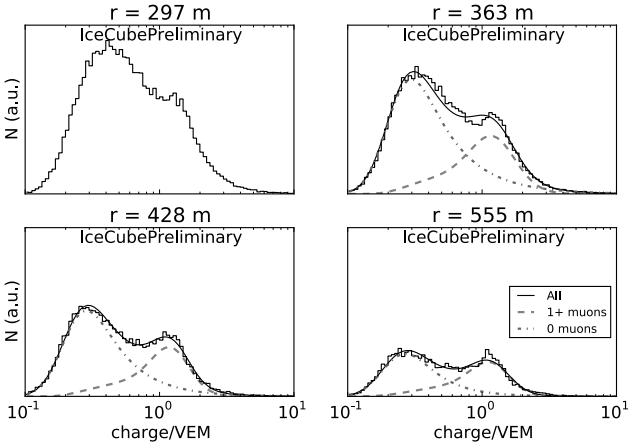


**Figure 3**: Vertical slices of the 2-d histogram in Fig. 2. Each histogram corresponds to a vertical line in Fig. 2. They correspond to the radii at which the probability that a given tank with signal is part of an HLC is 0.1, 0.2, 0.3, and 0.5. At 297 m, the model described does not fit the distribution.

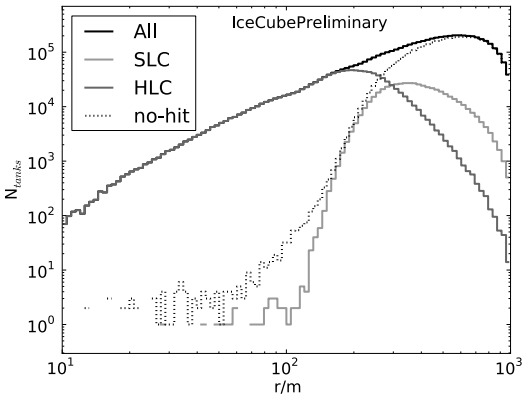


**Figure 4**: The radial distribution of all tanks (black), tanks with HLC (dark gray), tanks with SLC (light gray), and tanks with no hits (dotted) for events with $S_{125}$ between 4 and 5 VEM and zenith angle between 30° and 33°. Note that SLC hits dominate at large distances.

selected $S_{125}$ bins, are shown in Fig. 5. Each LDF can be described by the following function:

$$N_\mu(r) = A\, S_{125}{}^{\beta}\, r^{-0.75} \left(1 + \frac{r}{320\text{m}}\right)^{-\gamma}, \qquad (2)$$

where we decided to fix the first exponent of r to -0.75, and the equivalent to the Moliere radius to 320 meters, as measured by Greisen [11], and fit the rest of the parameters.

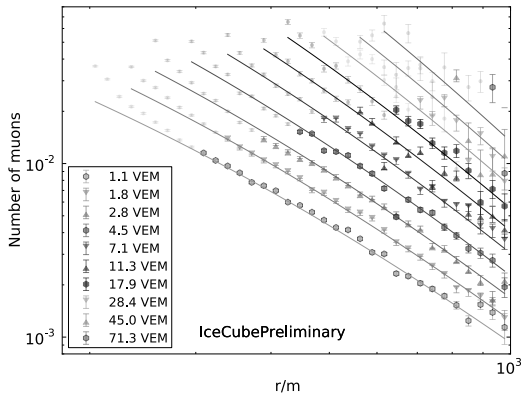


**Figure 5**: Reconstructed average lateral distribution of muons for air showers arriving at zeniths angles of 31° with the vertical and selected $S_{125}$ values. The small markers correspond to points below the radial cut and not used in the fitting procedure.

## 4 Detection Efficiency for Inclined Air Showers

In order to estimate the efficiency for the detection of inclined IceCube-contained showers, we implemented a simple Monte Carlo algorithm. The first step of the algorithm is to generate a random geometry (position and direction) that intersects the in-ice detector. The next step is to choose either a primary energy or a value for $S_{125}$. The primary energy determines the mean value for $S_{125}$, using a relation known for angles up to 37° [9] extrapolated up to 60°. Given the geometry and $S_{125}$, we then use the lateral trigger probability, determined as described in the previous section, to generate many realizations of sets of tanks with signal. We can finally impose various conditions for detection and calculate the fraction of detected events. The precise condition to be used in the future will depend on the required reconstruction quality and is not determined at this time.

One can require that there be a certain number of SLCs or HLCs. As an example, the resulting detection efficiency as a function of zenith angle, for different $S_{125}$ values, can be seen in Fig. 6. We show two different conditions, one requiring 10 SLCs and another requiring 3 HLCs. It becomes apparent that, at large zenith angles, the events consist mostly of SLC hits. This is because the local trigger probability is more evenly distributed over the array.

The most striking feature is the increase in efficiency that occurs at zenith angles larger than 45°. To understand this, we need to remember that the lines in Fig. 6 correspond to air showers with fixed $S_{125}$. The feature is a reflection of the fact that, as the air shower zenith angle increases, it has to traverse a larger amount of atmosphere and the muon component gives a larger relative contribution at ground, thereby decreasing the steepness of the LDF. That is: for a given $S_{125}$, the trigger probability at large distances to the shower axis increases with zenith angle. To make the point clearer, we show the LTP corresponding to events with an $S_{125}$ around 3.6 VEM in Fig. 7, where we can see how the tail of the LTP is steeper at small zenith angles.

The resulting effective area, as a function of zenith angle, is displayed in Fig. 8. In this figure, the thick solid line represents the surface area of IceTop projected at that zenith angle. The effective area for showers arriving at an angle of 60° with the vertical, with an energy of 112.9 PeV, is comparable to the effective area of IceTop.

The result of integrating the effective area over the azimuth and zenith range is the aperture. This is displayed in Fig. 9 as a function of the primary energy. Here it becomes apparent that, with a requirement of 10 IceTop SLCs in coincidence with the in-ice event, the aperture for IceCube-contained events is comparable to that of the

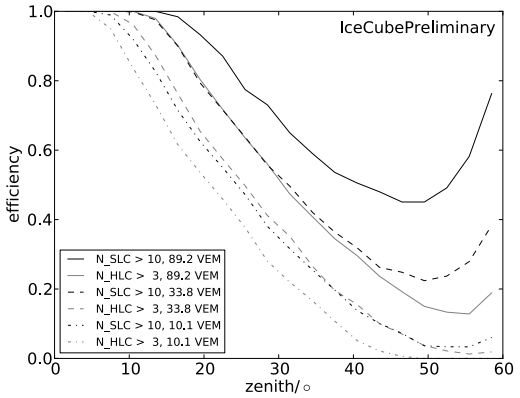


**Figure 6**: Detection efficiency for IceCube-contained inclined air showers with two different selection criteria. The SLC criterion requires a minimum of 10 SLCs. The HLC criterion requires a minimum of 3 HLCs. Both are displayed for selected $S_{125}$ values: 89.2, 33.8, and 10.1 VEM.

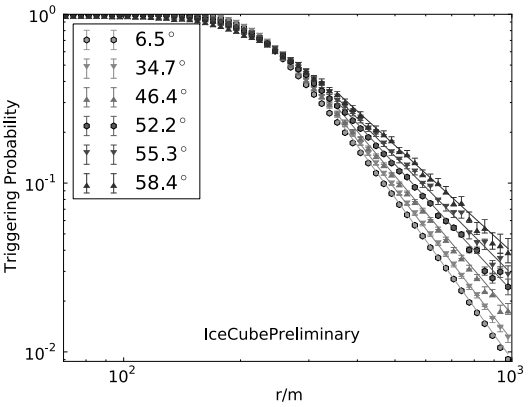


**Figure 7**: Lateral Triggering Probability (LTP) for air showers with $S_{125}$ =3.6 VEM and selected zenith angles. The LTP at large distances follows a power law with a steepeness that decreases with zenith angle.

current IceTop analysis at energies of the order of 25 PeV and more than doubles it at energies larger than 200 PeV. At 80 PeV it becomes larger than the aperture of IceTop for the same angular range. Therefore, the addition of IceCube-contained events should triple the statistics above 200 PeV when compared to the current analysis.

## 5 Outlook

By studying IceTop-contained air showers arriving with zenith angles up to 60°, IceTop can double the statistics over the entire energy range. We have also shown that the aperture of IceCube for the detection IceCube-contained cosmic ray air showers is more than double that of IceTop alone. The study of these events opens the possibility of studying the Muon Production Depth distribution function, which we intend to explore in the near future. The muon lateral distribution function presented here will enable us to determine the muon content of air showers on an event-by-event basis.

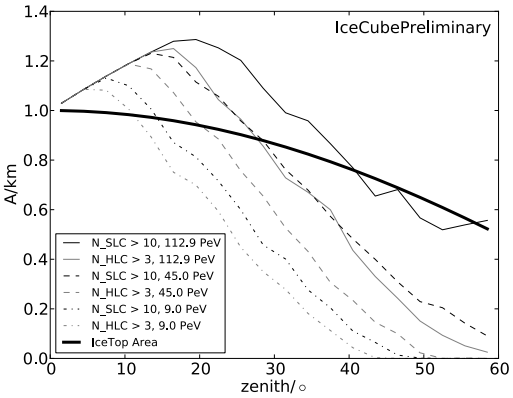


**Figure 8**: Effective area as a function of zenith angle for selected reconstructed energies.

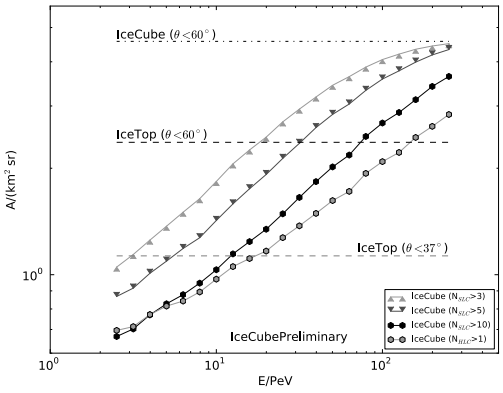


**Figure 9**: Aperture as a function of primary energy, assuming 100% in-ice detector efficiency. The horizontal lines correspond to the geometric aperture of the in-ice and IceTop components of IceCube. We show two values corresponding IceTop, for events with zenith angle less than 37° (1.14 km sr) and 60° (2.36 km sr).

## References

[1] J. Bluemer, R. Engel, and J.R. Hoerandel. *Prog.Part.Nucl.Phys.* 63 (2009) 293-338.
[2] IceCube coll., paper #861, this proceedings.
[3] A. Castellina and others for the Pierre Auger Collaboration. In *Proc. of the 31st ICRC, Lodz, Poland*, 2009.
[4] F. Schmidt, M. Ave, L. Cazon, and A. Chou. *Astropart. Phys.* 29 (2008) 355-365.
[5] G. Giacinti, M. Kachelriess, D.V. Semikoz, and G. Sigl. *JCAP*, 1207 (2012) 031.
[6] D. García-Gámez et al. In *Proc. of the 32nd ICRC, Beijing, China* 2011.
[7] R. Abbasi et al. *Nucl.Instrum.Meth.* A700 (2013) 188-220.
[8] R. Abbasi et al. *Astropart. Phys.* 44 (2013) 40-58.
[9] IceCube coll., paper #246, this proceedings.
[10] P. Berghaus for the IceCube Collaboration, In *Proc. of the 31st ICRC, Lodz, Poland*, 2009. arXiv:0909.0679 [astro-ph.HE].
[11] K. Greisen, *Ann. Rev. Nuc. Sci.* 10 (1960) 63.

# The Effect of Snow Accumulation on Signals in IceTop

THE ICECUBE COLLABORATION[1],

[1] *See special section in these proceedings*

*krawlins@uaa.alaska.edu*

**Abstract:** IceTop, the surface component of the IceCube Observatory at the South Pole, measures both the electromagnetic and muon components of cosmic ray air showers. Although initially deployed level with the snow surface, drifting snow buries the IceTop tanks under a layer of matter which attenuates the electromagnetic component and whose thickness changes slowly over time. Accounting for this attenuation is an important factor in correctly reconstructing the shower, but it is dependent on the shower's energy, composition, and zenith angle, as well as distance from the shower core. This work studies the attenuation of air shower particles and the effect of this attenuation on IceTop signals.

**Corresponding authors:** Katherine Rawlins[1],
[1] *University of Alaska Anchorage, Anchorage AK, USA*

**Keywords:** IceTop, snow, attenuation, air showers.

## 1 Motivation

IceTop [1] is the surface detector component of the IceCube Observatory [2]. IceTop's 81 cosmic ray detector "stations" are positioned near the top of IceCube's deeply-buried strings. Each station is composed of two tanks of frozen water; each tank contains two Digital Optical Modules (DOMs), one with high gain and one with low gain, which detect the Cherenkov light from charged particles passing through the tank. IceTop is sensitive to both electromagnetic particles and muons from cosmic ray air showers. The total charge deposited in each tank (which is measured in calibrated units of "vertical equivalent muons" or VEM) is used to reconstruct the properties of the shower, by fitting the distribution of charges to an expected functional form.

The IceTop site is the geographic South Pole, a high-altitude plateau where the snowy surface is ever-changing. Precipitation is minimal, but snowdrift driven by a prevailing wind slowly buries the IceTop tanks over time, especially those near buildings or structures, or which are located on sloped terrain. Figure 1 shows the depth of the snow layer above Station 40, which was deployed in January of 2007, as a function of time. Snow depth increases at an average rate of about 20 cm/year over the entire array. But the coverage of snow on the detector also builds unevenly; tanks deployed early in IceTop's construction history generally have accumulated the most snow, due to a combination of time, sloped terrain, and proximity to structures, as shown in Figure 2. In between regular *in situ* measurements of snow depths, the snow depth of a tank can be estimated using "VEMcal" calibration data in which the amount of signal from muons (which does not attenuate) is compared to the electromagnetic signal (which does) [1, 3].

The accumulated snow is *part* of the IceTop detector, as the particles observed will be attenuated by the layer above, affecting the charge observed in the tank and thus also the measured shower "size" $S_{125}$. Since $S_{125}$ is used by multiple IceTop analyses [4, 5, 6] to measure primary energy,

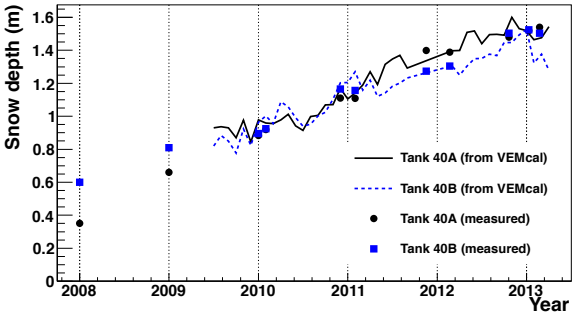


**Fig. 1**: Example of the accumulation of snow over time, for the two tanks in Station 40. Solid symbols are direct measurements of snow depth performed by scientists on-site. Lines are indirect measurements using VEMcal data taken weekly and smoothed monthly.

accounting for snow is critical. In fact, uncertainty in snow correction is the dominant source of systematic uncertainty for the spectrum measurements in these analyses.

## 2 A simple snow correction

The attenuation of electrons through matter is well-studied. A single (MeV) electron loses energy with a radiation length $X_0$ of about 37 g/cm$^2$ in ice [7]. High energy electrons can generate electromagnetic (EM) cascades in matter, which obey cascade equations [8]. So the electrons in an air shower experience attenuation which is a convolution of the particles' energy spectrum with the energy loss (according to cascade physics) at each energy. In particular, if the electrons have a $E^{-2.7}$ spectrum, the population as a whole is expected to be attenuated exponentially with the distance into the matter, with an effective attenua-

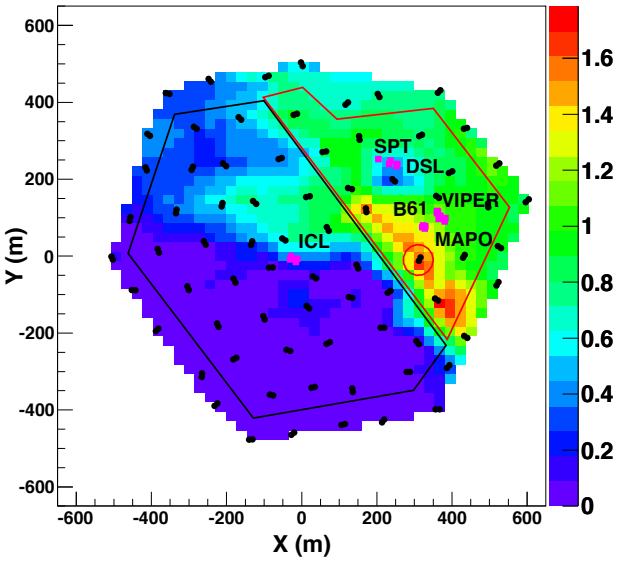


**Fig. 2**: Map of the snow coverage (in meters) over the IceTop tanks (black dots), during February of 2010. Pink squares labeled with acronyms are structures. The two outlined regions are the "old" subarray and "new" subarray used for optimizing a simple snow reconstruction [5]. The circle indicates Station 38, a very snowy station studied in this paper. Station 40 is two stations grid east of Station 38.

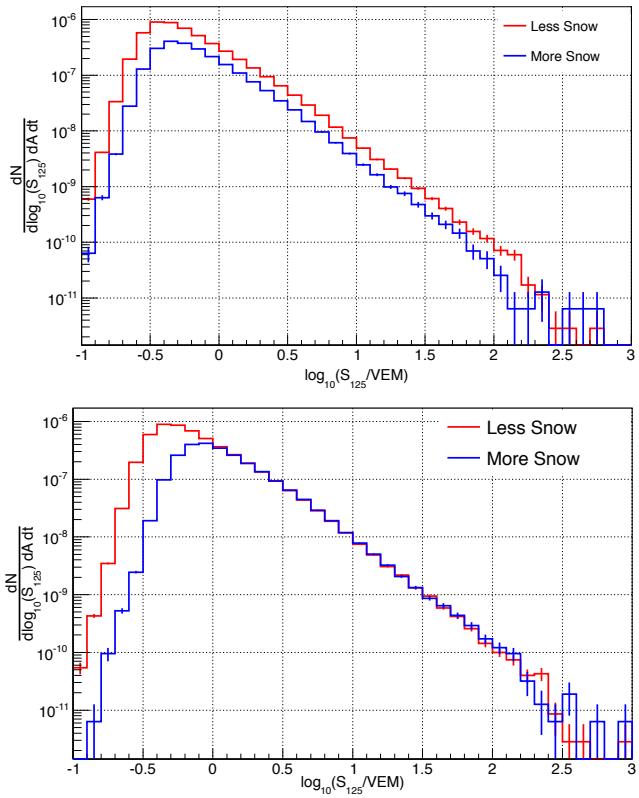


**Fig. 3**: $S_{125}$ distributions without any snow correction (above) and with an optimal snow correction (below).

tion length of approximately 85 g/cm$^2$ [9]. Using the average density of snow at the South Pole (measured on-site) which is 0.38 g/cm$^3$ [1], this effective attenuation length $\lambda_s$ should be about 2.1 m.

A simple exponential snow correction in reconstruction of air showers was first used in the analysis of 40-string IceTop-IceCube coincidence data for cosmic ray composition [4]. A shower's core location, direction, and $S_{125}$ are reconstructed by maximizing the likelihood that the track hypothesis (which predicts an expected signal, in the absence of snow) gave rise to the observed signal (details in [1]). To account for the attenuation by snow, the no-snow expected signal $S_0$ in a particular tank is reduced by an exponential factor:

$$S_{corr} = S_0 \exp(-X/\lambda_s) \quad \text{where} \quad X = d_{snow}/\cos(\theta)$$

before being compared to the observed signal in that tank. Here, "$X$" is the slant depth that particles must travel to a tank at a depth $d_{snow}$. Monthly tables of the snow depths of all the tanks, derived using VEMcal data, are used for this correction so that it changes appropriately over time. This simple treatment is also being used in current IceTop analyses such as: measurement of the all-particle spectrum with 73 IceTop stations alone [5] and with coincidence events which also pass through IceCube [6]. The correction was optimized by comparing the "old/more snow" subarray of the IceTop detector to the "new/less snow" subarray. A selection of these subarrays is shown in Figure 2. The best $\lambda_s$ is the one which brings the measured $S_{125}$ distributions from the different subarrays in line, as shown in Figure 3. In these studies, a $\lambda_s$ of 2.1 m fits the old/new subarray to each other well, but this number has a systematic uncertainty estimated at $\pm 0.2$ m.

## 3 Toward a more advanced snow correction: studies using IceTop data

Although an average $\lambda_s$ can be derived using some simplifying assumptions, the behavior of air shower signals in the real IceTop detector is expected to be more complicated. The fraction of the signal coming from unattenuated muons will vary (as a function of distance from the shower core, primary energy, primary composition, and zenith angle) Also, the shape of the spectrum of particles may vary from the assumed $E^{-2.7}$, with these same parameters.

Attenuation as a function of radius from the core was first studied using IceTop data itself. In particular, in IceTop-73 data (from 2010), many of the tanks were newly-deployed and covered with very little snow. These "no-snow tanks" can be used as a reference against which to compare signals in "snowy" tanks. A sample of events was collected for which the core position and direction was well-reconstructed, using quality cuts. For each tank, a normalized lateral distribution function (LDF) of signals was computed, in which each signal $S$ measurement in the histogram was divided by the $S_{125}$ of the event in which the tank was participating. These "normalized $S$ distributions" were made for both snowy and no-snow tanks; the distributions are systematically lower for snowy tanks due to the attenuation. Figure 4 shows the logarithm of the ratio between the normalized $S$ distribution of the tanks in a

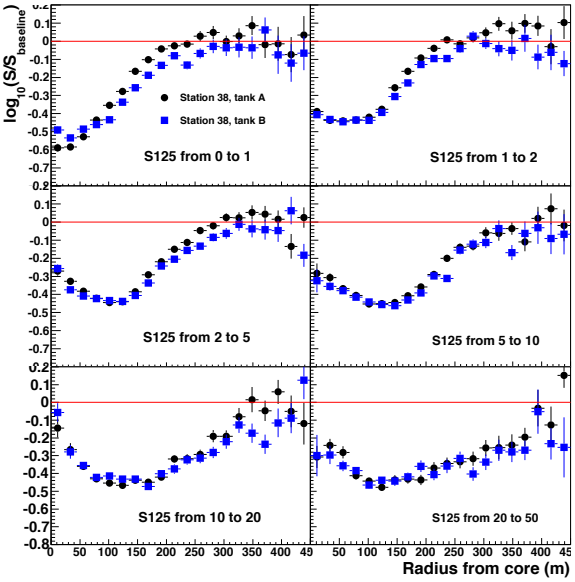


**Fig. 4**: Log of the ratio of normalized $S_{snowy}$ to normalized $S_{nosnow}$ as a function of distance from reconstructed core, for the two tanks in Station 38. The six panels represent a rough breakdown by energy. Near-vertical (0° to 20°) events only are selected.

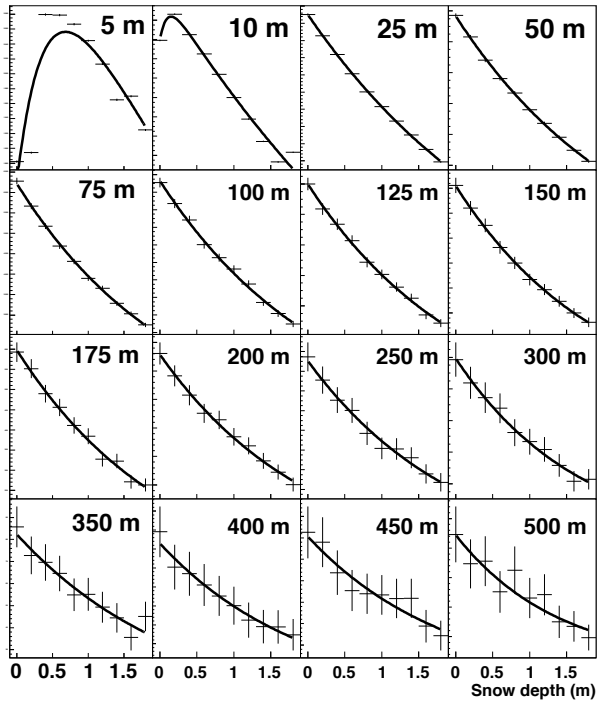


**Fig. 5**: Number of photoelectrons (arbitrarily normalized) hitting toy DOMs in the "ring simulation" as a function of snow depth, for various radii from the shower core. The showers are from 1 PeV vertical proton primaries. Each of the fit curves is a decaying exponential plus a short-range exponential rise.

snowy station to that of the normalized $S$ distribution of the no-snow baseline, in several different regimes of energy (as estimated by $S_{125}$). The more negative this value, the greater the attenuation of the total signal. The reduction of attenuation with increasing distance can be attributed to a changing muon content in the shower (further away, the shower becomes more dominated by muons and thus less effectively attenuated).

Muons do *not* explain the "upturn" in this ratio at small distances to the core, which indicates less attenuation (an enhancement) of signal close to the core. The effect grows more pronounced, and out to larger distances, at higher energies. Since real IceTop data suffers from reconstruction errors, unknown muon content, and effects from thresholds and saturation of PMT's, such a measurement is difficult to interpret on its own.

## 4 Toward a more advanced snow correction: a ring simulation

To explore these effects further, vertical CORSIKA[10] showers were simulated (both proton and iron primaries), at fixed energies (0.1, 0.316, 1, 10, and 100 PeV). In order to isolate the effect of snow on the EM component of the showers, all muons were stripped out of the CORSIKA files. The modified showers were then propagated through a simplified toy model of an IceTop-like detector, with single tanks (containing two DOMs each) spaced at sixteen different radii from the shower axis (5, 10, 25, 50, 75, 100, 125, 150, 200, 250, 300, 400, and 500 m). Each tank at each radius was simulated under 10 different snow depths, ranging from 0.0 to 1.8 m. The snow and the toy tanks were simulated using an IceTop simulation tool based on GEANT4 [11]. Photons arriving at the toy DOMs' photocathode were counted; details of the detector response beyond this were not simulated.

The number of photoelectrons registered in each toy tank as a function of snow depth for 1 PeV protons is shown in Figure 5, in which each of the 16 panels represents a different radius from the shower core There are some interesting features, namely: a) that attenuation is exponential (as expected), and the slope of the attenuation slowly changes as a function of radius, and b) that at very small radii (5 and 10 m from the core), snow causes an enhancement in signal at first, followed by attenuation. Corresponding plots for iron showers, and showers of other energies, show similar qualitative behavior.

Production from EM cascades of the highest-energy shower particles in the snow explains the enhancement feature at small distances. Figure 6 shows the spectra of electrons for various distances from the core, for 1 PeV proton showers. At most distances, the spectra have approximately the same shape, but very near the core (10 m and less), the harder electron spectrum stretches to higher energies. The particles in high-energy tails of the spectrum will cause EM cascades of their own in the snow, producing an increase in the number of particles at first, followed by a decrease as the now lower-energy particles attenuate away. To test this interpretation, particle distributions from CORSIKA at discrete core distances (such as those shown in Figure 6) were convolved with the Greisen function for EM cascades:

$$N_{e\gamma} = \frac{0.31}{\sqrt{\beta}} \exp(t(1 - \frac{3}{2}\log(s)))$$

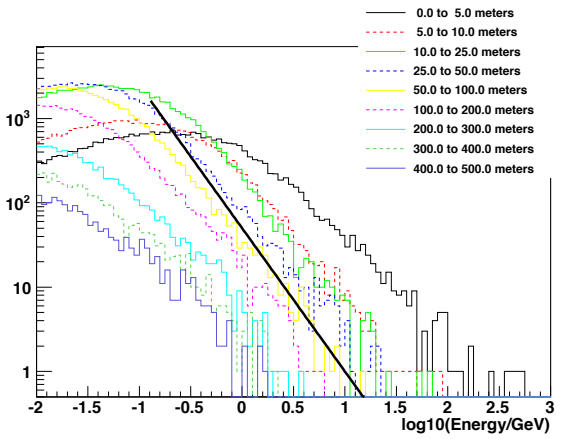


**Fig. 6**: Spectra of electrons from a 1 PeV proton event from CORSIKA. The different colors represent different distances from the shower core. The solid line is the shape of $E^{-2.7}$, to guide the eye.

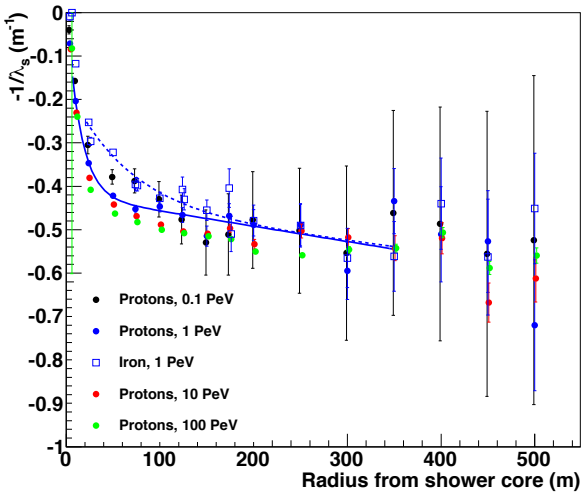


**Fig. 7**: Slope of an exponential fit to the sixteen curves such as in Figure 5, which is negative $1/\lambda_s$. Different colors represent different simulated proton primary energies, and 1 PeV iron is also shown for comparison. The 1 PeV data points have been fit to curves (protons = solid, and iron = dashed).

where $\beta = \log(E/83\text{MeV})$, $t$ is the slant depth $X$ in meters divided by $X_0/\rho$ (i.e. measured in radiation lengths), and $s = 3t/(t+2\beta)$ [8]. The convolution produces an expected number of particles as a function of snow depth; the resulting distributions look qualitatively very similar to Figure 5, with similar enhancement features at 5 and 10 meter distances in particular.

## 5 Results and Conclusions

Each of the 16 panels of Figure 5 was fit to a decaying exponential plus an EM-cascade "turnover". Similar fits were performed on all the CORSIKA sets (the different energies, and both protons and iron), all of which show similar qualitative behavior. A summary of the fitted exponential slope (which is $-1/\lambda_s$) as a function of radius to the shower core is shown in Figure 7.

Different primary energies and compositions show different attenuation lengths, especially at small distances where high-energy particles complicate the cascade physics. Most of the curves settle near a slope of around -0.5 (which is a $\lambda_s$ of about 2 m) at distances beyond 100 m. Since the IceTop hits that contribute most to an event reconstruction are generally at distances of 100-200 m, it is not surprising that the simple snow correction technique currently in use works well. However, this result also shows that improvement is possible; instead of one attenuation length $\lambda_s$ at all tanks, the attenuation response could be a function of a tank's position relative to the core, as well as other variables such as hypothesis energy, composition, or zenith.

One must also keep in mind that this attenuation behavior describes the EM shower component only, not the muons. One must also study the fraction of IceTop signals due to muons (either from theory or as part of the reconstruction itself), and attenuate only the EM fraction. So, in the future, a more advanced snow-corrected signal expectation will have a form like:

$$S_{corr} = S_{muons} + A(X)S_{EM}$$

where the attenuation function of slant depth $A(X)$ may be exponential ($A(X) = \exp(-X/\lambda_s)$), but may also include EM cascade effects for tanks very near the core.

This study still faces a number of unresolved issues. A different optimal $\lambda_s$ is found for Monte Carlo and data. The ring simulation studies vertical events only, and yet it is known that the behavior of the snow correction depends on zenith angle. A full simulation of IceTop under different snow depths will be necessary to study the effect of threshold and saturation settings, and hopefully to lead to a generalized snow correction technique which will improve reconstructions for all.

## References

[1] R. Abbasi et al. *NIM-A* **700**, 188-220 (2013).
[2] A. Achterberg et al. *Astropart.Phys.* **26**, 155 (2006).
[3] A. Van Overloop, *Proc. of the 32nd ICRC*, paper 0899 (2011).
[4] R. Abbasi et al. *Astropart. Phys.* **42**, 15-32 (2013).
[5] IceCube Collaboration, paper 0246, these Proceedings.
[6] IceCube Collaboration, paper 0861, these Proceedings.
[7] K. Nakamura et al.(PDG), *JPG* **37**, 075021 (2010).
[8] K. Greisen *Prog. Cosmic Ray Phys.* **3**, 1 (1956).
[9] T. Gaisser, "Cosmic Rays and Particle Physics" Cambridge University Press (1990).
[10] D. Heck et al., *Forschungszentrum Karlsruhe Report FZKA* **6019** (1998).
[11] S. Agostinelli et al., *NIM-A* **506** 250 (2003).